The Astrophysical Journal, 854:33 (31pp), 2018 February 10 https://doi.org/10.3847/1538-4357/aaa550

The *NuSTAR* Extragalactic Surveys: X-Ray Spectroscopic Analysis of the Bright Hard-band Selected Sample

L. Zappacosta[1], A. Comastri[2], F. Civano[3], S. Puccetti[4], F. Fiore[1], J. Aird[5,6], A. Del Moro[7,6], G. B. Lansbury[6,5], G. Lanzuisi[8,2], A. Goulding[9], J. R. Mullaney[10], D. Stern[11], M. Ajello[12], D. M. Alexander[6], D. R. Ballantyne[13], F. E. Bauer[14,15,16], W. N. Brandt[17,18,19], C.-T. J. Chen[17,18], D. Farrah[20], F. A. Harrison[21], P. Gandhi[6,22], L. Lanz[23], A. Masini[2,8], S. Marchesi[12], C. Ricci[14,24,25], and E. Treister[14]

[1] INAF—Osservatorio Astronomico di Roma, via di Frascati 33, I-00078 Monte Porzio Catone, Italy
[2] INAF Osservatorio Astronomico di Bologna, via Gobetti 93/3, I-40129 Bologna, Italy
[3] Harvard-Smithsonian Center for Astrophysics, 60 Garden Street, Cambridge, MA 02138, USA
[4] Agenzia Spaziale Italiana-Unitá di Ricerca Scientifica, Via del Politecnico, I-00133 Roma, Italy
[5] Institute of Astronomy, University of Cambridge, Madingley Road, Cambridge, CB3 0HA, UK
[6] Centre for Extragalactic Astronomy, Department of Physics, Durham University, South Road, Durham, DH1 3LE, UK
[7] Max-Planck-Institut für Extraterrestrische Physik (MPE), Postfach 1312, D85741, Garching, Germany
[8] Dipartimento di Fisica e Astronomia (DIFA), Università di Bologna, via Gobetti 93/2, I-40129, Bologna, Italy
[9] Department of Astrophysical Sciences, Princeton University, Princeton, NJ 08544, USA
[10] Department of Physics and Astronomy, The University of Sheffield, Hounsfield Road, Sheffield, S3 7RH, UK
[11] Jet Propulsion Laboratory, California Institute of Technology, 4800 Oak Grove Drive, Mail Stop 169-221, Pasadena, CA 91109, USA
[12] Department of Physics and Astronomy, Clemson University, Clemson, SC 29634-0978, USA
[13] Center for Relativistic Astrophysics, School of Physics, Georgia Institute of Technology, Atlanta, GA 30332, USA
[14] Instituto de Astrofísica, Facultad de Física, Pontificia Universidad Católica de Chile, 306, Santiago 22, Chile
[15] Millennium Institute of Astrophysics, Vicuña Mackenna 4860, 782 0436 Macul, Santiago, Chile
[16] Space Science Institute, 4750 Walnut Street, Suite 205, Boulder, CO 80301, USA
[17] Department of Astronomy and Astrophysics, The Pennsylvania State University, University Park, PA 16802, USA
[18] Institute for Gravitation and the Cosmos, Pennsylvania State University, University Park, PA 16802, USA
[19] Department of Physics, Pennsylvania State University, University Park, PA 16802, USA
[20] Department of Physics, Virginia Tech, Blacksburg, VA 24061, USA
[21] Cahill Center for Astrophysics, 1216 East California Boulevard, California Institute of Technology, Pasadena, CA 91125, USA
[22] School of Physics and Astronomy, University of Southampton, Highfield, Southampton SO17 1BJ, UK
[23] Department of Physics and Astronomy, Dartmouth College, 6127 Wilder Laboratory, Hanover, NH 03755, USA
[24] Chinese Academy of Sciences South America Center for Astronomy and China-Chile Joint Center for Astronomy, Camino El Observatorio 1515, Las Condes, Santiago, Chile
[25] Kavli Institute for Astronomy and Astrophysics, Peking University, Beijing 100871, People's Republic of China
Received 2017 May 24; revised 2017 December 1; accepted 2017 December 29; published 2018 February 8

Abstract

We discuss the spectral analysis of a sample of 63 active galactic nuclei (AGN) detected above a limiting flux of $S(8\text{–}24\ \mathrm{keV}) = 7\times10^{-14}$ erg s^{-1} cm^{-2} in the multi-tiered *NuSTAR* extragalactic survey program. The sources span a redshift range $z = 0\text{–}2.1$ (median $\langle z\rangle = 0.58$). The spectral analysis is performed over the broad 0.5–24 keV energy range, combining *NuSTAR* with *Chandra* and/or *XMM-Newton* data and employing empirical and physically motivated models. This constitutes the largest sample of AGN selected at >10 keV to be homogeneously spectrally analyzed at these flux levels. We study the distribution of spectral parameters such as photon index, column density ($N_{\rm H}$), reflection parameter ($\boldsymbol{R}$), and 10–40 keV luminosity ($L_{\rm X}$). Heavily obscured ($\log[N_{\rm H}/\mathrm{cm}^{-2}] \geqslant 23$) and Compton-thick (CT; $\log[N_{\rm H}/\mathrm{cm}^{-2}] \geqslant 24$) AGN constitute ∼25% (15–17 sources) and ∼2–3% (1–2 sources) of the sample, respectively. The observed $N_{\rm H}$ distribution agrees fairly well with predictions of cosmic X-ray background population-synthesis models (CXBPSM). We estimate the intrinsic fraction of AGN as a function of $N_{\rm H}$, accounting for the bias against obscured AGN in a flux-selected sample. The fraction of CT AGN relative to $\log[N_{\rm H}/\mathrm{cm}^{-2}] = 20\text{–}24$ AGN is poorly constrained, formally in the range 2–56% (90% upper limit of 66%). We derived a fraction ($f_{\rm abs}$) of obscured AGN ($\log[N_{\rm H}/\mathrm{cm}^{-2}] = 22\text{–}24$) as a function of $L_{\rm X}$ in agreement with CXBPSM and previous $z < 1$ X-ray determinations. Furthermore, $f_{\rm abs}$ at $z = 0.1\text{–}0.5$ and $\log(L_{\rm x}/\mathrm{erg\ s}^{-1}) \approx 43.6\text{–}44.3$ agrees with observational measurements/trends obtained over larger redshift intervals. We report a significant anti-correlation of R with $L_{\rm X}$ (confirmed by our companion paper on stacked spectra) with considerable scatter around the median R values.

Key words: galaxies: active – surveys – X-rays: galaxies

1. Introduction

Over the last decade, the advent of *Chandra* and *XMM-Newton* allowed extragalactic blank-field X-ray surveys to reach sufficient sensitivities (down to 10^{-17} erg s^{-1} cm^{-2}) and sky coverage (from tenths to several square degrees) to allow the study of distant populations of active galactic nuclei (AGN; Hickox & Markevitch 2006; Lehmer et al. 2012; Xue et al. 2012; Brandt & Alexander 2015; Luo et al. 2017). They resolved most (up to 80–90%) of the cosmic X-ray background (CXB) at energies below 10 keV (e.g., Hickox & Markevitch 2006; Cappelluti et al. 2017) as a mixture of obscured and unobscured AGN, in agreement with early population-synthesis model predictions (Setti & Woltjer 1989; Comastri et al. 1995). The fraction of resolved CXB gradually decreases

with energy being of the order of ∼50% above ∼10 keV and only a few percent at >10 keV with *Swift/BAT* & *INTEGRAL* studies (Krivonos et al. 2007; Ajello et al. 2008).

The missing unresolved AGN population, which is needed to account for the remaining high-energy CXB flux may be made up of a numerically non-negligible population of heavily obscured ($\log[N_{\rm H}/{\rm cm}^{-2}] \gtrsim 23$) non-local AGN (Worsley et al. 2005; Xue et al. 2012). It is therefore crucial to directly investigate the distribution of the obscured AGN population at the high column densities contributing to the CXB at high energies. A population of AGN with column densities in excess of 10^{24} cm^{-2}, called Compton-thick (CT) AGNs, and numerically comparable to the absorbed Compton-thin AGN, has long been posited to be responsible for the unaccounted 10–25% of the CXB flux required by population-synthesis models in order to reproduce its peak at 20–30 keV (Comastri et al. 1995; Gilli et al. 2007, hereafter G07). Recent works, however, suggest that the less obscured sources may also contribute significantly to the missing flux at >10 keV once other relevant high-energy spectral complexities of the AGN spectrum are taken into proper consideration (Treister et al. 2009; Akylas et al. 2012; Ueda et al. 2014). The latter would therefore lessen the need for a sizable contributing population of CT sources.

Given their very large column densities, the most obscured sources can effectively be detected in the X-rays at rest-frame energies >5–10 keV because their primary continuum is strongly suppressed at softer energies. This can be currently done: (i) locally ($z < 0.1$) by targeting bright sources (e.g., $\gtrsim 5 \times 10^{-12}$ erg s^{-1} cm^{-2}; Baumgartner et al. 2013) Seyfert-type ($L_{\rm X} \approx 5 \times 10^{43}$ erg s^{-1}) with hard X-ray (>10 keV) surveys, such as those performed by *Swift/BAT* and *INTEGRAL* (Krivonos et al. 2007; Ajello et al. 2008); and (ii) at high redshifts ($z > 1$) with the most sensitive *Chandra*/*XMM-Newton* observations of the deep/medium survey fields (e.g., Civano et al. 2016; Luo et al. 2017). Through either spectral or hardness ratio analysis, they allow one to quantify and characterize the obscured Compton-thin ($\log[N_{\rm H}/{\rm cm}^{-2}] =$ 22–24) AGN population and further shed light on the known decreasing trend between the numerical relevance of this population compared to all AGN (absorbed fraction) and the source luminosity (Lawrence & Elvis 1982; Gilli et al. 2007; Burlon et al. 2011; Buchner et al. 2015) and its redshift evolution (La Franca et al. 2005; Ballantyne et al. 2006; Treister & Urry 2006; Aird et al. 2015a; Buchner et al. 2015; Liu et al. 2017). They also allow exploration of the importance of the CT population, although with different constraining power and different non-negligible degrees of bias—especially at the highest column densities and lowest luminosities (e.g., Burlon et al. 2011; Brightman et al. 2014; Buchner et al. 2015; Lanzuisi et al. 2015; Ricci et al. 2015). Indeed, the large diversity in the spectral shapes, as well as poorly explored observational parameters in low counting regimes[26] such as the high energy cut-off and the reflection strength at high energies (Treister et al. 2009; Ballantyne et al. 2011, hereafter BA11), the scattered fractions at low energies (Brightman & Ueda 2012; Lanzuisi et al. 2015), or physical parameters such as the Eddington ratio (Draper & Ballantyne 2010), may further introduce uncertainty or biases, enlarging the possible range of the fraction of CT sources to an order of magnitude (Akylas et al. 2012) or even significantly reducing their importance (Gandhi et al. 2007). Indeed, given the paucity of CT sources effectively contributing to the CXB missing flux, the most recent population-synthesis models have tried to explain the CXB missing component as mainly a pronounced reflection contribution from less obscured sources with a reduced contribution by CT AGN (Treister et al. 2009; Ballantyne et al. 2011; Akylas et al. 2012).

Going deeper at high energies while retaining the capability of being greatly less affected by obscuration bias will enable us to efficiently sample a more distant ($z = 0.1$–1) and luminous population (i.e., at the knee of the luminosity function, $L_{\rm X} \approx 10^{44}$ erg s^{-1}) of obscured sources and better characterize their high-energy spectrum, substantially improving constraints on the majority of the obscured AGN contributing to the CXB (e.g., Gilli 2013). The *Nuclear Spectroscopic Telescope Array* (*NuSTAR*; Harrison et al. 2013) is perfectly tailored to this task. Indeed, as the first hard X-ray focusing telescope in orbit, it increases sensitivity by two orders of magnitude compared to any previous hard X-ray detector. With its higher sensitivity, *NuSTAR* has resolved ∼35% of the CXB near its peak (Harrison et al. 2016, hereafter H16) and is able to probe the hard X-ray (>10 keV) sky beyond the local universe ($z > 0.1$).

The *NuSTAR* wedding-cake extragalactic survey strategy focuses on several well-known medium-deep fields with extensive multi-wavelength coverage. The core of it includes the EGS (A. Del Moro et al. 2018, in preparation), E-CDFS (Mullaney et al. 2015), and COSMOS (Civano et al. 2015) fields, as well as a wider and typically shallower serendipitous survey (Lansbury et al. 2017b, L17). A further extension of it with the observation of two deep fields (CDF-N, A. Del Moro et al. 2018, in preparation; UDS, Masini et al. 2018) has also recently been completed. This multi-tiered program has already detected 676 AGN out to $z \approx 3.4$ (Alexander et al. 2013; Aird et al. 2015b; Civano et al. 2015; Mullaney et al. 2015; Lansbury et al. 2017b), of which 228 are significantly detected in the hard 8–24 keV *NuSTAR* band. In particular, at low redshift, Civano et al. (2015) presented the spectroscopic identification of a local ($z \sim 0.04$) low-luminosity ($\sim 5 \times 10^{42}$ erg s^{-1}) CT AGN not previously recognized by either *Chandra* or *XMM-Newton,* with a column density $N_{\rm H} \geqslant 10^{24}$ cm^{-2}. Lansbury et al. (2017a) identified three similar sources at $z < 0.1$ that have even higher obscuration in the *NuSTAR* serendipitous survey. At high redshift, Del Moro et al. (2014) presented the detection of a heavily absorbed ($N_{\rm H} = 6 \times 10^{23}$ cm^{-2}) quasar at $z = 2$.

The redshift range and the luminosities probed by the *NuSTAR* extragalactic survey program are well-matched to CXB population-synthesis models, in terms of characterization of the AGN high-energy spectral shape and of the dominant obscured populations contributing to the CXB. In the latter case, population-synthesis models predict the largest CT AGN contributions from sources at $z = 0.4$–1.2 with luminosities $L_{2-10} \lesssim 10^{44}$ erg s^{-1} (e.g., Gilli 2013) and that their contribution to the residual CXB flux may amount to 90% by $z \sim 2$. (Treister et al. 2009). We therefore expect *NuSTAR* to start to evaluate the relative importance of the obscured AGN populations and shed light on the main aspects contributing to the still-unaccounted remaining flux on the peak of the CXB (i.e., heavy absorption versus reflection).

In order to elucidate those aspects in this paper, we carry out a systematic broadband (0.5–24 keV) spectral analysis of 63 sources detected in the core *NuSTAR* Extragalactic Survey program, selected to have fluxes in the 8–24 keV energy band brighter than $S_{8-24} = 7 \times 10^{-14}$ erg s^{-1} cm^{-2}. We complement

[26] I.e., at the highest column densities or at the high/low-energy spectral boundaries where the instruments are less sensitive.

the *NuSTAR* data with archival low-energy data from *Chandra* and *XMM-Newton*. We perform broadband (0.5–24 keV) spectral modeling, characterize their spectral properties, and obtain a column density distribution, absorbed/CT fractions, and source counts, then compare them to predictions from population-synthesis models and past observational works. A companion paper (Del Moro et al. 2017, DM17) reports on the properties of the average X-ray spectra from all sources detected in the *NuSTAR* deep and medium survey fields.

This paper is organized as follows. Section 2 presents the sample, with Sections 3 and 4 devoted to the data reduction and spectral characterization of the source properties, respectively. We then discuss the column density distribution (Section 5), fraction of CT AGN (Section 6), fraction of absorbed sources as a function of luminosity and redshift (Section 7), and source counts (Section 8). We discuss the results in Section 9, and present the conclusions in Section 10. Relevant notes on individual sources are presented in the Appendix.

Throughout the paper, we adopt a flat cosmology with $\Omega_\Lambda = 0.73$ and $H_0 = 70\ \mathrm{km\ s^{-1}\ Mpc^{-1}}$. Errors are quoted at the 1σ level and upper/lower limits at the 90% confidence level (c.l.). The X-ray luminosities are quoted in the standard (for *NuSTAR* survey studies) rest-frame 10–40 keV energy band.

2. Description of the Sample

We draw our sample from the high-energy *NuSTAR* catalogs compiled for the COSMOS (Civano et al. 2015, C15), ECDF-S (Mullaney et al. 2015, M15), EGS (A. Del Moro et al. 2018, in preparation, DMIP) and serendipitous survey fields (L17). In order to have consistent catalogs, the same data-reduction tasks, mosaicing procedures, source-detection steps, photometry, and deblending algorithm were applied to all survey fields (see C15, M15, and Aird et al. 2015b for details). In the following, we briefly outline the source-identification procedure adopted in each catalog. The identification of the sources was consistently done through a SExtractor-based procedure on false probability maps generated on the mosaiced images accounting for the corresponding background maps in three energy bands (3–8, 8–24, 3–24 keV). No positional priors from previous low-energy X-ray surveys have been used in the source identification. Through simulated data, a proper threshold to set the significance of each source identification in each band has been adopted, and the final balance between completeness and reliability in each catalog has been chosen such there are no more than two or three possible spurious sources, down to the limiting flux in each catalog. Further details and description of the procedures regarding deblending, photometry, final catalog building, and association to low-energy counterparts are reported in each catalog paper. For our purposes, in order to minimize obscuration bias, we selected objects with relatively bright fluxes in the hard 8–24 keV band. The fluxes adopted for this selection have been estimated from the 8–24 keV counts collected in 30″ apertures[27] by the catalog papers, by assuming a power-law model with $\Gamma = 1.8$. Whenever possible, we complemented *NuSTAR* data with archival lower-energy data from *Chandra* and *XMM-Newton*.

[27] The fluxes reported in C15 are from 20″ apertures. They have been extrapolated to 30″ aperture fluxes by assuming a 1.47 constant conversion factor. This factor is obtained as the ratio between the fluxes in 30″ and 20″ apertures measured from the on-axis *NuSTAR* point-spread function.

2.1. Medium-deep Survey Fields

Given the $12' \times 12'$ *NuSTAR* field of view, the survey fields (COSMOS, ECDF-S,and EGS) were observed with a mosaicing strategy whereby each neighboring pointing was shifted by half of a field of view. This tile arrangement produces homogeneous and continuous coverage in the deep central region with contiguous shallower edges. The main properties of these surveys are reported in Table 1.

Despite *NuSTAR* being sensitive up to 79 keV, typical faint sources in the deep surveys are not detected to such high energies. In the extragalactic survey work to date, we have therefore only considered three energy bands: 3–24 keV (total), 3–8 keV (soft), and 8–24 keV (hard).

Figure 1 reports the 8–24 keV sensitivity curves as a function of hard-band flux for all the fields. The sensitivities at 50% survey coverage are reported in Table 1. Notice that they are based on the assumption of an unabsorbed $\Gamma = 1.8$ power-law spectrum. This is an approximation that is reasonable for Compton-thin sources, given that above 8 keV their spectrum is minimally altered at the highest column densities (i.e., $\log[N_\mathrm{H}/\mathrm{cm^{-2}}] \gtrsim 23$). However, it may be somewhat inadequate for CT sources whose spectrum substantially deviates from this assumed spectral shape within this hard band. Therefore, it may give biased results in calculating the intrinsic distribution of physical quantities for the sampled AGN population. We account for this by correcting a posteriori for this bias (see Section 6 and Figure 11).

2.2. Serendipitous Survey Fields

The serendipitous fields considered in this work consist of all fields analyzed as part of the serendipitous survey through 2015 January 1. This extends the sample presented by Alexander et al. (2013), and is a subset of the program presented in L17. The selection criteria adopted are reported in the following and constitute a slight modification to those employed in Aird et al. (2015b):

1. We minimize Galactic point-source contamination by requiring Galactic latitudes $>20°$.
2. In order to emphasize fields where our serendipitous survey follow-up is currently more complete, we only consider fields accessible from the northern hemisphere by requiring declinations $>-5°$.
3. We exclude fields with a large contamination from the primary targets by requiring $<10^6$ counts within 120″ of the aimpoint, and that primary targets contribute $\lesssim$6% to the extracted emission of the serendipitous source within the extraction region.

After these cuts, the sky coverage of the serendipitous survey considered here amounts to $\approx 4\ \mathrm{deg^2}$ (see Figure 1). Further survey details are reported in Table 1. It is worth noting that, despite the serendipitous survey having sensitivity better than COSMOS over a wider area and comparable faint source sensitivity to ECDF-S, it still has the disadvantage of having less multi-wavelength coverage. This usually translates to lower redshift completeness (from optical spectroscopy) and a poorer-quality X-ray coverage at low energies from *Chandra* and/or *XMM-Newton* (see L17).

Table 1
Main Properties of the *NuSTAR* Extragalactic Surveys and Relative Catalogs

Survey	Total Exp.[a]	Pointings Exp.[b]	Deepest Exp.[c]	Pointing Layout[d]	Area	Detected Sources		Sensitivity 50%[e]		References
	(Ms)	(ks)	(ks)		(deg^2)	3–24 keV	8–24 keV	3–24 keV	8–24 keV	
EGS	1.6	50	400	8×1	0.24	39	14	0.39	0.35	DMIP
ECDF-S	1.5	45–50	360	4×4	0.31	49	19	0.39	0.45	M15
COSMOS	3.0	20–30	90	11×11	1.73	91	32	0.77	0.93	C15
Serendipitous[f]	2.2	20–1000	970	Random	3.91	118	38	1.70	1.35	L17

Notes.
[a] Total exposure time devoted to the survey.
[b] Average exposure times of the single pointings; notice that the serendipitous survey consists of pointings with a large range of exposure times.
[c] Average exposure in the deepest field.
[d] Tiling design of the survey.
[e] Flux reached at 50% of the survey area coverage, in units of 10^{-13} erg s^{-1} cm^{-2}.
[f] This is a subsample of the serendipitous survey sample presented in L17 (see Section 2.2).

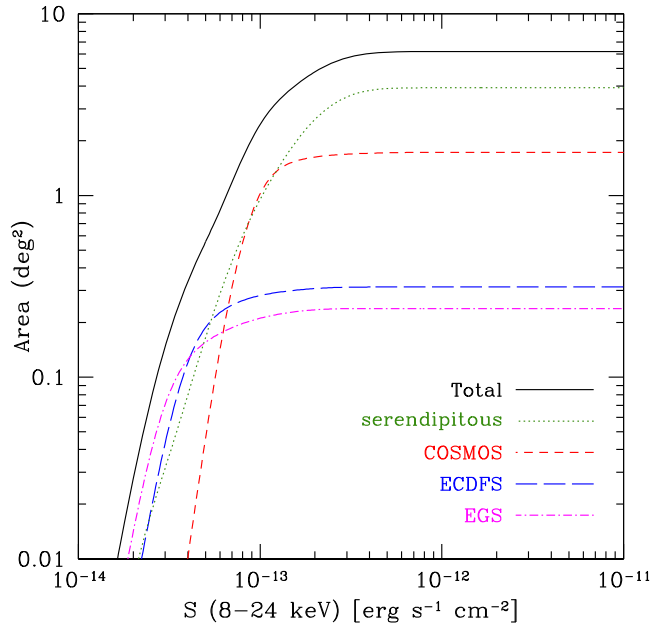

Figure 1. Total and individual sensitivity curves as a function of the hard-band flux for the surveys included in our sample. Black solid curve is for the entire sample, magenta dotted–dashed is for EGS, blue long-dashed is for ECDF-S, red short-dashed is for COSMOS, and green dotted is for the serendipitous survey.

2.3. Selected Sample

The final catalogs consist of 91, 49, 39, and 118 objects, respectively, from the *NuSTAR* COSMOS, ECDF-S, EGS, and serendipitous survey. Of these, 32, 19, 14, and 38, respectively, are significantly detected in the hard-band, based on a maximum likelihood estimator (see C15, M15, Aird et al. 2015b, and L17 for details and the adopted thresholds). These objects are shown in Figure 2 (left panel), which displays the net 3–24 keV counts within a 30″ aperture versus their aperture-corrected photometry in the 8–24 keV energy band. From this combined sample, we select sources with hard-band flux $S_{8-24\,\mathrm{keV}} \geqslant 7 \times 10^{-14}$ erg s^{-1} cm^{-2}. We are sensitive to fluxes larger than this value in 80% of the surveyed area (see Figure 1). This subsample, corresponding to objects above the dashed line in Figure 2, includes a total of 31, 3, 5, and 24 objects from the four surveys, respectively, selected over a total area of $\sim$6 deg^2. The resulting sample of 63 sources is the focus of the following analysis. The redshift distribution is reported in the right panel of Figure 2, compared to the distribution of the 199 local sources detected by *Swift*-BAT in the energy range 15–55 keV (Burlon et al. 2011). *NuSTAR*, with its two orders of magnitude greater sensitivity, probes sources well beyond the local universe. Table 2 reports the position, spectroscopic redshift, *Chandra* and *XMM-Newton* counterparts, *NuSTAR* observation IDs, and *NuSTAR* survey for all 63 sources. When referring to the single sources, we use the catalog IDs listed in column 2 prefixed by *ecdfs*, *egs*, *cosmos,* and *ser* for sources from respectively the *NuSTAR*- ECDF-S, EGS, COSMOS, and serendipitous catalogs.

Objects from the deep fields all have unique counterparts at lower energies from either the *Chandra* (Lehmer et al. 2005; Xue et al. 2011; Civano et al. 2012, 2016; Goulding et al. 2012) or *XMM-Newton* (Brusa et al. 2010; Ranalli et al. 2013) surveys of these same fields, with the exception of one source in the ECDF-S field (*ecdfs5*; this source has two possible counterparts, one at low and one at high redshift; see Table 2 and Appendix).

A few sources have nearby potential contaminants (i.e., inside the *NuSTAR* extraction radius) in the deep survey fields. Contamination ultimately is unimportant or partially negligible in most cases, as discussed for the affected sources in the Appendix. For some cases (*cosmos154* and *cosmos181*), we restrict the *NuSTAR* low-energy bound to 4–5 keV, where the contamination becomes less important. In a few other cases, the contamination is such that, within the uncertainties, it could potentially lower the true hard-band source flux also below the threshold flux used in our sample selection (*cosmos107*, *cosmos178*, and *cosmos229*). For the serendipitous survey sources, most have counterparts from at least *Chandra* or *XMM-Newton*, the exception being five sources (*ser97*, *ser285*, *ser235*, *ser261*, *ser409*; see Table 4) that have not yet been observed by these satellites.

3. Data Reduction

3.1. NuSTAR

In order to perform a proper spectral analysis for these low-count point-like sources (i.e., from tens to hundreds of counts; see Figure 2), we need to carefully account for: 1. the relatively uniform arcmin-scale *NuSTAR* point-spread function (FWHM = 18″; half-power diameter HPD = 58″; Harrison et al. 2013); and 2. the spectrally variable and spatially dependent background

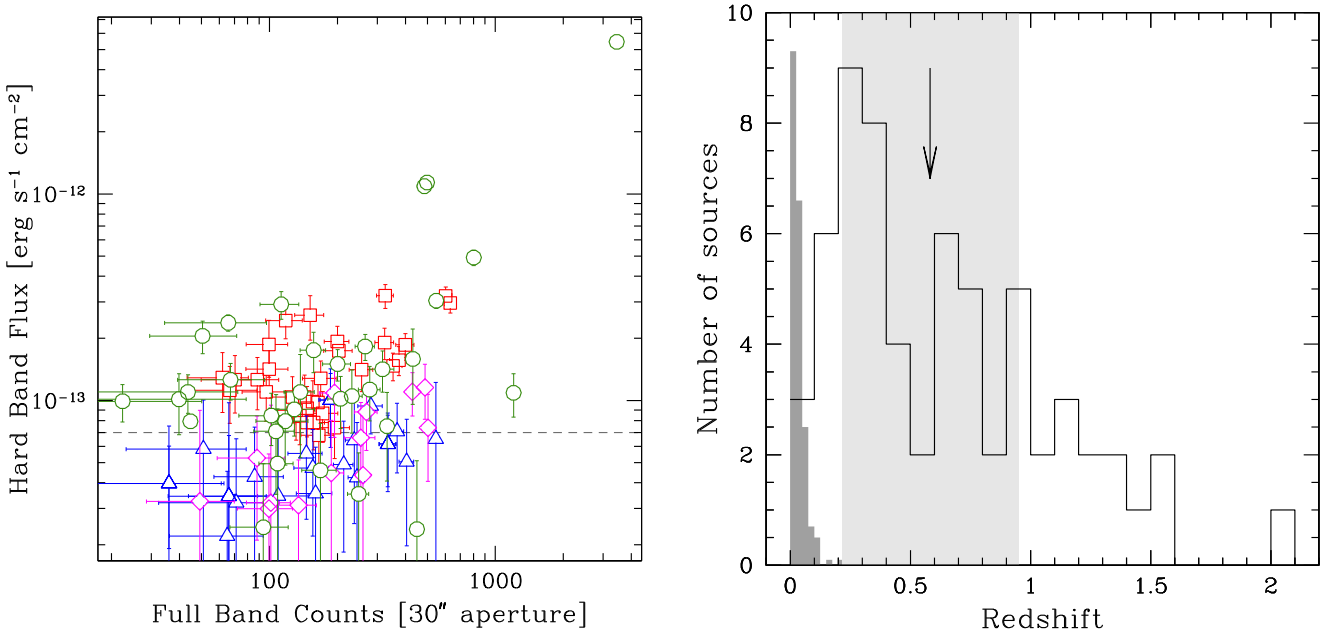

Figure 2. Left panel: net counts in the full (3–24 keV) energy band from a 30″ aperture vs. the hard (8–24 keV) deblended aperture-corrected flux for the hard-band detected objects in the *NuSTAR*-COSMOS (red squares), *NuSTAR*-ECDF-S (blue triangles), *NuSTAR*-EGS (magenta diamonds), and *NuSTAR*-Serendip (green circles) catalogs. For the COSMOS sources, the flux has been extrapolated from the 20″ apertures reported in C15, assuming a constant conversion factor of 1.47 based on the on-axis *NuSTAR* point-spread function. The horizontal dashed line indicates the threshold value of 7×10^{-14} erg s^{-1} cm^{-2} defining our sample. Right panel: spectroscopic redshift distribution of our sample (open histogram) compared to the the 199 local sources studied by *Swift*-BAT in Burlon et al. (2011; dark gray, with normalization and histogram binning rescaled by a factor of 10). The arrow indicates the median redshift value for the sample ($\langle z \rangle = 0.58$) and the light gray region shows the interquartile range.

(for details, see Wik et al. 2014). In particular, the latter at $<$20 keV is strongly affected by stray light from unfocused CXB photons reaching the detectors through the open design of the observatory (called "aperture background").

Given the flux levels of the sources in our sample, it is necessary to maximize and carefully account for their contribution relative to the backgrounds (especially with respect to the spatially dependent "aperture background"). We therefore optimize the spectral extraction radius to maximize the signal-to-noise ratio (S/N) and, within the Poissonian uncertainties, the number of collected net counts. To do this, we started with the level 2 data products and simulated background maps where the latter were created using the software NUSKYBGD (Wik et al. 2014) as described in C15 and M15. The simulated background maps reproduce the "aperture background" across the FoV and the normalization of the total background in each observation. In detail, we used all the observations pertaining to a given source in order to determine the total counts in increasing circular apertures centered on the source position, calculating both source +background counts (S) from the event files and background counts alone (B) from the simulated maps. We then calculated the radial profile for the net source counts $N(<r) = S(<r) - B(<r)$ and $S/N(<r) = \frac{N(<r)}{\sqrt{N(<r)+2B(<r)}}$. The radius for spectral extraction $r_{\rm ex}$ is chosen as the radius that maximizes the S/N profile and, within its $\pm 1\sigma$ range, also maximizes N. In the few (nine for COSMOS and one for ECDFS) cases in which a source is blended with a nearby source (closer than 2 arcmin), we further reduced $r_{\rm ex}$ so that the source flux from the contaminating source is reduced, within the aperture, to levels of 5–6%. Table 4 reports $r_{\rm ex}$ values for all the sources in our sample.

We used the task "nuproducts" in NUSTARDAS v.1.4.1 with the *NuSTAR* calibration database (CALDB version 20150123) for the spectral extractions and the creation of relative response files.

The background spectrum for each source spectrum was simulated from the best-fit models of the background across the detectors obtained with NUSKYBGD. This software performs iterative joint fits of the observed backgrounds across the field extracted in $\gtrsim$3 arcmin apertures placed in each chip of each focal plane module. The joint modeling aims to determine the normalization of the different background components, and hence characterize them at the position of the source. The fits are performed using spectral models of the instrumental (continuum + line activation due to particle background), cosmic focused (CXB) and cosmic unfocused background (straylight) components, and information on their spatial dependence across the detectors. We checked each best fit to ensure that no significant spatial or spectral residuals were present. After this procedure, we are (in principle) able to well-reproduce the background spectrum at each position of the detector. We further verify this by creating background-subtracted images and visually inspecting them for spatial gradients indicative of poor background modeling. As a final step, the best-fit spectral model is used by NUSKYBGD to simulate the background within the source extraction aperture, but using an exposure time multiplied by 100 to ensure high S/N.

We then co-added spectra, simulated backgrounds and response files for each source and in each detector. Table 4 reports *NuSTAR* net counts and total exposure time collected for each source.

Table 2
The Bright *NuSTAR* Hard-band Spectroscopic Sample

Name	ID$_N$[a]	R.A.	Decl.	z[b]	ID$_C$[c]	ID$_X$[d]	*NuSTAR* Observation IDs[e]	Catalog
NuSTAR J100129+013636	cosmos97	150.372537	+1.610073	0.104	cid1678	2021	098001 099001	COSMOS
NuSTAR J100249+013851	cosmos107	150.705859	+1.647561	0.694	lid1688	5496	101002 103001	COSMOS
NuSTAR J100101+014752	cosmos129	150.256432	+1.797837	0.907	cid284	54490	037002 038001 060001	COSMOS
NuSTAR J095815+014932	cosmos130	149.564437	+1.825731	1.509	lid961	5323	090001 091001	COSMOS
NuSTAR J095926+015348	cosmos145	149.860885	+1.896815	0.445	cid209	293	012001 018001 062001 063001	COSMOS
NuSTAR J100055+015633	cosmos154	150.233212	+1.942588	0.219	cid1105	131	029001 030001 035002 036002	COSMOS
NuSTAR J100024+015858	cosmos155	150.104087	+1.982873	0.373	cid358	1	023001 024001 029001 030001	COSMOS
NuSTAR J095840+020437	cosmos178	149.668862	+2.077021	0.340	cid168	417	004001 005001 087001 088002	COSMOS
NuSTAR J100141+020348	cosmos181	150.423842	+2.063424	0.125	cid482	2608	040001 041001 050001 051001	COSMOS
NuSTAR J095918+020956	cosmos194	149.826665	+2.165826	1.157	cid320	5	003001 004001 009002-B 010001	COSMOS
NuSTAR J100308+020917	cosmos195	150.785979	+2.154816	1.470	lid1646	5321	109001 111001	COSMOS
NuSTAR J095857+021320	cosmos206	149.738507	+2.222475	1.024	cid329	2	003001 004001	COSMOS
NuSTAR J100307+021149	cosmos207	150.782581	+2.197149	0.582	lid1645	5370	111001 113001	COSMOS
NuSTAR J095817+021548	cosmos216	149.573824	+2.263384	0.707	lid633	54514	086001 087001	COSMOS
NuSTAR J100032+021821	cosmos217	150.133457	+2.305840	1.598	cid87	18	020002 021001 026001 027002	COSMOS
NuSTAR J095902+021912	cosmos218	149.761712	+2.320121	0.345	cid440	3	002001 003001 008001 009002	COSMOS
NuSTAR J095909+021929	cosmos229	149.789727	+2.324908	0.378	cid420	23	002001 003001 008001 009002	COSMOS
NuSTAR J095957+022244	cosmos232	149.990626	+2.378889	0.931	cid530	212	013001 014001 019001 020002	COSMOS
NuSTAR J100228+024901	cosmos249	150.620155	+2.817155	0.213	lid3218	5014	067001 120001	COSMOS
NuSTAR J095945+024750	cosmos251	149.941358	+2.797420	1.067	lid545	5620	076001 077001-A 078001	COSMOS
NuSTAR J100238+024651	cosmos253	150.658422	+2.780956	0.212	lid484	5114	120001 121001	COSMOS
NuSTAR J095908+024310	cosmos263	149.785525	+2.719548	1.317	lid549	5230	077001 079001 080001	COSMOS
NuSTAR J100243+024025	cosmos272	150.682309	+2.673758	0.669	lid492	5400	118001 119001 120001 121001	COSMOS
NuSTAR J100204+023726	cosmos282	150.520310	+2.623974	0.519	lid294	7	046002 046004 065002 066001	COSMOS
NuSTAR J095837+023602	cosmos284	149.656383	+2.600703	0.735	lid1856	2076	082001 083001	COSMOS
NuSTAR J100232+023538	cosmos287	150.635807	+2.593895	0.658	lid280	5133	046002 116001 117001-B 118001 119001	COSMOS
NuSTAR J095849+022513	cosmos296	149.704281	+2.420472	1.108	cid513	126	001002 002001	COSMOS
NuSTAR J095848+022419	cosmos297	149.700185	+2.405449	0.375	cid417	135	001002 002001	COSMOS
NuSTAR J100229+023223	cosmos299	150.624855	+2.539961	0.432	lid278	5222	046002 046004 065002 116001 118001	COSMOS
NuSTAR J095839+022350	cosmos322	149.662604	+2.397242	0.356	lid622	1429	001002 002001 084001 085001	COSMOS
NuSTAR J100259+022033	cosmos330	150.747792	+2.342593	0.044	lid1791	5371	113001 115001	COSMOS
NuSTAR J033136−280132	ecdfs5	52.901946	−28.025645	0.141	103	⋯	001003 001002 001003	E-CDFS
				1.957	100	⋯		E-CDFS
NuSTAR J033207−273736	ecdfs20	53.032301	−27.626858	0.976	301	358	013001 013002 014001 014002	E-CDFS
NuSTAR J033328−275642	ecdfs51	53.370361	−27.945068	0.841	712	⋯	004001 004002 008001 008002	E-CDFS
NuSTAR J141736+523029	egs1	214.400911	+52.508258	0.987	37	⋯	001002 001004 001006 001008	EGS
NuSTAR J141754+524138	egs9	214.475905	+52.694030	0.464	294	⋯	001002 001004 001008 002002	EGS
							002003 002004B 002005	
NuSTAR J142047+525809	egs26	215.196713	+52.969305	0.201	669	⋯	006002 006003 006004 006005	EGS
							007001 007003 007005 007007	
NuSTAR J142052+525630	egs27	215.220076	+52.941858	0.676	622	⋯	006002 006004A 006005 007001	EGS
							007005 007007	
NuSTAR J142027+530454	egs32	215.113227	+53.081728	0.997	863	⋯	007001 007003 007005 007007	EGS
							008001 008002 008003 008004	
							60002048002	
NuSTAR J023228+202349	ser37	38.119089	+20.397218	0.029	⋯	⋯	60002047006 60002047004	Serendip
NuSTAR J035911+103126	ser77	59.798670	+10.523951	0.167	⋯	⋯	60061042002	Serendip
NuSTAR J051617−001340	ser97	79.073788	−0.227904	0.201	⋯	⋯	60001044004 60001044002	Serendip

Table 2
(Continued)

Name	ID$_N$[a]	R.A.	Decl.	z[b]	ID$_C$[c]	ID$_X$[d]	*NuSTAR* Observation IDs[e]	Catalog
NuSTAR J061640+710811	ser107	94.167546	+71.136661	0.203	⋯	⋯	60002048010 60002048006 60002048004	Serendip
NuSTAR J075800+392027	ser148	119.503085	+39.341045	0.095	⋯	⋯	60001131002	Serendip
NuSTAR J081909+703930	ser153	124.789365	+70.658570	1.278	⋯	⋯	30001031005 30001031003 30001031002	Serendip
NuSTAR J095512+694739	ser184	148.800066	+69.794361	0.675	⋯	⋯	80002092011 80002092009 80002092008	Serendip
							80002092007 80002092006 80002092004	
							80002092002	
NuSTAR J102345+004407	ser213	155.938116	+0.735278	0.300	⋯	⋯	30001027006	Serendip
NuSTAR J102628+254417	ser215	156.619145	+25.738177	0.827	⋯	⋯	60001107002	Serendip
NuSTAR J110740+723234	ser235	166.919819	+72.542882	2.100	⋯	⋯	60002042004 60002042002	Serendip
NuSTAR J112829+583151	ser243	172.122122	+58.530861	0.410	⋯	⋯	50002041003 50002041002	Serendip
NuSTAR J115912+423242	ser254	179.802748	+42.545158	0.177	⋯	⋯	60001148004 60001148002 60061217006	Serendip
							60061217004B 60061217002	
NuSTAR J120613+495712	ser261	181.555033	+49.953531	0.784	⋯	⋯	60061357002	Serendip
NuSTAR J121358+293608	ser267	183.494820	+29.602344	0.131	⋯	⋯	60061335002	Serendip
NuSTAR J121425+293610	ser273	183.607905	+29.603048	0.308	⋯	⋯	60061335002	Serendip
NuSTAR J122751+321222	ser285	186.964887	+32.206371	0.733	⋯	⋯	60001108002	Serendip
NuSTAR J134513+554751	ser318	206.304766	+55.797766	1.167	⋯	⋯	60002028002	Serendip
NuSTAR J143026+415959	ser335	217.610385	+41.999984	0.352	⋯	⋯	60001103002	Serendip
NuSTAR J151508+420837	ser359	228.786883	+42.143734	0.289	⋯	⋯	60061348002	Serendip
NuSTAR J151654+561744	ser363	229.225216	+56.295566	1.310	⋯	⋯	30002039005A 30002039003 30002039002	Serendip
NuSTAR J171309+573421	ser382	258.288435	+57.572549	0.243	⋯	⋯	60001137002	Serendip
NuSTAR J181429+341055	ser401	273.621211	+34.181958	0.763	⋯	⋯	60001114002	Serendip
NuSTAR J182615+720942	ser409	276.563078	+72.161734	1.225	⋯	⋯	60161687002	Serendip
NuSTAR J204020−005609	ser451	310.087027	−0.936058	0.601	⋯	⋯	30001120005 30001120004 30001120003	Serendip
							30001120002	

Notes.
[a] Identification name for each source. This is made from a prefix indicating the source parent catalog plus the ID from *NuSTAR* parent catalogs (Section 2). The prefixes of each parent catalog are *cosmos* for COSMOS, *ecdfs* for ECDF-S *egs* for EGS, and *ser* for the serendipitous survey.
[b] All the redshifts are spectroscopic. They are taken from: Brusa et al. (2010; COSMOS), Lehmer et al. (2005), Xue et al. (2011) and Ranalli et al. (2013; ECDF-S), Nandra et al. (2015; EGS), and L17 (*NuSTAR* Serendipitous Survey).
[c] *Chandra* IDs are from Elvis et al. (2009) and Civano et al. (2016; COSMOS, with prefix *cid* and *lid* respectively), Lehmer et al. (2005; ECDF-S), and Nandra et al. (2015; EGS).
[d] *XMM-Newton* IDs are from Brusa et al. (2010; COSMOS) and Ranalli et al. (2013; ECDF-S).
[e] To obtain the full *NuSTAR* observation IDs for the COSMOS, ECDF-S, and EGS fields, the six-digit survey identification numbers 60021, 60022, and 60023 must be prefixed, respectively.

Table 3
Low-energy Observations Used for Serendipitous Sources

ID	*Chandra*		*XMM-Newton*	
	ObsID	Notes	ObsID	Notes
ser37	⋯	⋯	0604210201	⋯
	⋯	⋯	0604210301	⋯
ser77	10234	1	0064600101	⋯
	⋯	⋯	0064600301	⋯
ser107	⋯	⋯	0111220201	2
ser148	⋯	⋯	0406740101	⋯
ser153	⋯	⋯	0724810301	3
ser184	10542	4	0657801901	3
	10543	4	0657802101	3
	10544	4	0657802301	3
	10925	4	⋯	⋯
	11800	4	⋯	⋯
	11104	4	⋯	⋯
ser213	⋯	⋯	0203050201	⋯
ser215	12167	5	⋯	⋯
ser243	15077	3, 5	⋯	⋯
	15619	3, 5	⋯	⋯
ser254	⋯	⋯	0744040301	6
	⋯	⋯	0744040401	6
ser267	14042	1	⋯	⋯
ser273	14042	1	⋯	⋯
ser318	⋯	⋯	0722610201	3
ser335	⋯	⋯	0111260101	⋯
	⋯	⋯	0111260701	⋯
	⋯	⋯	0212480701	⋯
ser359	⋯	⋯	0651850501	⋯
ser363	⋯	⋯	0724810201	3
	⋯	⋯	0724810401	3
ser382	⋯	⋯	0764910201	⋯
ser401	⋯	⋯	0693750101	⋯
ser451	⋯	⋯	0111180201	⋯

Notes. (1) *Chandra*/ACIS-I detector. (2) *XMM-Newton*/MOS data. (3) Observations chosen to be closest in time to the *NuSTAR* data. (4) The source is on the *Chandra*/ACIS-S2 chip. (5) The source is on the *Chandra*/ACIS-S3 chip. (6) See Ricci et al. (2016) for details on data reduction and spectral extraction.

3.2. XMM-Newton and Chandra

For the ECDF-S and COSMOS fields, we employed all spectra reduced and extracted by previous works. Specifically, for the deep ECDF-S field, we used *Chandra* data reduced by Lehmer et al. (2005) and Xue et al. (2016), and extracted spectra following procedures discussed in Del Moro et al. (2014). For *ecdfs20*, which only has an *XMM-Newton* spectrum, the data reduction and spectral extraction are from Ranalli et al. (2013) and Georgantopoulos et al. (2013). For the COSMOS field, we use spectra reduced and extracted for *XMM-Newton* by Mainieri et al. (2007) and for *Chandra* by Lanzuisi et al. (2013), with the only exception being source *cosmos330*, for which a spectrum from the COSMOS-Legacy field has been used (Marchesi et al. 2016).

For the serendipitous survey fields, we reduced and extracted the *Chandra* and *XMM-Newton* data. In the selection of archival observations, we only use data from observations in which CCD detectors are primary instruments (i.e., we exclude *Chandra* grating observations). In the case of *XMM-Newton*, we almost always only use data from PN, the exception being *ser107*, which was located in a CCD gap of the PN camera. For this source, we use the MOS data. For the *Chandra* data, we used both ACIS-S and ACIS-I detectors whenever available (see Table 3 for details). When multiple archival data sets were available, we chose the data closest in time to the *NuSTAR* observation, if available, in order to minimize source variability. Table 3 reports the selected observations for each source.

We reduced the *Chandra* data using CIAO v. 4.7 with[28] CALDB v. 4.6.7. We re-processed the data using the CHANDRA_REPRO script to produce new re-calibrated level = 2 event files. The spectral extraction was done with the script SPECEXTRACT, which automates the creation of source and background spectral files and the relative ARF and RMF. The source and background spectral extractions were performed on user-selected circular and annular concentric regions, respectively, in order to maximize the source flux and avoid point-source contamination to background measurements. We finally combined the resulting spectra using the FTOOLs script ADDASCASPEC, available in HEASOFT v. 6.16,[29] and produced combined RMFs and ARFs using the tasks ADDRMF and ADDARF. The resulting exposure times and collected net-source counts are reported in Table 4.

For the *XMM-Newton* data, we used SAS v14.0.0.[30] For each observation, we screened the event files for time intervals impacted by soft proton flares by adopting an observation-dependent 10–12 keV count-rate threshold (0.4 ± 0.1 counts s^{-1} being the average and 1σ standard deviation of the applied threshold), above which data were removed. For the spectral extraction and creation of response files, we followed the standard procedures outlined in the *XMM-Newton* science threads.[31] We extracted events with pattern $\leqslant 4$ for the PN camera and $\leqslant 12$ for the MOS detectors. We combined the MOS1 and MOS2 spectra using the SAS task EPICSPECCOMBINE. For sources with more than one data set, we produced combined source spectra, background spectra, ARF, and RMF, as per the *Chandra* data. Exposure times and net-source counts for each source are reported in Table 4.

For the EGS field, *Chandra* data products from Goulding et al. (2012) have been used. The spectral extraction, specifically carried out for this work,[32] has been performed using SPECEXTRACT for each individual observation. Background regions were taken from annuli with $1.3 * r_{90,\mathrm{psf}} - 3.0 * r_{90,\mathrm{psf}}$ (with the latter being the radius enclosing 90% of the point-spread function) with other detected sources masked out. Spectra and backgrounds were combined for the different observations using COMBINE_SPECTRA in CIAO.

4. Data Analysis

We performed the spectral analysis via XSPEC v. 12.8.2 using the Cash statistic (Cash 1979) with the direct background subtraction option (Wachter et al. 1979). In the limit of a large number of counts per bin, the distribution of this statistic, called the W statistic (Wstat), approximates the χ^2 distribution with N–M degrees of freedom (dof, where N is the number of independent bins and M is the number of free parameters). We performed all our modeling with spectra binned to five net-counts (i.e., background subtracted) per bin, with the exception

[28] http://cxc.harvard.edu/ciao4.7/
[29] http://heasarc.gsfc.nasa.gov/docs/software/lheasoft/
[30] https://www.cosmos.esa.int/web/xmm-newton/sas
[31] http://www.cosmos.esa.int/web/xmm-newton/sas-threads
[32] CIAO v. 4.8 with CALDB v. 4.7.0 has been used.

Table 4
Spectral Extraction Parameters

NuSTAR ID	*NuSTAR* FPMA			*NuSTAR* FPMB			*Chandra*			*XMM-Newton*		
	net cts	exp[a]	r_{ex}[b]	net cts	exp[a]	r_{ex}[b]	net cts	exp[a]	Ref.	net cts	exp[a]	Ref.
cosmos97	246	57.1	60	268	57.0	60	392	47.1	3	675	40.1	2
cosmos107	26	52.8	25	21	52.7	25	…	…	…	73	20.5	2
cosmos129	21	71.5	30	27	71.5	25	46	186.7	3	54	57.1	2
cosmos130	111	49.6	40	103	49.5	40	…	…	…	1498	37.5	2
cosmos145	109	103.2	50	77	103.1	50	603	189.5	3	329	45.8	2
cosmos154	114	100.1	45	119	99.5	45	185	189.4	3	…	…	…
cosmos155	531	104.8	60	534	104.1	55	5127	184.8	3	3520	46.1	2
cosmos178	110	97.8	60	67	97.7	40	402	93.2	3	218	32.0	2
cosmos181	75[c]	95.0	40	55[c]	94.9	40	62	92.4	3	99	53.5	2
cosmos194	86	73.1	35	182	99.1	40	3174	185.9	3	2383	53.3	2
cosmos195	82	48.7	40	100	48.7	40	…	…	…	682	17.5	2
cosmos206	149	46.6	45	101	46.6	30	1920	91.5	3	2957	43.3	2
cosmos207	58	49.7	35	65	49.6	45	…	…	…	175	18.7	2
cosmos216	45	51.5	45	34	51.4	40	88	140.5	3	104	56.2	2
cosmos217	44	114.4	20	42	114.3	20	945	188.5	3	821	63.5	2
cosmos218	500	98.6	55	470	98.5	55	2170	88.9	3	3417	39.6	2
cosmos229	56	98.6	25	53	98.5	25	316	133.9	3	1096	60.8	2
cosmos232	75	111.8	40	38	111.7	20	240	185.6	3	115	63.7	2
cosmos249	23	52.0	25	28	51.9	20	…	…	…	138	32.9	2
cosmos251	74	78.0	30	51	52.1	30	…	…	…	721	29.1	2
cosmos253	71	52.9	40	43	52.8	40	…	…	…	191	32.5	2
cosmos263	239	76.7	55	184	76.5	55	…	…	…	514	12.9	2
cosmos272	110	106.4	40	113	106.2	40	…	…	…	189	36.9	2
cosmos282	158	83.1	40	177	82.9	45	…	…	…	2790	46.0	2
cosmos284	38	52.6	40	43	52.5	30	…	…	…	1159	73.3	2
cosmos287	88	111.7	30	93	107.1	40	…	…	…	946	31.3	2
cosmos296	27	45.6	20	38	45.5	25	658	91.6	3	893	45.9	2
cosmos297	78	45.6	30	50	45.5	35	402	93.2	3	1056	64.3	2
cosmos299	167	110.7	40	176	110.5	40	…	…	…	111	38.2	2
cosmos322	114	99.1	40	93	99.0	40	…	…	…	613	51.8	2
cosmos330	131	52.8	55	105	52.7	55	183	147.9	1	80	39.9	2
ecdfs5	82	89.5	30	127	89.1	40	532	240.3	4,5	…	…	…
ecdfs20	149	192.6	20	136	192.6	20	1204	357.9	4,5	3743	1862.2	6
ecdfs51	170	185.8	45	179	185.6	45	2079	245.6	4,5	…	…	…
egs1	180	149.4	55	166	205.5	35	2894	197.5	7	…	…	…
egs9	453	302.8	50	387	354.2	40	4195	719.0	7	…	…	…
egs26	593	400.5	55	578	399.6	55	2531	683.9	7	…	…	…
egs27	294	300.2	55	250	251.3	50	10696	683.9	7	…	…	…
egs32	614	390.4	60	484	389.6	40	5448	683.9	7	…	…	…
ser37	267	49.1	20	106	30.1	15	…	…	…	956	28.7	8
ser77	104	27.3	55	97	27.3	45	160	31.7	8	42	12.5	…
ser97	290	120.8	35	344	120.6	35	…	…	…	…	…	…
ser107	80	127.6	30	130	127.4	50	…	…	…	50[d]	49.8[d]	8
ser148	4105	38.7	90	4299	42.4	85	…	…	…	6316	10.9	8
ser153	321	142.5	50	327	221.7	50	…	…	…	5	5.8	8
ser184	635	943.6	40	1002	974.7	45	5717	381.9	8	251	21.2	8
ser213	637	94.3	55	510	94.1	45	…	…	…	52	11.3	8
ser215	99	59.4	45	74	59.3	35	55	5.0	8	…	…	…
ser235	211	123.1	50	169	122.8	50	…	…	…	…	…	…
ser243	172	69.2	20	125	69.1	20	674	90.4	8	…	…	…
ser254	495	90.2	45	795	142.1	50	…	…	…	439	36.5	9
ser261	11	22.4	25	14	22.4	35	…	…	…	…	…	…
ser267	27	20.4	40	38	20.3	35	45	5.0	8	…	…	…
ser273	521	20.4	70	473	20.3	60	1028	5.0	8	…	…	…
ser285	33	23.2	35	33	23.1	35	…	…	…	…	…	…
ser318	123	67.7	50	104	68.0	40	…	…	…	129	3.0	8
ser335	93	49.2	40	87	49.1	35	…	…	…	996	23.9	8
ser359	56	23.9	50	58	23.8	60	…	…	…	151	18.1	8
ser363	293	224.7	50	119	110.1	50	…	…	…	898	32.8	8
ser382	33	49.4	30	32	50.0	25	…	…	…	190	19.4	8
ser401	17	21.3	20	21	21.3	20	…	…	…	158	22.8	8
ser409	23	32.3	25	26	32.2	20	…	…	…	…	…	…
ser451	261	95.1	60	173	98.7	60	…	…	…	5	7.6	8

Notes.
[a] Exposure time in ks.
[b] Extraction radius in arcseconds.
[c] Counts in the energy range 4.5–24 keV. See the Appendix for details on this source.
[d] MOS spectrum; the source falls in a chip gap in PN.

References. (1) Marchesi et al. (2016), (2) Mainieri et al. (2007), (3) Lanzuisi et al. (2013), (4) Lehmer et al. (2005), (5) Xue et al. (2016), (6) Ranalli et al. (2013), (7) Goulding et al. (2012), (8) this work, and (9) data reduction as in Ricci et al. (2016).

of sources with a low number of counts (i.e., $\lesssim$50 counts from both *NuSTAR* detectors), for which we resorted to a finer binning of one net-count per bin.

The spectral modeling has been performed: (a) for the *NuSTAR*-only data, in the energy range 3–24 keV, assuming a power law, with absorption and reflection (Section 4.1), and (b) jointly together with *XMM-Newton* and *Chandra* over the broader 0.5–24 keV energy band, using more complex models (Section 4.2).

Notice that, despite the spectral analysis being performed up to 24 keV, on average, our spectra are sensitive to slightly lower energies. The median and semi-interquartile range for the highest energy bin in the FPMA and FPMB spectra are 19.6 $\pm$ 3.0 keV and 17.9 $\pm$ 2.4 keV, respectively.

4.1. NuSTAR Spectral Analysis

For the *NuSTAR*-only analysis (3–24 keV), we first use a power-law model. We freeze the cross-calibration between FPMA and FPMB because, given the few percent level of accuracy measured by Madsen et al. (2015) and the limited counts of the majority of our spectra (up to a few hundreds) we do not expect to distinguish these small calibration levels (i.e., the statistical uncertainties exceed the systematic ones). The left panel of Figure 3 presents the power-law photon index Γ values plotted against the net counts in the 3–24 keV band. The Γ values are, on average, flatter than the canonical 1.8–2 values (e.g., Piconcelli et al. 2005; Dadina 2008) with a mean (median) of 1.5 (1.6). The distribution of Γ is reported by the black histogram in the right-upper panel. Spectra with fewer counts than the median have slightly flatter photon indices than high-count sources, $\langle\Gamma_{\rm low}\rangle = 1.4 \pm 0.2$ compared to $\langle\Gamma_{\rm high}\rangle = 1.7 \pm 0.3$. The average hardening of faint sources agrees with the shape of the CXB in approximately the same energy range (Marshall et al. 1980), as already found at lower energies (e.g., Mushotzky et al. 2000; Brandt et al. 2001; Giacconi et al. 2001). There is one notable outlier with a negative Γ value—the CT thick source in the COSMOS field reported by C15 (*cosmos330* in Table 2). The average flat values of Γ point to a more complex spectral shape in the *NuSTAR* energy band.

In order to identify a more suitable model that would bring the power-law photon indices to the canonical 1.8–2 values, we explored two modifications to the simple power-law model. We first allowed for low-energy photoelectric absorption by the circumnuclear interstellar matter, using the ZWABS model in XSPEC. Given the 3 keV lower bound of the *NuSTAR* energy range, this model modification did not appreciably change the distribution of Γ, producing a median of 1.6 and only a few outliers ($\sim$10% of the sample) at values much larger than 3 (see red dashed histogram in Figure 3). An alternative modification is the inclusion, beside the simple power-law component, of an additional cold Compton-reflection component to account for the disk/torus reflectors. This component is particularly important in the *NuSTAR* hard-energy band. We used the PEXRAV model (Magdziarz & Zdziarski 1995), which assumes that the reflector is an infinite slab with infinite optical depth illuminated by the primary power-law continuum, subtending an angle $\Omega = 2\pi R$, where R is the reflection parameter. For a source of isotropic emission, $\Omega = 2\pi$; hence $R = 1$. We tied both the photon index and the normalization of the reflection model to those of the primary power law and let R vary. In our modeling throughout the paper, we set this parameter in XSPEC to be negative; as for PEXRAV, this will switch on the reflection-only solution as opposed to the reflection+power-law solution activated by positive values. Throughout the text, we quote the absolute value of the parameter. We left the abundance at its default solar value, $\cos\theta = 0.45$ (i.e., inclination angle $\theta \sim 63°$, the default value in the model), and set the exponential cut-off (E_c) for the incident power-law primary continuum at 200 keV (as assumed by G07 and consistent with recent determinations by *NuSTAR*; see Fabian et al. 2015 for a compilation). This additional component shifts the mean and median photon index to higher values ($\Gamma = 1.8$ and $\Gamma = 1.7$, respectively), but at the cost of increasing the dispersion of the distribution (see blue histogram in Figure 3). There is no trend in the median Γ with the number of counts—except for the dispersion, with low-count sources having an interquartile range of 1.2, as opposed to high-counts sources having an interquartile range of 0.6. Histograms of the Γ distribution for the three models are reported in the right panels of Figure 3.

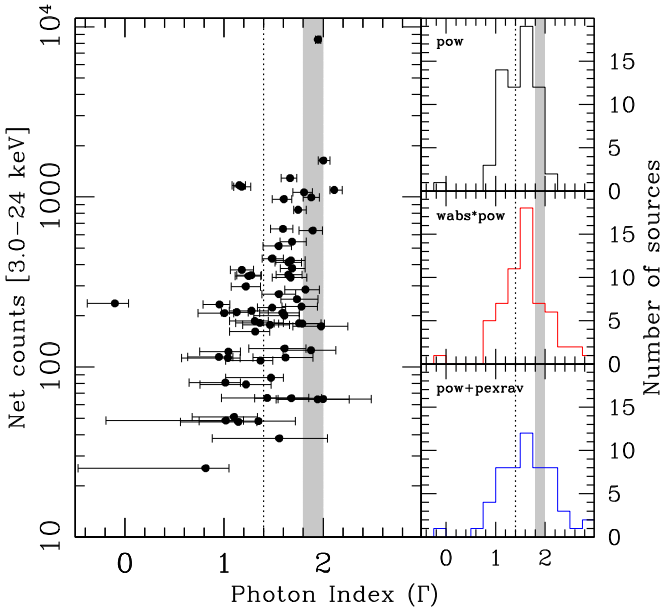

Figure 3. Left panel: 3–24 keV net counts vs. photon index for the *NuSTAR*-only joint fit derived using a power-law model (black dots). Right panels (from top to bottom): black, red, and blue histograms report the distribution for the power-law, absorbed power-law, and power-law plus reflection component models, respectively. Gray regions represent the canonical range of Γ values measured in the literature for the power-law component. The dotted line represents the 3–15 keV slope of the CXB as measured by *HEAO-1* (Marshall et al. 1980).

4.2. Joint Broad Band Analysis

In order to improve the modeling and obtain tighter constraints on the spectral parameters, we added lower-energy data from *XMM-Newton* and *Chandra*, thereby extending the spectral range down to $E = 0.5$ keV (observed frame). Table 4 reports details on the low-energy data used for each source.

We first consider an empirical model (hereafter called *baseline model*), expressed in XSPEC as:

$$\text{CONSTANT} \times \text{WABS}(\text{POWERLAW}_{\rm sc} + \text{ZWABS} \times \text{POWERLAW} + \text{ZGAUSS} + \text{PEXRAV}),$$

where POWERLAW represents the primary coronal component modified at low energies with photoelectric absorption (model

ZWABS) and complemented at high energies with the addition of a cold Compton-reflection component (model PEXRAV). We further add a power law ($\mathrm{POWERLAW_{sc}}$) at low energy to account, when needed, for residual low-energy flux for absorbed sources (hereafter called scattered component) consisting either of primary component flux scattered outside the nuclear absorbing region or of circumnuclear photoionized gas. At high energy, we add a line (ZGAUSS) to account for neutral Fe Kα emission at 6.4 keV produced by the surrounding reflecting cold medium, and let its normalization free to vary. The entire model is modified by photoelectric absorption (WABS) from Galactic interstellar gas using values reported by Kalberla et al. (2005) at the position of each source. The CONSTANT accounts for instrument intercalibration and possible source flux variability, as well allowing for a crude accounting of possible contamination from blended sources inside differing extraction radii. We left the constant free to vary between satellites, but always tied between the two *NuSTAR* FPMs[33] as done in Section 4.1. We left the slope and normalization of the scattered component free to vary. As in Section 4.1, we used the reflection-only component from PEXRAV and tied both Γ and normalization to the corresponding parameters of the primary component. Other PEXRAV parameters are set to the default values as reported in Section 4.1. In this way, our fits with the baseline model are performed with five free parameters. In case of a joint fit performed with one or two additional low-energy data sets, one or two intercalibration constants need to be accounted as additional free parameters, respectively. Furthermore, in the case of sources with a soft-excess component, two additional free parameters need to be considered for the slope and normalization of the scattered component. In order to speed up our modeling, which can be quite time-consuming using PEXRAV, the error estimation on all parameters was obtained with the reflection strength parameter R and calibration constants fixed to their best-fit values. For error estimation in R, we left only $N_{\rm H}$, Γ, and normalization of the primary power-law component free to vary. Best-fit spectral parameters are reported in Table 5, along with fluxes in the 8–24 keV and 3–24 keV bands, and 10–40 keV unabsorbed and intrinsic coronal luminosities inferred from the best-fit baseline model (see Section 4.4 for details). Figure 4 shows broadband spectra for four sources, along with their best-fit model. For the few sources exhibiting extreme Γ values below 1.3 or above $\sim$2.5 or reflection parameters larger than $\sim$10, we redid the fits with Γ fixed to 1.8. These sources are *cosmos129*, *cosmos232*, *cosmos253*, *cosmos282*, *ser285*, *ser77*, and *ser261*. In three cases, mainly unabsorbed sources with high-quality spectra, the baseline parameterization in the soft- (*ser148*) and broadband (*ser37, egs26*) was inadequate. Indeed, in these energy ranges, absorbed power-law models return slopes in the range $\Gamma = 0.2$–1.2 with very little absorption. We therefore further modified the absorbed primary power law by further applying absorption from a partial covering cold (ZPCFABS in XSPEC) or partially ionized (ZXIPCF) medium. Details on these sources are reported in the Appendix.

[33] For the 58 sources with low-energy spectral data, the difference between the estimated best-fit constants is reasonably low, being smaller than a factor of $\sim$2 for the majority of the sources (50). Four sources (*cosmos129*, *cosmos229*, *cosmos297,* and *ser77*) show variations larger than a factor of 2–3 in both *XMM-Newton* and *NuSTAR,* clearly pointing to source variability as the main cause of discrepancy. The remaining four sources, *cosmos249*, *cosmos263*, *ser148,* and *ecdfs5,* have variations by factors of 2–4, with the latter showing the largest variation that is possibly due to contamination from a nearby source (see the Appendix for details).

4.3. Absorption and Photon Index from the Primary Power Law

The distribution of the measured Γ peaks at around 1.8–2, with a mean value of 1.89 ± 0.26, as reported in Figure 5. Best-fit column density values range from $\lesssim 10^{21}\,\mathrm{cm^{-2}}$ to $\gtrsim 10^{24}\,\mathrm{cm^{-2}}$. We have upper limits for 23 sources. Twenty are unabsorbed sources with $N_{\rm H}$ upper limits $< 10^{22}\,\mathrm{cm^{-2}}$. The two remaining sources have $N_{\rm H}$ upper limits reaching into the heavily absorbed regime ($\sim 10^{23}$–$10^{24}\,\mathrm{cm^{-2}}$). These sources, *ser285* and *ser235*, have low-count *NuSTAR* data and no lower energy data available. For only one source with *NuSTAR*-only data (*ser409*) can we not constrain its $N_{\rm H}$ value even when fixing $\Gamma = 1.8$. For 17 sources, $\sim$27% of the sample, we measure $N_{\rm H} \geqslant 10^{23}\,\mathrm{cm^{-2}}$. Two sources ($\sim$3% of the sample), *cosmos330* and *ser261*, exhibit CT column densities. The former is the CT AGN discovered by C15. Figure 5 shows Γ as a function of intrinsic $N_{\rm H}$. Error bars in Γ tend to be larger for obscured sources (i.e., $N_{\rm H} \gtrsim 10^{22}\,\mathrm{cm^{-2}}$).

4.4. Luminosity in the 10–40 keV Energy Band

In the last two columns of Table 5, we report the 10–40 keV luminosities from the baseline model. They are unabsorbed luminosities ($L_{\rm u,X}$, penultimate column) and intrinsic luminosities ($L_{\rm i,X}$, last column). The unabsorbed luminosity is estimated by simply removing the Galactic and intrinsic absorption components from the best-fit baseline model. The intrinsic coronal luminosities are computed from the unabsorbed coronal power-law component by simply removing the reflection contribution to the best-fit baseline model. The uncertainties in $L_{\rm i,X}$ due to parameter degeneracy in our modeling are estimated by fitting the baseline model with R fixed to its lower and upper error bounds.

In the context of the baseline parameterization, $L_{\rm i,X}$ is supposed to reflect more closely the true X-ray radiative output of the primary (direct) X-ray emitting nuclear source. Notice, though, that the planar geometry assumed in PEXRAV is an approximate description of the cold reflector—which, according to unification schemes, has a toroidal geometry. In any case, in the 10–40 keV band, the additional reflection contribution can become relevant compared to the intrinsic coronal one, especially for sources with low luminosity and large reflection strengths. Including the reflection term in the luminosity calculation may lead to a "double counting" of the intrinsic X-ray radiative output. Indeed, in this case, the estimate of $L_{\rm u,X}$ would include both the primary coronal power-law component and the primary coronal photons reflected from the circumnuclear material back to the observer. This overestimation of the intrinsic luminosity is negligible (10%–30% for $R = 1$–6) in the 2–10 keV band where the reflection component is a few percent of the primary emission. The upper panel of Figure 6 shows, for the 10–40 keV band, the overestimate of the "unabsorbed luminosities," including the reflection component compared to the intrinsic

Table 5
Best-fit Parameters for Baseline Model

NuSTAR ID	stat	dof	Γ	$\log N_{\rm H}$[a]	R	S_{8-24}[b]	S_{3-24}[b]	$\log L_{\rm u,X}$[c]	$\log L_{\rm i,X}$[d]
cosmos97	257.1	262	$2.07^{+0.08}_{-0.08}$	$22.62^{+0.04}_{-0.04}$	$5.89^{+1.75}_{-1.41}$	3.8	5.4	43.2	$42.62^{+0.03}_{-0.04}$
cosmos107	19.0	16	$1.74^{+0.71}_{-0.52}$	$23.63^{+0.29}_{-0.30}$	<0.91	0.9	1.3	44.4	$44.36^{+0.00}_{-0.20}$
cosmos129	16.0	24	1.8	$23.84^{+0.11}_{-0.07}$	<0.32	0.5	0.7	44.4	$44.42^{+0.00}_{-0.04}$
cosmos130	256.1	247	$1.87^{+0.06}_{-0.05}$	<21.41	$0.39^{+0.36}_{-0.18}$	1.6	2.5	45.4	$45.14^{+0.08}_{-0.19}$
cosmos145	150.6	170	$1.71^{+0.11}_{-0.08}$	$21.97^{+0.06}_{-0.06}$	$0.83^{+1.64}_{-0.73}$	0.7	1.0	43.8	$43.58^{+0.08}_{-0.20}$
cosmos154	76.3	70	$1.80^{+0.38}_{-0.21}$	$23.55^{+0.09}_{-0.08}$	<0.34	1.6	2.1	43.5	$43.51^{+0.00}_{-0.02}$
cosmos155	788.7	792	$2.03^{+0.01}_{-0.02}$	<20.09	$1.24^{+0.27}_{-0.38}$	3.3	5.3	44.3	$44.06^{+0.01}_{-0.03}$
cosmos178	143.9	127	$1.46^{+0.11}_{-0.08}$	$21.00^{+0.24}_{-0.82}$	<1.96	0.7	1.0	43.6	$43.55^{+0.00}_{-0.21}$
cosmos181	38.0	45	$2.10^{+0.16}_{-0.14}$	$23.91^{+0.09}_{-0.09}$	$0.76^{+0.84}_{-0.37}$	1.0	1.2	42.8	$42.69^{+0.05}_{-0.00}$
cosmos194	581.2	587	$1.79^{+0.03}_{-0.02}$	<20.93	$0.38^{+0.15}_{-0.15}$	1.7	2.6	45.2	$44.94^{+0.04}_{-0.04}$
cosmos195	139.3	138	$1.61^{+0.06}_{-0.08}$	$21.48^{+0.21}_{-0.50}$	$0.31^{+0.51}_{-0.22}$	2.4	3.7	45.5	$45.33^{+0.12}_{-0.26}$
cosmos206	547.4	571	$1.77^{+0.03}_{-0.02}$	<20.89	$0.23^{+0.16}_{-0.13}$	2.3	3.6	45.2	$45.04^{+0.03}_{-0.05}$
cosmos207	57.6	50	$1.70^{+0.16}_{-0.07}$	<21.46	$3.88^{+4.84}_{-1.56}$	2.0	2.7	44.5	$43.85^{+0.08}_{-0.33}$
cosmos216	23.8	41	$1.75^{+0.16}_{-0.15}$	$23.78^{+0.23}_{-0.26}$	$1.97^{+1.33}_{-1.39}$	1.0	1.2	44.4	$43.90^{+0.14}_{-0.06}$
cosmos217	321.3	267	$1.85^{+0.07}_{-0.07}$	$22.42^{+0.05}_{-0.05}$	<0.40	0.5	0.9	45.0	$44.91^{+0.05}_{-0.21}$
cosmos218	674.8	695	$1.90^{+0.02}_{-0.02}$	<20.17	$1.17^{+0.30}_{-0.11}$	3.6	5.5	44.3	$44.02^{+0.00}_{-0.02}$
cosmos229	231.4	221	$2.04^{+0.05}_{-0.03}$	<20.51	$2.71^{+0.67}_{-0.61}$	0.8	1.1	43.7	$43.20^{+0.00}_{-0.00}$
cosmos232	62.3	76	1.8	$23.41^{+0.06}_{-0.06}$	$0.58^{+0.27}_{-0.30}$	0.7	0.9	44.5	$44.27^{+0.04}_{-0.03}$
cosmos249	23.4	27	$1.98^{+0.36}_{-0.61}$	$23.56^{+0.14}_{-0.18}$	<0.95	1.0	1.4	43.3	$43.30^{+0.00}_{-0.03}$
cosmos251	138.0	127	$2.37^{+0.07}_{-0.05}$	<21.17	$1.17^{+0.88}_{-0.49}$	0.8	1.3	44.8	$44.31^{+0.06}_{-0.22}$
cosmos253	49.5	52	1.8	$22.68^{+0.08}_{-0.08}$	$4.99^{+5.19}_{-1.43}$	1.4	1.8	43.4	$42.84^{+0.03}_{-0.15}$
cosmos263	160.8	153	$1.88^{+0.05}_{-0.03}$	<21.32	$0.11^{+0.17}_{-0.10}$	1.7	2.8	45.3	$45.23^{+0.04}_{-0.09}$
cosmos272	81.9	68	$1.35^{+0.16}_{-0.14}$	$22.62^{+0.12}_{-0.11}$	$0.02^{+0.39}_{-0.00}$	1.1	1.6	44.4	$44.39^{+0.00}_{-0.06}$
cosmos282	390.2	377	1.8	<20.39	$0.42^{+0.18}_{-0.18}$	1.5	2.3	44.3	$44.17^{+0.00}_{-0.00}$
cosmos284	184.4	186	$2.05^{+0.08}_{-0.09}$	$21.87^{+0.07}_{-0.06}$	$1.30^{+1.66}_{-0.84}$	0.9	1.4	44.4	$44.02^{+0.17}_{-0.25}$
cosmos287	162.3	164	$2.33^{+0.08}_{-0.08}$	<21.13	$1.24^{+1.01}_{-0.54}$	0.7	1.2	44.2	$43.84^{+0.02}_{-0.03}$
cosmos296	202.5	234	$2.15^{+0.09}_{-0.07}$	<21.36	$1.57^{+1.06}_{-0.80}$	0.8	1.3	44.8	$44.22^{+0.08}_{-0.07}$
cosmos297	272.9	247	$1.98^{+0.10}_{-0.07}$	$21.99^{+0.05}_{-0.04}$	$1.55^{+2.11}_{-0.94}$	1.3	2.0	43.9	$43.58^{+0.04}_{-0.04}$
cosmos299	99.1	71	$2.16^{+0.06}_{-0.09}$	$23.67^{+0.10}_{-0.05}$	$0.28^{+0.20}_{-0.21}$	1.7	2.3	44.2	$44.09^{+0.02}_{-0.09}$
cosmos322	151.9	137	$1.96^{+0.10}_{-0.08}$	$21.74^{+0.06}_{-0.07}$	$2.58^{+1.67}_{-1.08}$	1.1	1.5	43.8	$43.32^{+0.03}_{-0.03}$
cosmos330	81.2	81	$1.57^{+0.55}_{-0.57}$	$24.13^{+0.11}_{-0.21}$	$0.22^{+0.30}_{-0.17}$	3.6	3.8	42.6	$42.52^{+0.01}_{-0.00}$
ecdfs5	151.7	104	$1.90^{+0.08}_{-0.07}$	$20.87^{+0.22}_{-0.51}$	$3.17^{+11.26}_{-2.09}$	1.2	1.8	43.0	$42.56^{+0.03}_{-0.04}$
ecdfs20	695.6	717	$1.99^{+0.05}_{-0.07}$	$23.02^{+0.02}_{-0.03}$	$0.74^{+0.15}_{-0.15}$	1.1	1.6	44.8	$44.46^{+0.03}_{-0.03}$
ecdfs51	318.2	229	$1.98^{+0.06}_{-0.05}$	<21.20	$1.05^{+0.93}_{-0.60}$	0.7	1.1	44.5	$44.19^{+0.02}_{-0.03}$
egs1	220.1	268	$1.84^{+0.04}_{-0.05}$	$20.93^{+0.31}_{-0.64}$	$0.24^{+0.47}_{-0.12}$	0.8	1.3	44.7	$44.57^{+0.01}_{-0.03}$
egs9	438.4	459	$1.80^{+0.06}_{-0.04}$	$22.72^{+0.02}_{-0.02}$	<0.28	1.3	2.2	44.1	$44.13^{+0.00}_{-0.03}$
egs26[e]	424.4	429	$1.56^{+0.05}_{-0.03}$	$21.06^{+0.12}_{-0.16}$	<0.68	1.4	2.0	43.4	$43.37^{+0.00}_{-0.09}$
egs27	424.9	411	$2.30^{+0.02}_{-0.02}$	<20.56	$1.06^{+0.21}_{-0.31}$	0.9	1.5	44.4	$44.00^{+0.01}_{-0.01}$
egs32	458.6	462	$1.66^{+0.03}_{-0.03}$	$21.62^{+0.09}_{-0.08}$	<0.07	0.8	1.4	44.7	$44.71^{+0.00}_{-0.01}$
ser37[f]	223.3	219	1.8	<20.58	$1.78^{+0.55}_{-0.84}$	17.7	23.7	42.7	$42.48^{+0.06}_{-0.05}$
ser77	64.9	66	1.8	$21.93^{+0.09}_{-0.07}$	$2.00^{+1.05}_{-0.95}$	3.6	5.2	43.6	$43.29^{+0.03}_{-0.03}$
ser97	93.7	95	$2.25^{+0.32}_{-0.18}$	$23.06^{+0.24}_{-0.22}$	<1.40	1.7	3.1	43.4	$43.39^{+0.00}_{-0.11}$
ser107	27.6	38	$1.48^{+0.36}_{-0.23}$	$23.21^{+0.27}_{-0.18}$	<4.45	1.4	1.9	43.4	$43.34^{+0.00}_{-0.18}$
ser148[f]	1338.4	1260	$2.51^{+0.02}_{-0.01}$	<19.89	$2.63^{+0.41}_{-0.36}$	47.5	85.7	44.1	$43.80^{+0.02}_{-0.03}$
ser153	98.3	93	$1.84^{+0.26}_{-0.19}$	$23.42^{+0.27}_{-0.32}$	<1.14	1.1	1.8	45.1	$45.11^{+0.00}_{-0.20}$
ser184	461.2	538	$1.73^{+0.03}_{-0.02}$	$20.88^{+0.20}_{-0.22}$	<0.10	0.9	1.5	44.3	$44.35^{+0.00}_{-0.01}$
ser213	183.5	183	$1.96^{+0.14}_{-0.15}$	$23.33^{+0.13}_{-0.12}$	$1.37^{+0.76}_{-0.53}$	5.5	7.5	44.3	$44.05^{+0.06}_{-0.07}$
ser215	36.8	35	$1.97^{+0.06}_{-0.08}$	<21.71	<16.72	0.9	1.5	44.5	$44.29^{+0.06}_{-0.04}$
ser235	64.8	56	$1.79^{+0.37}_{-0.10}$	<24.25	<0.70	1.2	2.0	45.6	$45.65^{+0.00}_{-0.28}$
ser243	152.6	145	$1.35^{+0.11}_{-0.10}$	$23.02^{+0.05}_{-0.05}$	<0.74	3.3	4.6	44.4	$44.43^{+0.00}_{-0.09}$
ser254	261.7	260	$2.28^{+0.08}_{-0.11}$	$22.98^{+0.05}_{-0.06}$	$1.90^{+0.74}_{-0.62}$	3.7	5.9	43.6	$43.33^{+0.04}_{-0.04}$
ser261	15.5	15	1.8	$24.61^{+0.51}_{-0.32}$	$0.37^{+0.95}_{-0.29}$	0.9	1.0	44.6	$44.41^{+0.14}_{-0.19}$
ser267	14.8	14	$2.13^{+0.26}_{-0.23}$	<21.74	$4.09^{+23.63}_{-3.26}$	1.6	2.8	43.0	$42.52^{+0.06}_{-0.13}$
ser273	221.0	276	$1.85^{+0.04}_{-0.03}$	<20.87	<0.19	11.8	21.1	44.7	$44.67^{+0.00}_{-0.04}$
ser285	7.7	9	1.8	<23.99	<17.31	0.9	1.4	44.4	$44.09^{+0.27}_{-0.89}$
ser318	63.9	56	$2.41^{+0.15}_{-0.08}$	<21.79	$0.56^{+0.76}_{-0.30}$	1.2	2.2	45.1	$44.74^{+0.05}_{-0.05}$
ser335	135.6	189	$1.69^{+0.08}_{-0.03}$	<20.82	<1.10	1.4	2.3	43.9	$43.82^{+0.01}_{-0.05}$
ser359	23.8	44	$1.46^{+0.29}_{-0.20}$	$22.56^{+0.18}_{-0.13}$	<13.89	2.2	3.2	43.9	$43.90^{+0.00}_{-0.18}$

Table 5
(Continued)

NuSTAR ID	stat	dof	Γ	$\log N_{\rm H}$[a]	R	S_{8-24}[b]	S_{3-24}[b]	$\log L_{\rm u,X}$[c]	$\log L_{\rm i,X}$[d]
ser363	129.4	205	$1.64^{+0.06}_{-0.07}$	$21.67^{+0.14}_{-0.26}$	<1.56	1.2	1.9	45.1	$45.10^{+0.00}_{-0.07}$
ser382	40.7	42	$1.88^{+0.24}_{-0.20}$	$22.19^{+0.13}_{-0.12}$	$0.75^{+8.43}_{-0.72}$	0.9	1.5	43.3	$43.18^{+0.02}_{-0.16}$
ser401	31.6	31	$1.87^{+0.20}_{-0.18}$	$22.01^{+0.16}_{-0.20}$	<12.95	0.9	1.5	44.5	$44.33^{+0.10}_{-0.22}$
ser409	33.8	30	$1.68^{+0.11}_{-0.06}$	...	$0.71^{+2.99}_{-0.62}$	0.9	1.3	44.9	$44.58^{+0.17}_{-0.51}$
ser451	52.2	66	$1.81^{+0.61}_{-0.10}$	$23.42^{+0.36}_{-0.10}$	<1.11	1.4	2.1	44.4	$44.41^{+0.00}_{-0.15}$

Notes.
[a] $N_{\rm H}$ in units of $\rm cm^{-2}$.
[b] Units of 10^{-13} erg $\rm s^{-1}$ $\rm cm^{-2}$.
[c] Unabsorbed luminosity in the 10–40 keV energy range in units of erg $\rm s^{-1}$. See Section 4.4 for details.
[d] Intrinsic luminosity in the 10–40 keV energy range in units of erg $\rm s^{-1}$. Errors highlight the uncertainty associated with the reflection component modeling. See Section 4.4 for details.
[e] For this source, we further added a partial covering absorber by partially cold material (zpcfabs in XSPEC). See the Appendix for further details.
[f] For this source, we further added a partial covering absorber by partially ionized material (zxipcf in XSPEC). See the Appendix for further details.

luminosities derived from the unabsorbed primary component only. In the lower panel, we report the ratio between these two quantities in order to quantify better the level of overestimation. Here, $L_{\rm u,X}$ can be larger by factors up to ∼2–4 and the majority of those sources are those with best-fit $R > 1$ (red diamonds) at low luminosity (i.e., $L_{\rm i,X} \lesssim 2 \times 10^{44}$ erg $\rm s^{-1}$). This is due to an induced dependence between R and luminosity; if not accounted for, this may lead to a biased view of the relationship between luminosity and reflection strength (see Section 4.5.1 and Figure 8, bottom panels). Notice that few sources at higher luminosities ($\gtrsim 2 \times 10^{44}$ erg $\rm s^{-1}$) have overestimates of a factor of ∼2, even though they have low reflection strengths (i.e., $R < 1$). This is due to the fact that the $L_{\rm u,X}/L_{\rm i,X}$ ratio in the observed 10–40 keV energy range is an increasing function of the redshift[34] and our sample, selected in flux, contains higher-luminosity sources, on average, at higher redshifts.

In order to keep the *baseline* parameterization simple and suitable for low S/N spectra, we did not include a Compton-scattering term, which can become important for the most obscured sources. This may lead to an underestimate of the true luminosity for the most obscured sources. We compared our unabsorbed values with the best-fit values obtained by adding a Compton-scattering term parameterized with CABS for the COSMOS sources with $\log(N_{\rm H}/\rm cm^{-2}) \gtrsim 24$, i.e., those for which we have the best-quality broadband data. We obtained larger luminosities, on average, with values ranging from <0.1 dex for the less obscured sources up to ∼0.4 dex for the most obscured ones. However, CABS approximates the Compton scattering by only accounting for the scattering of the photons outside the beam and neglecting photons reflected by surrounding material into the line of sight. Hence, more appropriate luminosity values may be estimated by accounting for the geometry of the obscurer. For this reason, we compared our values with those obtained with the torus modelings employed in Section 4.6, which self-consistently account for Compton-scattering effects due to the toroidal geometry of the obscurer. We found that, in the range $\log(N_{\rm H}/\rm cm^{-2}) \approx$ 23–24.5, the 10–40 keV luminosity is underestimated, on average, by at most ∼0.1 dex, with only two exceptions in our sample: *cosmos129* and *ser261*. These sources are among the most obscured sources in our sample; for them, we have found $L_{\rm u,X}$ underestimated by 0.2 dex and 0.3–0.4 dex, respectively. No significant difference is found for less obscured sources.

4.5. The Reflection Component

We next estimate the significance of the reflection component in our sources. We first evaluated whether, for the obscured sources ($\log[N_{\rm H}/\rm cm^{-2}] \geqslant 22$), the absorbed spectral shape could be better modeled in the context of a CT scenario in which the primary continuum is completely suppressed and where the only dominant component other than the soft residual scattered one is the pure cold reflection component. Hence, we evaluated a reflection-dominated spectrum obtained by removing the absorbed primary power-law component from the baseline model. Because we are not using χ^2 statistics, we are not able to use an F-test to evaluate the significance of the baseline model over the simpler reflection-dominated one. We therefore based our evaluation on the presence of: (1) a reasonable input power-law photon index for the PEXRAV component of the best-fit parameterization of the reflection-dominated model; (2) a large fraction of scattered flux at low energies for the baseline model[35]; (3) the presence of an Fe Kα emission line with a large equivalent width (EW $\gtrsim$ 1 keV); and (4) large residuals for the best-fit parameterization. Based on these criteria, we did not find clear cases of sources deviating from the baseline model or significantly better parameterized by a reflection-dominated model. Similarly, we did not find scattered fractions in excess of a few percent, the value that is typically found in heavily obscured sources (e.g., Lanzuisi et al. 2015). Moreover, only for *cosmos181* did we obtain Fe Kα EW ∼ 1 keV. Other sources show more moderate EWs. We therefore are unable to discriminate between the two models.

4.5.1. Reflection as a Function of Obscuration, Slope, and Luminosity of the Primary Emission

We measured R for all the sources (see Table 5 column 6) and obtained upper limits for 23 sources. We considered all the

[34] Indeed, the redshift progressively shifts to lower energies (i.e., outside the band) portions of the spectrum where the decreasing primary component still significantly contributes to the total flux.

[35] That is, if we are modeling an intrinsic reflection-dominated source with the baseline model, we obtain an overestimate of this quantity. To check for this, we tied Γ of the scattered component to the primary one.

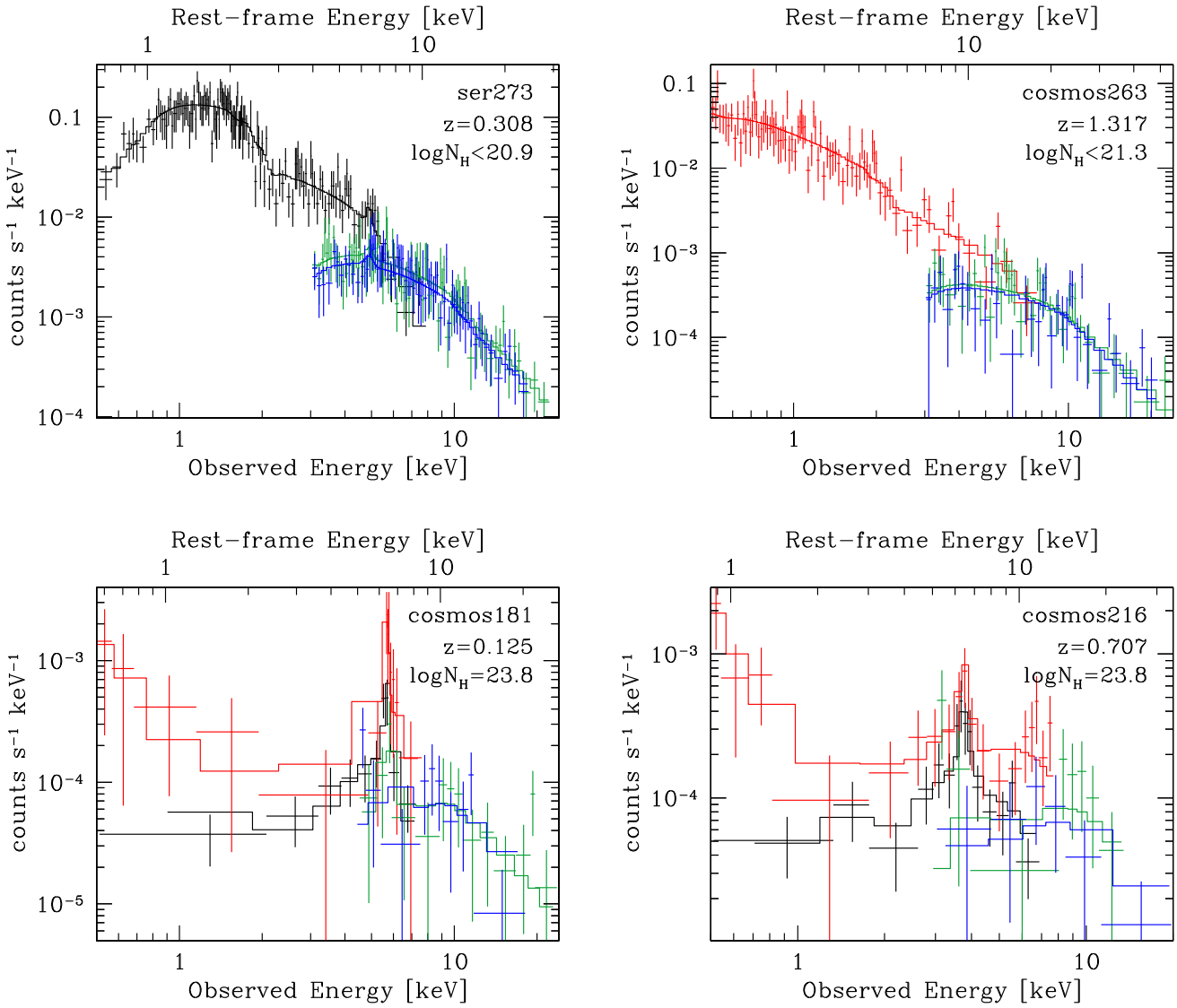

Figure 4. Examples of broadband spectra for four sources with best-fit baseline models (solid lines). Black, red, green, and blue spectra refer to *Chandra*, *XMM-Newton*, *NuSTAR*-FPMA, and *NuSTAR*-FPMB, respectively. Upper/lower spectra are for unabsorbed/absorbed sources. Spectra on the left/right are for sources with redshifts lower/higher than $\langle z \rangle$.

best-fit values with $R < 0.01$ as upper limits. In Figure 7, we report the distribution of R in bins of 0.5 dex.[36]

We investigated how reflection correlates with obscuration and luminosity for the whole sample. Figure 8 presents the reflection parameter as a function of column density (top-left panel) and unabsorbed and intrinsic 10–40 keV luminosity (bottom panels). The color of each point corresponds to redshift, with the redder colors representing the more distant sources. Because ours is a flux-selected sample, more distant (i.e., redder) sources in the R–L_X plane correspond to more luminous, less obscured sources (see R–N_H plane).

There is an apparent tendency for obscured and luminous sources to have, on average, maximum R values smaller than unobscured and less luminous sources.

We investigated and quantified these trends by: (1) computing the Spearman's rank correlation coefficient (ρ) for censored data using the ASURV package v. 1.2 (Lavalley et al. 1992; Feigelson & Nelson 1985; Isobe et al. 1986) and (2) calculating the median $\langle R \rangle$ and its interquartile range (IQR) for the entire sample and the obscured/unobscured and luminous/less luminous subsamples (the separation between the latter being dictated by the median luminosities of the sample, $\log[\langle L_{i,X} \rangle / \mathrm{erg\ s^{-1}}] = 44.06$ and $\log[\langle L_{u,X} \rangle / \mathrm{erg\ s^{-1}}] = 44.35$).

For the latter, we accounted for measurement errors and upper limits in R, $\log(N_H/\mathrm{cm^{-2}})$, and $\log L_{i,X}$ as follows: we performed 10,000 realizations of the sample, each time with respective Gaussian and uniform randomization for each of the parameter best-fit values[37] and the upper limits. In the case of R and $\log N_H$, the latter were randomized from their 90% upper value down to a fixed minimum value of $R = 0.01$ and $\log(N_H/\mathrm{cm^{-2}}) = 20$. For each realization, we computed the median value and IQR, and adopted the averaged values over all the realizations as representative for the sample. The

[36] Notice that the derived R values are obtained by fixing the inclination angle (θ_{incl}) for the reflector to $\theta_{incl} \sim 63°$ (default in Xspec). Assuming lower/larger inclination angles will decrease/increase R. For instance, fixing $\theta_{incl} = 30°$ ($\theta_{incl} = 85°$) would lower (increase) our reported R by 50% (a factor of 2–3).

[37] We assumed a symmetric distribution centered on the parameter value with 1σ standard deviation as the mean of the lower and upper error bars.

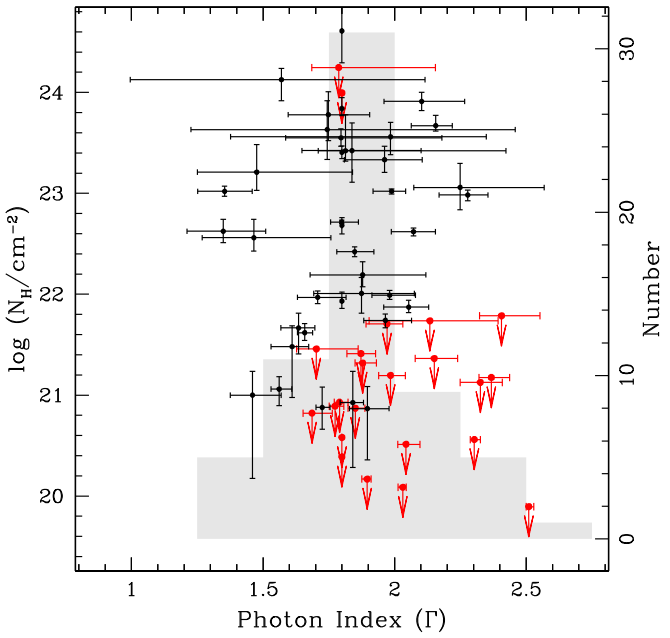

Figure 5. Intrinsic column density (left-hand *y*-axis) vs. photon index from the baseline modeling. Red arrows are 90% c.l. upper limits on N_H. The shaded gray histogram reports the distribution of Γ (right-hand *y*-axis). Data points without error-bars in Γ are sources for which the value of Γ was fixed to a value of 1.8 during the modeling because of poor constraints due to a combination of limited statistics and large column densities.

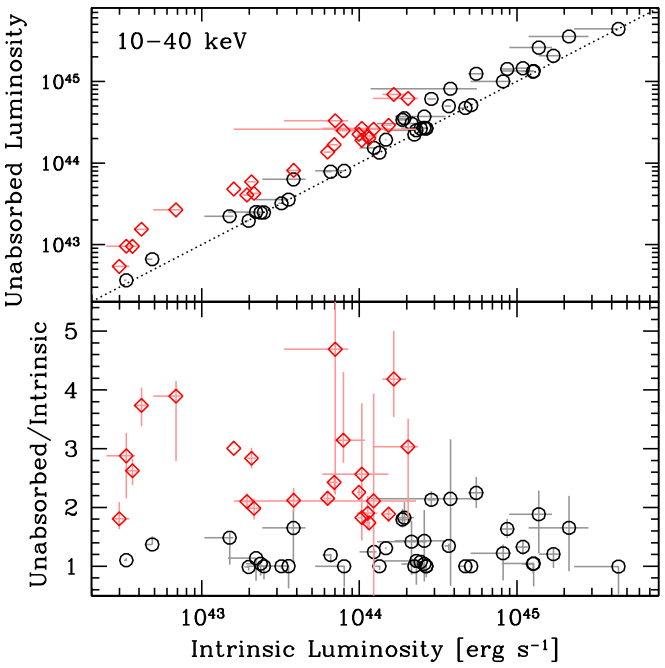

Figure 6. Upper panel: intrinsic 10–40 keV luminosity measured on the coronal primary component only (i.e., unabsorbed luminosity computed after removing the Compton-reflection term) vs. unabsorbed 10–40 keV luminosity measured on the unabsorbed baseline best-fit model (i.e., including the Compton-reflection term). Uncertainties in the baseline spectral modeling are reported in light colors. The dotted line shows a relation with slope 1. Lower panel: ratio between unabsorbed and intrinsic luminosities. Red diamonds show the sources exhibiting $R > 1$.

resulting values are reported in Table 6. Note that accounting for the upper limits may lead to a shift of the lower interquartile bound toward smaller values. Therefore, the lower interquartile range may not reflect the true relative R distributions. The IQR

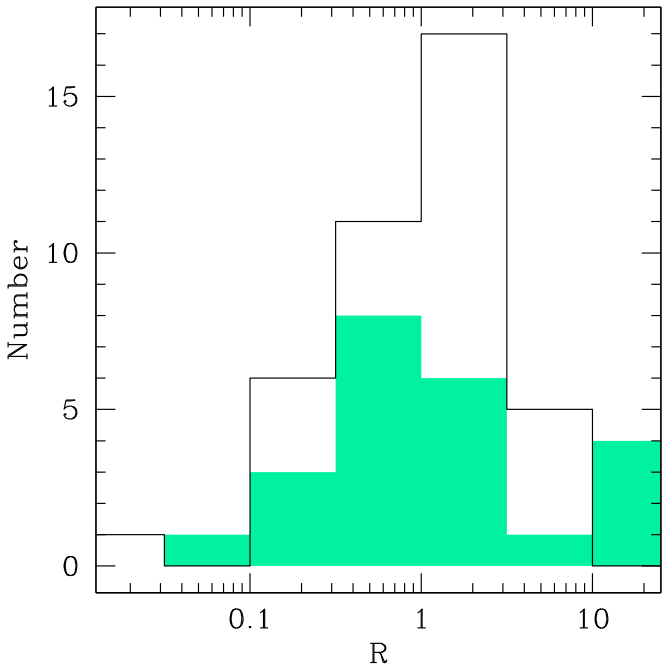

Figure 7. Distribution of measured reflection parameter (black histogram) as obtained from the baseline spectral modeling. The upper limits distribution is reported by the shaded green histogram. The binning is 0.5 dex.

values are reported as shaded areas in Figure 8 for the subsamples and as vertical lines for the entire sample.

For the entire sample, the average median value is $\langle R \rangle = 0.43$ with an interquartile range 0.06–1.50. We find a weak, mildly significant anti-correlation between R and $\log N_H$ with $\rho = -0.25$ and a null hypothesis probability that the two quantities are not related to each other of $p = 0.05$. The median R values for unobscured and obscured samples are 0.67 and 0.28, respectively. Despite the apparent difference, their IQR have quite a large interval of values in common. The difference in the lower values (with unabsorbed sources having larger values) may reflect the fact that the obscured sample has twice as many upper limits as the unobscured sample. We verified that the presence of such a large number of upper limits does not depend on the S/N of the *NuSTAR* spectra. The upper bounds of the interquartile range differ by a factor of ∼1.7. Both categories sample AGN with similar range in luminosities (interquartile range $\log(L_{u,X}/\mathrm{erg\ s^{-1}}) = 43.8$–$44.9$ and $\log(L_{i,X}/\mathrm{erg\ s^{-1}}) = 43.5$–$44.6$). Therefore, the dependence of R on luminosity (see below) should not affect our result. We checked for the possibility that the resulting trend is due to the covariance in our modeling at the highest column densities between the two quantities. We computed the confidence contours for N_H and R for the heavily obscured sources (i.e., $\log(N_H/\mathrm{cm^{-2}}) \geqslant 23$) and we find no significant covariance, with few sources showing a weak covariance that has been found to be either positive (*cosmos181* and *cosmos216*) or negative (*ser243* and *ser254*). If the anti-correlation between R and $\log N_H$ is real, it could be explained by a configuration in which the obscurer absorbs also the reflected component. Hence, a more pronounced reflection is necessary to reproduce the observed high-energy spectral shape. This would bring the reflection parameters to higher values for the obscured AGN ($\log[N_H/\mathrm{cm^{-2}}] \geqslant 22$), in agreement with those derived for the unabsorbed sources. Hence, we estimated R and $\log N_H$ best-fit values by performing modeling on the obscured AGN with a modified baseline model in which

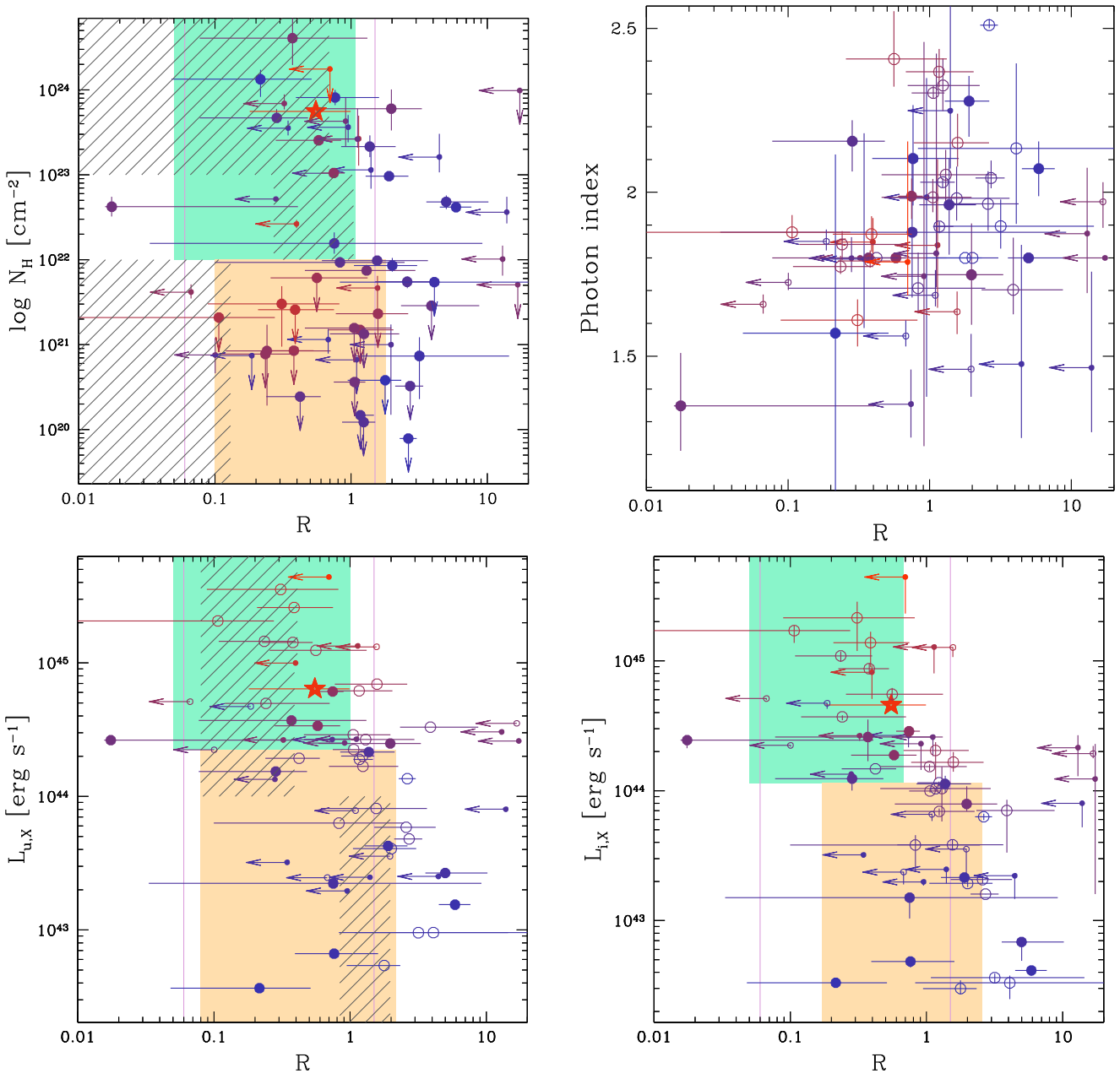

Figure 8. Reflection parameter against N_H (top-left panel), photon index (top-right panel), unabsorbed luminosity $L_{u,X}$ (bottom-left panel), and intrinsic coronal luminosity $L_{i,X}$ (bottom-right panel). Colors reflect the redshift of each source, with redder colors representing more distant objects. In the R vs. L_X and R vs. Γ plots, empty (filled) circles represent unobscured (obscured) AGN. Vertical lines mark the interquartile interval for R in the entire sample. Shaded green (yellow) regions represent the interquartile ranges for obscured (unobscured) and more (less) luminous sources (the latter being separated at a median luminosity). In the R vs. luminosity and R vs. N_H plots, the red star represents the high-redshift quasar detected in the ECDF-S field and analyzed in Del Moro et al. (2014). The hatched regions in the R vs. $L_{u,X}$ represent 90% error range for bins in N_H and L_X, as measured from the stacking analysis performed by DM17 on a large sample of *NuSTAR*-detected sources. Values of interquartile ranges are also reported in Table 6. See Section 4.4 for the definition of $L_{u,X}$ and $L_{i,X}$.

the reflection component is absorbed by the same column density absorbing the power-law continuum. We obtained $\langle R \rangle = 0.14$ and IQR = 0.02–0.93, which are not dissimilar to the values obtained by the baseline model. We also estimated the correlation between the two quantities and obtained $\rho = -0.19$ with $p = 0.147$. Hence, although a weak anti-correlation still persists, it is not significant. We therefore cannot make significant claims about this hypothesis. We mention that accounting for Compton-scattering in our baseline model may affect the determination of R for the most absorbed sources. We measured this for the most obscured sources in the COSMOS subsample (i.e., *cosmos330*, *cosmos181*, *cosmos216,* and *cosmos129*) and found R values that are lower but always in agreement with those from the baseline model within the 1σ uncertainties. The inclusion of a Compton-scattering term will, on average, lower the median R value for the $\log(N_H/\mathrm{cm}^{-2}) \geqslant 22$ sources and increase the disagreement compared to the unobscured sources (i.e., strengthen the anti-correlation).

In our modeling, R may be partially degenerate with Γ. We investigated this induced effect in the $R - \Gamma$ plane (see Figure 8, top right panel). There is a significant correlation between the two quantities with $\rho = 0.54$ and a null-hypothesis probability $p = 10^{-4}$. We find similar trends with obscuration

Table 6
Reflection Parameter: Correlation Coefficient Values, Median, and Interquartile Ranges Relative to Column Density and Luminosities

Parameters	ρ[a]	p[a]	Sample	$\langle R\rangle$[b]	IQR[b]
R	...	...	All	0.43	0.06–1.50
$\log N_{\rm H}$, R	−0.25	0.05	unobscured[c]	0.67	0.10–1.80
			obscured[c]	0.28	0.05–1.07
$\log L_{\rm i,X}$, R	−0.59	$<10^{-5}$	low $L_{\rm i,X}$[d]	1.15	0.17–2.56
			high $L_{\rm i,X}$[d]	0.25	0.05–0.68
$\log L_{\rm u,X}$, R	−0.37	0.0039	low $L_{\rm u,X}$[e]	0.73	0.08–2.17
			high $L_{\rm u,X}$[e]	0.31	0.05–1.00

Notes.
[a] Spearman's rho correlation coefficient (ρ) and null-hypothesis probability (p) calculated for censored data from ASURV package (see Section 4.5.1).
[b] Median ($\langle R\rangle$) and Interquartile range (IQR) values for R computed in each considered sample, accounting for errors and upper limits as explained in Section 4.5.1.
[c] We used a 10^{22} cm^{-2} threshold value.
[d] The median value $\log(\langle L_{\rm u,X}\rangle/{\rm erg\ s^{-1}}) = 44.35$ is adopted as the threshold value.
[e] The median value $\log(\langle L_{\rm i,X}\rangle/{\rm erg\ s^{-1}}) = 44.06$ is adopted as the threshold value.

at a lower significance level. Notice that our evaluation in this case is affected by the small number of sources in the obscured and unobscured sample, as well as, for the obscured sources, by the many sources with $\Gamma = 1.8$ fixed—which we had to exclude from the analysis. Therefore, we cannot draw firm conclusions on this point. A pronounced degree of degeneracy between the two parameters has also been found through spectral stacking analysis in our companion paper (DM17), using a sample three times larger than in this work.

As for the relation with luminosity, we find a significant anti-correlation for both $L_{\rm u,X}$ and $L_{\rm i,X}$ (see Figure 8, bottom panels). The correlation coefficient for the former quantity is $\rho = -0.37$ with $p = 3.9 \times 10^{-3}$, while for the latter it is $\rho = -0.59$ with $p < 1 \times 10^{-5}$. The stronger correlation with $L_{\rm i,X}$ is expected, given that $L_{\rm u,X}$ includes a contribution from the reflection component itself, which partially mitigates the "true" relation. The stronger correlation of $L_{\rm i,X}$–R, compared to $L_{\rm u,X}$–R, reflects also in the median and IQR values, as shown in Table 6. The median and upper IQR bound values for luminous and less luminous sources differ, respectively, by a factor of $\gtrsim$4 and $\gtrsim$2. These trends are not particularly sensitive to the luminosity value adopted to separate the two subsamples: less luminous sources always exhibit more pronounced reflection than luminous ones. For example, changing $L_{\rm i,X}$ threshold values by ±50% translates into a $\gtrsim$3–5 factor difference in median and upper bound R values. A $z = 2$ quasar selected in the *NuSTAR*-ECDF-S field and analyzed in Del Moro et al. (2014) is reported in the plots as the starred data point. This source shows a low degree of reflection, comparable to the luminous/obscured AGN in our sample. Notice that we are using a flux-limited sample. Hence, the more luminous sources are also, on average, the more distant ones. Indeed, those sources brighter than the median intrinsic luminosity of the sample have median redshifts of $\langle z_{hi-z}\rangle \gtrsim 0.9$, while the less luminous ones have $\langle z_{hi-z}\rangle \gtrsim 0.25$. Hence, it is also possible that the main driver of the correlation between luminosity and R is the redshift. With this sample, we are not able to break the degeneracy between luminosity and redshift in order to investigate this scenario.

In our companion paper (DM17), we analyze, through stacking techniques, the average spectral properties of the 182 AGN detected in the medium-deep *NuSTAR* surveys. This sample is three times larger than the one used on that work, with a slight overlap (for one-sixth of the sources) with our sample. The average reflection strength is found to be $R \approx 0.5$ ($\Gamma = 1.8$ fixed), with hard-band detected sources showing a slightly higher value $R \approx 0.7$ (for $\Gamma = 1.8$ fixed, $R < 0.4$ when leaving Γ free to vary). These values are in good agreement with our $\langle R\rangle$ and within the scatter suggested by the interquartile range. The R values derived as a function of unabsorbed luminosity $L_{\rm u,X}$ and column density are in good agreement with those inferred for our sample. This can be seen in Figure 8 (bottom left panel), where the 90% error range in R, accounting for the degeneracy with Γ (i.e., reporting ranges according to the average Γ we measured in our sub-samples), is reported as hatched gray regions.

Our combined analysis of the *NuSTAR* sources gives an indication of the average R values (from DM17) and of their dispersion among different sources (from this work) as a function of luminosity and column density for the intermediate redshift ($\langle z\rangle = 0.5$–1) AGN population.

Our findings are also consistent with previous results showing low levels of reflection for high-redshift quasars (Vignali et al. 1999; Reeves & Turner 2000; Page et al. 2005), although we note that Ricci et al. (2011) found higher levels of reflection from Seyfert 2s than from Seyfert 1s. Figure 8 (bottom panels) shows unobscured and obscured sources as empty and filled data points, respectively, and does not allow a firm conclusion on this point for Seyfert-like luminosity sources.

4.6. Physically Motivated Models for the Obscured Sources

To constrain the spectral parameters, we also adopted two physically motivated, Monte Carlo models that self-consistently account for the toroidal geometry of the obscuring/reflecting medium and properly treat continuum suppression due to the additional contribution of Compton-scattering at the highest column densities. The latter contribution, if neglected, can lead to an overestimation of the column density of the obscuring medium. The models used are MYTorus (Murphy & Yaqoob 2009) and the Brightman & Nandra (2011) model (hereafter BNTorus). MYTorus assumes a proper torus geometry with a half-opening angle $\theta_{\rm oa} = 60°$ (i.e., a covering factor of 0.5). The torus geometry in BNTorus is approximated as a sphere with variable polar conical openings. We apply these models to the obscured sources (i.e., those found to have column density values or upper/lower limits consistent with $\log[N_{\rm H}/{\rm cm^{-2}}] \gtrsim 22$, including *ser409* for which $N_{\rm H}$ was unconstrained) as estimated by the baseline model (see Table 5) with the aim of comparing the $N_{\rm H}$ values. We assume an edge-on orientation with inclination angle 85°. For the low S/N spectra with unconstrained photon indices, we fix $\Gamma = 1.8$.

The best-fit parameters are reported in Table 7. For both models, there is broad agreement in $N_{\rm H}$ and Γ with the baseline model. Indeed, we have 15 and 16 sources, ∼25% of the sample, in the $\log(N_{\rm H}/{\rm cm^{-2}}) = 23$–24 bin for BNTorus and MYTorus, respectively.[38] For the two sources having best-fit $N_{\rm H}$ values in the CT regime from the baseline model, *cosmos330* and *ser261*, the latter has the lowest S/N *NuSTAR*-only

[38] Furthermore, both modelings have an additional source with estimated $N_{\rm H}$ consistent within 1σ with $\log(N_{\rm H}/{\rm cm^{-2}}) \geqslant 23$.

Table 7
Best-fit Parameters for the Torus Models

	BNTorus							MYTorus						
ID	stat	dof	Γ	$\log N_{\rm H}$[a]	S_{8-24}[b]	S_{3-24}[b]	$\log L_{\rm u,X}$[c]	stat	dof	Γ	$\log N_{\rm H}$[a]	S_{8-24}[b]	S_{3-24}[b]	$\log L_{\rm u,X}$[c]
cosmos97	271.1	264	$1.33^{+0.06}_{-0.07}$	$22.38^{+0.04}_{-0.03}$	3.8	5.4	43.2	291.0	265	1.80	$22.56^{+0.02}_{-0.02}$	2.8	4.6	43.0
cosmos107	19.6	17	$1.73^{+0.56}_{-0.56}$	$23.53^{+0.23}_{-0.28}$	0.9	1.2	44.4	19.5	17	$1.77^{+0.58}_{-1.77}$	$23.61^{+0.22}_{-0.29}$	0.9	1.3	44.5
cosmos129	18.5	25	1.80	$23.80^{+0.10}_{-0.09}$	0.5	0.7	44.6	18.5	25	1.80	$23.81^{+0.11}_{-0.07}$	0.5	0.7	44.6
cosmos145	151.2	171	$1.59^{+0.12}_{-0.08}$	$21.87^{+0.07}_{-0.07}$	0.6	0.9	43.7	152.0	171	$1.67^{+0.07}_{-0.05}$	<22.05	0.5	0.8	43.7
cosmos154	75.4	72	$1.73^{+0.26}_{-0.22}$	$23.49^{+0.09}_{-0.06}$	1.6	2.0	43.6	125.2	81	$1.68^{+0.25}_{-0.21}$	$23.50^{+0.08}_{-0.08}$	1.4	1.9	43.5
cosmos181	49.3	48	1.80	$23.89^{+0.10}_{-0.05}$	1.2	1.4	43.1	88.1	52	$2.27^{+0.16}_{-0.08}$	$23.78^{+0.04}_{-0.08}$	1.0	1.3	42.9
cosmos216	30.3	44	1.80	$23.67^{+0.06}_{-0.13}$	0.8	1.1	44.4	29.8	43	$2.07^{+-2.07}_{-0.45}$	$23.74^{+0.20}_{-0.17}$	0.6	0.9	44.4
cosmos217	321.7	268	$1.76^{+0.07}_{-0.05}$	$22.34^{+0.04}_{-0.06}$	0.5	0.8	45.0	321.6	268	$1.74^{+0.08}_{-0.06}$	$22.38^{+0.04}_{-0.06}$	0.5	0.8	45.0
cosmos232	64.6	77	$1.32^{+0.24}_{-0.18}$	$23.20^{+0.07}_{-0.09}$	0.8	1.0	44.6	69.2	78	1.80	$23.35^{+0.05}_{-0.04}$	0.5	0.8	44.5
cosmos249	23.1	29	$1.80^{+0.35}_{-0.46}$	$23.54^{+0.13}_{-0.17}$	1.1	1.4	43.4	23.7	29	$1.52^{+0.58}_{-1.52}$	$23.53^{+0.17}_{-0.13}$	1.3	1.6	43.5
cosmos253	61.2	53	1.80	$22.68^{+0.09}_{-0.06}$	0.8	1.3	43.2	61.9	53	1.80	$22.75^{+0.05}_{-0.09}$	0.9	1.4	43.2
cosmos272	85.7	70	$1.39^{+0.14}_{-0.14}$	$22.62^{+0.08}_{-0.14}$	1.0	1.5	44.4	88.2	71	1.80	$22.79^{+0.06}_{-0.05}$	0.8	1.3	44.3
cosmos297	277.3	249	$1.80^{+0.08}_{-0.08}$	$21.89^{+0.04}_{-0.05}$	1.0	1.7	43.8	295.8	249	$1.82^{+0.05}_{-0.05}$	<22.02	0.6	1.0	43.6
cosmos299	100.7	73	$1.80^{+0.07}_{-0.05}$	$23.51^{+0.07}_{-0.04}$	1.7	2.4	44.3	107.9	73	$1.81^{+0.56}_{-0.15}$	$23.53^{+0.11}_{-0.04}$	1.7	2.4	44.3
cosmos330	83.5	84	$1.86^{+0.16}_{-0.19}$	$24.07^{+0.08}_{-0.05}$	3.2	3.5	42.7	90.8	84	$1.46^{+0.08}_{-1.46}$	$23.99^{+0.05}_{-0.04}$	3.3	3.6	42.7
ecdfs20	706.1	718	$1.61^{+0.07}_{-0.07}$	$22.87^{+0.02}_{-0.04}$	1.0	1.6	44.8	706.8	718	$1.57^{+0.05}_{-0.06}$	$22.90^{+0.02}_{-0.02}$	1.1	1.6	44.8
egs9	443.1	461	$1.80^{+0.07}_{-0.03}$	$22.66^{+0.01}_{-0.01}$	1.3	2.2	44.1	444.5	461	$1.79^{+0.05}_{-0.05}$	$22.70^{+0.02}_{-0.02}$	1.3	2.2	44.1
ser97	94.2	96	$2.31^{+0.22}_{-0.24}$	$23.01^{+0.21}_{-0.25}$	1.7	3.1	43.4	94.2	96	$2.29^{+0.21}_{-0.24}$	$23.06^{+0.21}_{-0.27}$	1.7	3.1	43.4
ser107	27.6	40	$1.49^{+0.26}_{-0.28}$	$23.17^{+0.23}_{-0.17}$	1.4	1.9	43.4	27.7	41	1.80	$23.38^{+0.07}_{-0.09}$	1.3	1.7	43.4
ser153	99.5	95	$1.87^{+0.24}_{-0.19}$	$23.30^{+0.24}_{-0.25}$	1.1	1.8	45.2	99.9	95	$1.86^{+0.24}_{-0.20}$	$23.34^{+0.25}_{-0.24}$	1.1	1.8	45.2
ser213	187.4	184	$1.43^{+0.13}_{-0.13}$	$23.08^{+0.09}_{-0.15}$	5.5	7.5	44.4	187.4	184	1.80	$23.09^{+0.05}_{-0.09}$	5.6	7.6	44.4
ser235	64.9	57	$1.79^{+0.35}_{-0.31}$	<23.87	1.2	2.0	45.6	64.8	57	$1.80^{+0.31}_{-0.33}$	<24.13	1.1	2.0	45.6
ser243	153.2	147	$1.38^{+0.11}_{-0.09}$	$22.97^{+0.05}_{-0.05}$	3.3	4.6	44.4	158.8	148	1.80	$23.14^{+0.04}_{-0.04}$	3.4	4.7	44.5
ser254	260.0	260	$2.17^{+0.16}_{-0.53}$	$22.93^{+0.05}_{-0.09}$	3.8	6.0	43.7	260.1	260	$2.05^{+0.33}_{-0.32}$	$22.95^{+0.09}_{-0.11}$	3.6	5.8	43.7
ser261	15.7	16	1.80	>23.84	1.1	1.2	45.0	16.2	16	1.80	>23.71	0.9	1.0	44.9
ser285	8.3	9	$1.57^{+0.07}_{-0.33}$	<23.99	1.0	1.5	44.5	8.3	9	$1.59^{+0.71}_{-1.59}$	<23.80	1.0	1.5	44.5
ser359	23.7	45	$1.52^{+0.27}_{-0.22}$	$22.52^{+0.17}_{-0.15}$	2.3	3.3	43.9	23.7	45	$1.51^{+0.28}_{-1.51}$	$22.58^{+0.14}_{-0.16}$	2.3	3.4	43.9
ser382	41.3	43	$1.75^{+0.20}_{-0.12}$	$22.10^{+0.14}_{-0.07}$	0.8	1.4	43.3	41.5	43	$1.70^{+0.19}_{-0.13}$	$22.13^{+0.14}_{-0.07}$	0.8	1.3	43.3
ser401	31.8	33	$1.76^{+0.19}_{-0.18}$	$21.91^{+0.17}_{-0.22}$	0.9	1.4	44.5	31.9	33	$1.80^{+0.15}_{-0.13}$	<22.21	0.8	1.4	44.4
ser409	35.7	32	1.80	<24.08	0.7	1.2	44.9	8.2	5	1.80	<23.72	0.9	1.3	44.9
ser451	52.0	68	$1.82^{+0.36}_{-0.10}$	$23.35^{+0.29}_{-0.09}$	1.4	2.1	44.5	52.0	68	$1.92^{+0.41}_{-0.14}$	$23.40^{+0.28}_{-0.10}$	1.3	2.0	44.5

Notes.
[a] Line-of-sight column density in units of $\rm cm^{-2}$.
[b] Units of 10^{-13} erg $\rm s^{-1}$ $\rm cm^{-2}$.
[c] Unabsorbed 10–40 keV luminosity in units of erg $\rm s^{-1}$.

spectrum in the sample, and it is not confirmed to be CT. Indeed the estimated lower limits on $N_{\rm H}$ for both torus models are in the heavily obscured range $\log(N_{\rm H}/{\rm cm}^{-2}) = 23$–$24$. Therefore, the source could still be CT. The other two sources with upper limits in the CT regime from the baseline model, *ser285* and *ser235*, typically have upper limits in the heavily obscured range for both models, the exception being *ser235,* for which MYTorus gives an upper limit in the CT range. Figure 9 shows a comparison between column densities derived from both models. There is good agreement for the BNTorus model (empty circles), although with a tendency to estimate systematically slightly lower $N_{\rm H}$ values.[39] Red dots report the best-fit $N_{\rm H}$ values from MYTorus, which also show good agreement. Given the mild disagreement regarding $N_{\rm H}$ for the two CT sources, as estimated by the baseline model, we further modify the primary power law in the baseline model with an approximated Compton-scattering term parameterized in XSPEC with the CABS model. Both sources are still reported to be CT. This highlights the need to account for accurate Compton scattering treatment and geometry-dependent effects, as provided by the torus modelings, in order to get an accurate estimate of the column density for the most obscured AGN.

5. Observed $N_{\rm H}$ Distribution

The distribution of $N_{\rm H}$ derived from photoelectric absorption, as evaluated by the baseline model (Section 4.2) for 62 out of 63 sources, is shown in the histograms reported in Figure 10 (upper panel). The empty histogram reports sources for which $N_{\rm H}$ is at least constrained at the 1σ level, with error bars computed following Poisson counting statistics (Gehrels 1986). The filled green histogram reports sources with 90% upper limits on $N_{\rm H}$. For the latter, two sources have very high (i.e., poorly constrained) column density upper limits in the range $\log(N_{\rm H}/{\rm cm}^{-2}) = 23$–$25$ (one in the CT range). These are sources with *NuSTAR*-only X-ray data available, for which the missing coverage at lower X-ray energies limits our ability to

[39] This could be due to the tendency of BNTorus to overestimate the low-energy reflection component for edge-on orientations, as pointed out by Liu & Li (2015). This would require a lower column density to explain the observed absorption cut-off.

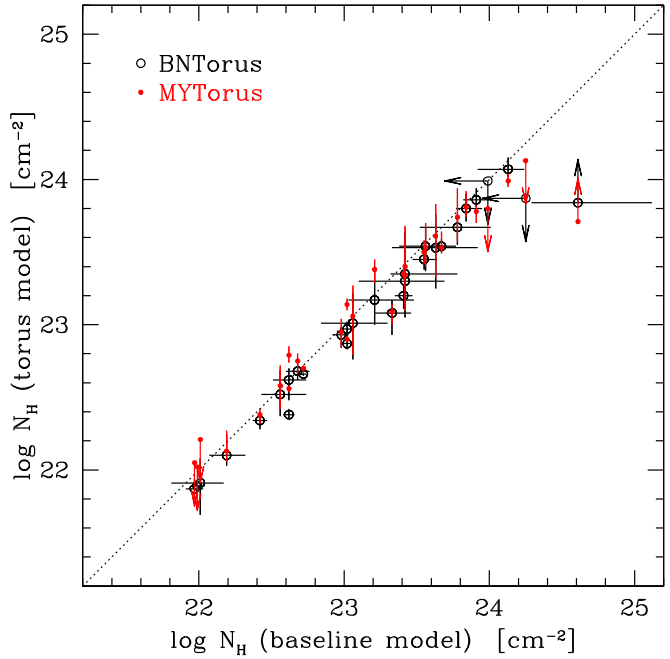

Figure 9. Comparison of column density values from the best-fit baseline model and torus models for the obscured sources. Black hollow circles report values from the BNTORUS model. Red dots report values from the MYTORUS model.

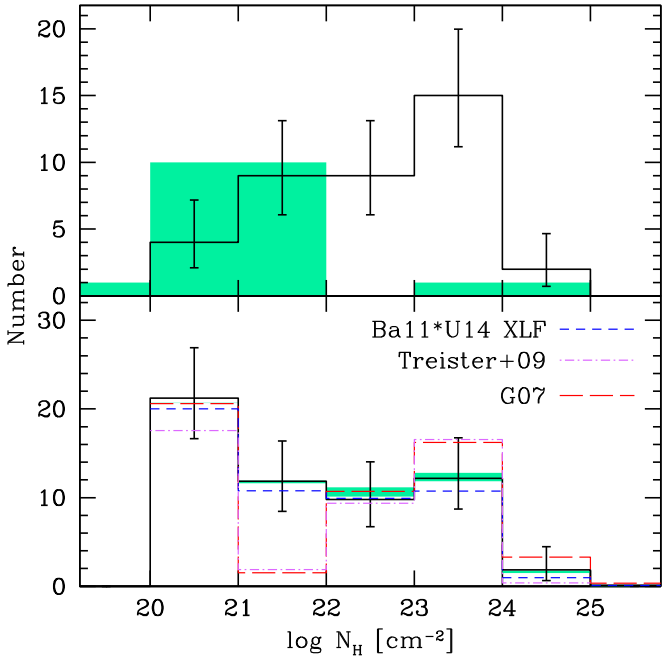

Figure 10. Upper panel: column density distribution from the baseline spectral model (black histogram), with error bars calculated assuming low counting statistics. Shaded green histogram reports 90% upper limits for data sets with limited constraining power (i.e., high-redshift, low $N_{\rm H}$, or sources with only *NuSTAR* spectra). Lower panel: black line shows the distribution in which the $N_{\rm H}$ best-fit values and upper limits from the baseline model have been randomized as described in Section 5. Green indicates the range of $N_{\rm H}$ distribution by substituting the baseline-derived measurements for the sources with $\log(N_{\rm H}/{\rm cm}^{-2}) \geqslant 23$ with those derived by adopting the torus models. Red (long dashed), blue (dashed), and magenta (dot dashed) histograms are model predictions from G07 and BA11 using the U14 XLF and Treister et al. (2009).

measure lower column densities. We find two sources (*cosmos330* and *ser261*) in the CT range. However, the torus modeling finds a lower number of CT AGN. Only *cosmos330* is formally considered as such by BNTORUS. MYTORUS finds it to be slightly below the the CT range. For *ser261*, both models place a lower limit in the heavily obscured regime ($\log[N_{\rm H}/{\rm cm}^{-2}] = 23$–$24$) for the low-quality spectrum of *ser261* (see Figure 9). Both models place an upper limit in the CT regime for only one source: *ser409* for BNTORUS (this source has $N_{\rm H}$ unconstrained by the baseline modeling) and *ser235* for MYTORUS.

We build a histogram of the column-density distribution of the sample by folding in the error information in $N_{\rm H}$ best-fit values and the 90% upper limits. In order to do this, analogous to Section 4.5, we performed 1000 random realizations of the sample. We assume symmetric Gaussian distributions in $\log N_{\rm H}$ with 1σ standard deviations as the mean of the lower and upper errors. For sources with upper limits in $\log N_{\rm H}$, we assume a smooth uniform random distribution down to $\log(N_{\rm H}/{\rm cm}^{-2}) = 20\ {\rm cm}^{-2}$. We then averaged the resulting $N_{\rm H}$ distributions and obtained the randomized histogram reported in black in Figure 10 (lower panel). Notice that this procedure, because of the upper limits, may lead to an overestimate of the $\log(N_{\rm H}/{\rm cm}^{-2}) = 20$–$21$ numbers due to the contributions from the sources with upper limits in the $\log(N_{\rm H}/{\rm cm}^{-2}) = 21$–$22$ bin (some may really belong to this bin but are averaged over all the $\log[N_{\rm H}/{\rm cm}^{-2}] = 20$–$22$ range). We also accounted for the $N_{\rm H}$ values obtained by the torus modeling. We substituted them for the sources with baseline-derived $N_{\rm H}$ measurements in excess of $10^{23}\ {\rm cm}^{-2}$. Figure 10 shows the torus-derived $N_{\rm H}$ distribution (and its range) in green. There is very little difference vis a vis those derived with the baseline values.

We compared the randomized $N_{\rm H}$ distributions with the prediction from theoretical models (dashed histograms in figure) by G07 (red long-dashed), Treister et al. (2009) (magenta dot-dashed) and BA11 (blue short-dashed), updated with the X-ray Luminosity Function (XLF) of Ueda et al. 2014 (hereafter BA11+U14) folded with the sky coverage of our survey (Figure 1) at fluxes above the threshold set for selecting the sample ($S_{8-24} \geqslant 7 \times 10^{-14}\ {\rm erg\ s^{-1}\ cm^{-2}}$). All models predict a slightly lower total number of sources than the randomized histogram does. However, they are all roughly consistent within the Poissonian errors. Specifically, we have a total of 57 sources above threshold, while G07, Treister et al. (2009), and BA11+U14 predict 52.7, 46, and 52.5, respectively. There is fair agreement within the uncertainties between the models and our randomized histogram for the obscured sources. As for the unobscured sources ($\log[N_{\rm H}/{\rm cm}^{-2}] \leqslant 22$), the anomalous low value of the G07 model at $\log(N_{\rm H}/{\rm cm}^{-2}) =$ 21–22, as reported by Gilli et al. (2007) themselves, seems to be due to the assumed XLF for type-1 AGNs (from Hasinger et al. 2005), which probably is contaminated at the level of 10–20% by mildly obscured ($\log[N_{\rm H}/{\rm cm}^{-2}] = 21$–$22$) sources, making the transition to the $\log(N_{\rm H}/{\rm cm}^{-2}) \geqslant 22$ sources unrealistically steep. Correcting for a 10–20% contamination alleviates the disagreement with our data at 1.5–2.1σ level. Furthermore, Treister et al. (2009) predicts a very small number of sources at $\log(N_{\rm H}/{\rm cm}^{-2}) = 21$–$22$. This is probably due to the fact that, in this regime, the host galaxy obscuration plays a non-negligible role. This further extranuclear absorption component is not accounted for in the model.

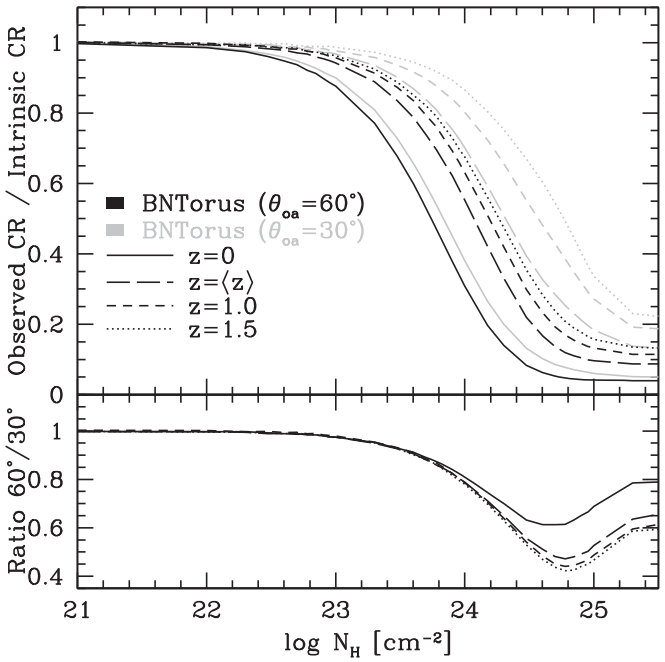

Figure 11. Upper panel: absorption bias in the 8–24 keV band, assuming a BNTorus model with $\Gamma = 1.8$ for different redshifts as indicated. Black and light gray respectively indicate $\theta_{oa} = 60°$ and 30° (BNTorus30 case). Lower panel: ratio between the 8–24 keV absorption bias between 60° and 30°.

6. Intrinsic N_H Distribution and Fraction of CT AGN

Both models in Figure 10 agree with our data and predict a very low number (∼1–4) of CT AGNs in our selected hard sample. This is a consequence of the fact that the 8–24 keV *NuSTAR* band is still biased against extremely obscured sources. This bias depends primarily on the redshift of the sources, on the width and high-energy bound of the range used for selecting the sources, and on the value of the instrumental effective area at the energies where CT sources mostly emit. Figure 11 highlights this for a BNTorus model[40] with $\Gamma = 1.8$ by showing the "absorption bias" $B(\log N_H, z)$, i.e., the ratio between observed and intrinsic 8–24 keV *NuSTAR* count-rates as a function of the absorbing column density. The different black curves show this bias for the 8–24 keV band at redshifts 0, 0.58 (the median redshift of our sample), 1.0, 1.5 (respectively solid, long-dashed, short-dashed, and dotted lines) for a torus with $\theta_{oa} = 60°$. The bias for a fixed N_H decreases with redshift. In gray, we show the bias for $\theta_{oa} = 30°$ (hereafter BNTorus30). In the lower panel, we report the ratio between the bias among the two opening angles. A smaller opening angle of the torus tends to give less bias. Given the fact that *NuSTAR* probes non-local sources up to $z \approx 2$–3, we infer that *NuSTAR* has, on average, roughly the same absorption bias as *Swift*-BAT at these flux levels.

For the unobscured sources, the hard *NuSTAR* band is not biased at any redshift. The following considerations take the absorption bias as a reference, with $\theta_{oa} = 60°$. This will weight the heavily absorbed sources more when correcting for it. We later discuss possible changes in our estimates when using a bias given by the BNTorus30 case. At larger column densities, the bias is more evident for increasing N_H. It becomes more pronounced for the CT sources (from 0.4 to 0.7, depending on redshift to less than 0.2). This means that, while we detect all the unobscured sources at intrinsic fluxes down to $S_{8-24} \approx 7 \times 10^{-14}$ erg s^{-1} cm^{-2}, we are sensitive to sources with intrinsic fluxes in the range $\sim(1–3) \times 10^{-13}$ erg s^{-1} cm^{-2} for the CT sources; therefore, we are missing a sizable fraction of the CT AGN population at fainter intrinsic (i.e., unabsorbed) fluxes. We can recover the missing AGN population by computing the intrinsic N_H distribution down to a certain intrinsic (i.e., unabsorbed) flux level common to all the sources regardless of their column density. Following Burlon et al. (2011), we integrate the source counts dN/dS derived in each 1 dex $\log N_H$ bin (see Section 8) from a minimum (S_{min}^{obs}) to a maximum (S_{max}^{obs}) observed flux, as follows:

$$\frac{dN}{d\log N_H} = \int_{S_{min}^{obs} = S_{min}^{intr} \times B(\log N_H, z)}^{S_{max}} \frac{dN}{dS}(\log N_H) dS,$$

where $B(\log N_H, z)$ depends on N_H as well as the mean redshift of the sources in each $\log N_H$ bin, and S_{min}^{intr} is the minimum intrinsic (i.e., absorption-corrected) source flux at which the intrinsic distribution is estimated. In order to derive the source counts in each $\log N_H$ accounting for uncertainties in N_H, we applied, through 10,000 realizations of the sample, the same randomization procedure for error and upper/lower limits as explained for the observed N_H distribution Section 5. We model the derived $\log N$–$\log S$ in each realization as a power law with slope α and normalization K, and adopted the median values among all the realizations for each bin as representative. These best-fit values are reported in Table 8. The derived slopes are all consistent, within the uncertainties, with the 3/2 Euclidean value for a uniform, non-evolving universe. A small number of realizations (at the percent level) gave no sources in the CT bin; hence, in these cases, no source count could be computed. Given their paucity, we neglected these cases.[41] We derived the distributions for N_H estimated by (i) baseline-only modeling and (ii) baseline model for sources with $\log(N_H/\mathrm{cm}^{-2}) \leqslant 23$ and BNTorus model for more obscured sources. The latter case has been considered in order to include more accurate N_H estimates at the highest column densities (see Figure 9). The value of S_{min}^{intr} is chosen such that we are sensitive, according to $B(\log N_H, z)$, to the same intrinsic flux for all the sources, regardless of their N_H. This parameter is critical for deriving a CT fraction with reliable uncertainties. Indeed, in the CT bin, $B(\log N_H, z)$ may vary by a factor of 4–6 in accord with the exact value of N_H (see Figure 11). Given that we have only a couple of CT sources, one of which (*ser261*) has large errors—and in the torus models is not even considered a bona fide CT—the choice of S_{min}^{intr} is subject to large uncertainties. Therefore, to make that determination, we relied on the ∼10 sources within which the uncertainties have N_H compatible with $\log(N_H/\mathrm{cm}^{-2}) \approx 24$. We verified, through 1000 realizations of the sample, that accounting for the flux uncertainties and adopting an absorption bias relative to the redshift of each source and its randomized N_H (we are excluding objects with upper limits whose absorption

[40] The adoption of BNTorus (which is assumed representative for the toroidal models) instead of the baseline model is due to the fact that, at high N_H, it allows a more accurate estimate of the bias. At low N_H, they both predict very negligible bias.

[41] We verified that our adopted median values are stable and not very sensitive to these outliers.

Table 8
Best-fit Values of the Slope and Normalization of a Power-law Model to the Source Counts as a Function of Column Density

$\Delta \log N_{\rm H}$ ($\rm cm^{-2}$)	α	K [$\rm deg^{-2}$] at 10^{-13} erg $\rm s^{-1}$ $\rm cm^{-2}$
	Baseline	
20–21	2.02 ± 0.73	3.93 ± 0.85
20–22	2.22 ± 0.61	5.88 ± 1.00
21–22	2.63 ± 1.30	2.00 ± 0.56
22–23	1.33 ± 0.86	1.94 ± 0.59
23–24	1.50 ± 0.74	2.25 ± 0.60
24–25	2.62 ± 3.96	0.49 ± 0.36
	Baseline+BNTorus	
20–21	2.04 ± 0.74	3.91 ± 0.85
20–22	2.24 ± 0.62	5.83 ± 0.99
21–22	2.68 ± 1.30	1.99 ± 0.55
22–23	1.28 ± 0.77	2.31 ± 0.65
23–24	1.63 ± 0.83	2.18 ± 0.61
24–25	2.19 ± 4.33	0.62 ± 0.46

Note. Values are presented for baseline-only modeling and baseline + BNTorus (the latter used for only $\log(N_{\rm H}/\rm cm^{-2}) \geqslant 23$ sources).

bias—and therefore intrinsic flux—cannot be reliably estimated), a flux of $S_{\rm min}^{\rm intr} = 10^{-13}$ erg $\rm s^{-1}$ $\rm cm^{-2}$ is adequate for our purposes. In this way, we estimate the intrinsic $N_{\rm H}$ distribution of the population of AGNs down to this intrinsic flux. In the integration, we are assuming the value of the absorption bias relative to the central $\log N_{\rm H}$ value at the mean redshift of each bin to be representative for each bin. This sets a representative value of $S_{\rm min}^{\rm obs}$ to perform the integration of the source counts in each bin. This has non-negligible implications in the CT bin, where the absorption bias, being strongly dependent on $\log N_{\rm H}$, makes the estimation of $S_{\rm min}^{\rm obs}$ highly uncertain. Given the paucity of possible CT AGN in our CT bin, which may reflect the distribution of CT sources at "intrinsic" fluxes of 10^{-13} erg $\rm s^{-1}$ $\rm cm^{-2}$, and given that they have column densities close to $\log(N_{\rm H}/\rm cm^{-2}) = 24$, we have decided to use an absorption bias relative to $N_{\rm H} = 1.5 \times 10^{24} \rm cm^{-2}$ (i.e., the formal threshold for defining a source as CT) for the CT bin. The derived distribution is reported in the histograms of Figure 12, where the $N_{\rm H}$ estimates for the more obscured sources are from BNTorus. Notice that the reported distributions for baseline-only $N_{\rm H}$ estimates are very similar, providing only slightly higher estimates in the CT bin. The error-bars reflect the low counting statistics on the number of sources whose unabsorbed flux is above $S_{\rm min}^{\rm intr}$ in each bin. In the upper panel, we report the intrinsic distribution using normalizations derived from the source counts fits to all the sources in 1 dex $\log N_{\rm H}$ intervals (see Table 8) and assuming an Euclidean slope.[42] In the lower panel, we report the fractional number of AGN in each bin relative to the total number of sources at $\log(N_{\rm H}/\rm cm^{-2}) < 24$ (f^{20-24}) from the intrinsic distribution. The shaded gray region is the 1σ range obtained through error propagation from the intrinsic $N_{\rm H}$ distribution uncertainties. We

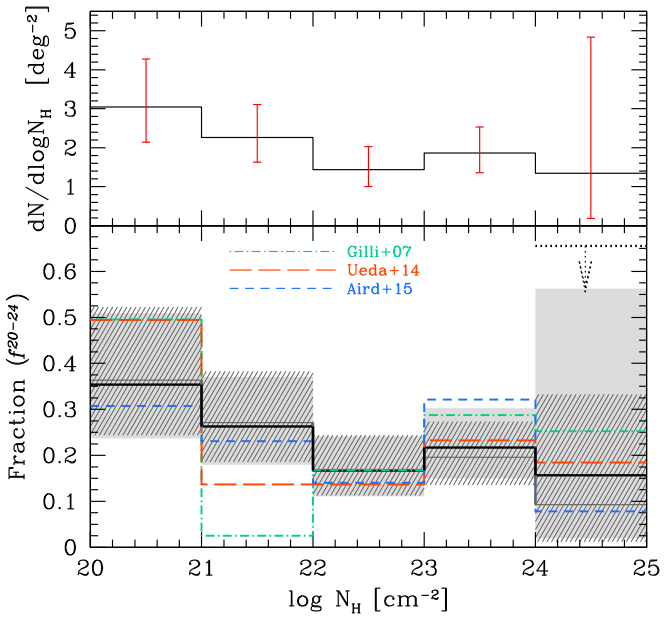

Figure 12. Intrinsic $N_{\rm H}$ distributions (upper panel) and fraction relative to the total number of objects in the intrinsic distribution (shaded gray, lower panel). The distributions presented here are for $N_{\rm H}$ derived by the baseline model, except for the heavily obscured sources (i.e., $\log[N_{\rm H}/\rm cm^{-2}] \geqslant 23$) for which the BNTorus model estimates are adopted. Error bars reflect the low counting statistics of the observed $N_{\rm H}$ distribution (Figure 10). The shaded gray and hatched dark gray regions represent the 1σ range of derived fractions assuming different absorption bias corrections with $\theta_{\rm oa}$ in the BNTorus model of 60° and 30°, respectively (see Figure 11). In the $\log(N_{\rm H}/\rm cm^{-2}) = 24$–25 bin, we also report the 90% upper limits as dotted lines. Model predictions from G07, U14, and Aird et al. (2015a) are shown in dotted–dashed green, long-dashed orange, and short-dashed blue, respectively.

also report, in hatched dark gray regions, the fractional distributions, assuming an absorption bias derived by BNTorus30 (see gray lines in Figure 11) and fixing[43] $S_{\rm min}^{\rm intr} = 10^{-13}$ erg $\rm s^{-1}$ $\rm cm^{-2}$. We obtain a fraction of CT sources $f_{\rm CT}^{20-24} = 0.02$–$0.56$ (0.01–0.33 for BNTorus30). The 90% upper-limit is $f_{\rm CT}^{20-24} < 0.66$, reported in the figure as a dotted line. Assuming an $N_{\rm H}$ derived from only the baseline model, we obtain $f_{\rm CT}^{20-24} = 0.08$–$0.66$.

7. Fraction of Absorbed Sources

Clear trends in the fraction of absorbed AGNs ($f_{\rm abs}$), compared to the whole population, have been found with redshift and luminosity. Indeed, several authors report a decrease in the absorbed AGN population with source luminosity (e.g., Lawrence & Elvis 1982; Steffen et al. 2003; La Franca et al. 2005; Sazonov et al. 2007; Della Ceca et al. 2008; Burlon et al. 2011) and an increase with redshift at fixed X-ray luminosity (e.g., La Franca et al. 2005; Ballantyne et al. 2006; Treister & Urry 2006; Ueda et al. 2014; Vito et al. 2014). Our spectral analysis effectively probes rest-frame ~1.2–24 keV for all the sources, given the redshift distribution from $z \gtrsim 0$ up to $z \approx 1.5$. It can therefore account globally for the most relevant spectral complexity measurable in X-ray

[42] The fraction of the CT sources (relative to all AGN population) obtained with the best-fit slopes is rather high and uncertain, given its large uncertainties; see Table 8.

[43] The absorption bias in this case is smaller by a factor of about two, compared to the adopted $\theta_{\rm oa} = 60°$ (see Figure 11 lower panel). However, given the uncertainties in estimating the exact value of $S_{\rm min}^{\rm intr}$ due to the low number of sources, we prefer to assume the same value derived for the 60° case.

AGN spectra, and allows an accurate determination of the absorbing column density. For this reason, we estimated the fraction of absorbed sources as a function of X-ray luminosity and redshift. Given that our survey is biased at the highest absorptions (i.e., at CT column densities), we chose to neglect these sources and estimate fraction of absorbed Compton-thin AGN.

Because of the selection of our sample, we must correct our observed number of absorbed sources for the fact that AGN with a given intrinsic luminosity are progressively missed in the surveyed field for increasing column densities at larger distances. This translates to larger cosmic volumes sampled for unobscured sources compared to obscured ones. To account for this selection effect, we computed the maximum surveyable comoving volume ($V_{\rm max}$, Schmidt 1968; Page & Carrera 2000) for each source, accounting for its observed (i.e., absorbed) luminosity ($L_x^{\rm obs}$) and survey sky-coverage $\Omega(S)$ using the following formula:

$$V_{\rm max} = \int_{z_{\rm min}=0}^{z_{\rm max}} \Omega(S(L_x^{\rm obs}, z)) \frac{dV}{dz} dz,$$

where $z_{\rm max}$ is chosen such that $S(L_x^{\rm obs}, z_{\rm max}) = 7 \times 10^{-14}$ erg s^{-1} cm^{-2} in the 8–24 keV band. The intrinsic fraction of obscured sources is therefore estimated as the ratio of the summed space densities of absorbed sources over the space densities of the total population:

$$f_{N_{\rm H}} = \frac{\sum_{i=1}^{N_{N_{\rm H}}} (V_{\rm max}^i)^{-1}}{\sum_{i=1}^{N_{\rm tot}} (V_{\rm max}^i)^{-1}},$$

where $N_{\rm tot}$ and $N_{N_{\rm H}}$ are, respectively, the total number of sources and the number of sources characterized by a column density larger than a given $N_{\rm H}$ value. Notice that, in our calculation, we use parameters derived from the baseline modeling, except for the heavily absorbed sources ($\log[N_{\rm H}/{\rm cm}^{-2}] \geqslant 23$) for which more accurate results from BNTorus have been incorporated. The uncertainty on $F_{N_{\rm H}}$ is obtained by error propagation of the uncertainties on $(V_{\rm max})^{-1}$. The latter is usually estimated as $\sqrt{\sum_i (V_{\rm max}^i)^{-2}}$ (Marshall 1985) by assuming Gaussian statistics in each bin. Because we are dealing with a relatively small number of sources per bin, this uncertainty estimate is not optimal in our case. We therefore estimate uncertainties through bootstrap resampling[44] in each luminosity bin. Notice that, in this case, we are not correcting for the absorption bias because $\log(N_{\rm H}/{\rm cm}^{-2}) = 23$–24 sources show little bias (see Figure 11) and the small number of AGN in each bin is the dominant source of uncertainty.

7.1. Fraction as a Function of Luminosity

Figure 13 shows the fraction of absorbed sources with $\log(N_{\rm H}/{\rm cm}^{-2}) \geqslant 22$ (f_{22}) as a function of the unabsorbed 10–40 keV luminosity. We adopt those values estimated from the bootstrap resampling procedure as being fiducial. We use the unabsorbed luminosity instead of the intrinsic coronal one in order to be consistent in comparing our results with those

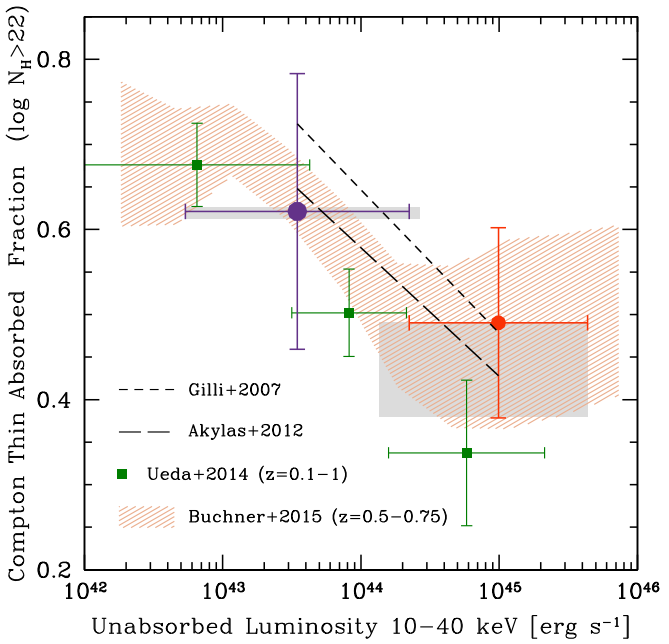

Figure 13. Intrinsic absorbed fractions for Compton-thin sources with $\log(N_{\rm H}/{\rm cm}^{-2}) > 22$ as a function of unabsorbed 10–40 keV luminosity. The relative median redshift from the objects contributing to each bin is highlighted with a bluer, larger dot representing local, lower luminosity sources, and redder, smaller ones showing objects at greater distances and luminosities. Green data are fractions reported by Ueda et al. (2014) for $z = 0.1$–1 sources. Hatched orange indicates the region determined by Buchner et al. (2015) for $z = 0.5$–0.75 AGN. Short- and long-dashed lines represent the G07 and Akylas et al. (2012) CXB synthesis model predictions, as indicated. Gray shaded regions relative to our two data points give an indication of the robustness of the absorbed fraction (see Section 7.1 for details).

derived by previous works. Furthermore, there is no comparable intrinsic luminosity quantity for the BNTorus-modeled heavily absorbed sources. In order to ensure good statistics and minimize the effects from single sources (i.e., outliers) we divide the sample into two bins, each containing a comparable number of objects. The size and color of each point gives an indication of the relative median redshift of the sources contributing to each bin, with the redder, smaller point sampling, on average, more distant sources.

We see a hint of a decreasing trend of f_{22} with luminosity. This dependence is, however, not very significant, being consistent within the uncertainties with no dependence with luminosity. Given the large range in redshift covered by our sample, it is possible that the redshift evolution in the fractions acts at the highest luminosities (where we have the more luminous sources) partially masking the luminosity dependence. The small number of sources prevents us from drawing firm conclusions on this point. In any case, our estimated values are perfectly consistent with population-synthesis model predictions not incorporating redshift evolution (G07 and Akylas et al. 2012). Given that 80% of the sources are at $z \lesssim 1$ and that 90% of the contribution to the high-luminosity bin comes from sources at $z \approx 0.3$–1.1, we can compare our results with recent determinations at similar redshifts. We find broad consistency with the estimated fractions for Compton-thin sources reported by Ueda et al. (2014) and Buchner et al. (2015) for $z = 0.1$–1 and $z = 0.5$–0.75, respectively.

To give an idea of the variance of our results on the adopted binning, we adjusted the bin width in order to include up to eight more sources (thus increasing the number of sources by

[44] For each bin, we performed 10,000 random resamplings to derive the absorbed fractions and their standard deviation.

~25%) and reported the range of the corresponding variations as gray regions. We find very stable results on the fraction for low-luminosity sources and a much broader range for high-luminosity sources. Notice, however, that our nominal high-luminosity fractions are at the upper end of this range. This is an indication that the fractions at higher luminosities may be somewhat smaller than estimated.

Our absorption fraction calculation has been obtained through the estimation of the space densities in the two bins. For the low-luminosity bin including sources in the redshift range[45] $z \approx 0.1$–0.25, we obtain total and absorbed space densities of $(4.7 \pm 1.5) \times 10^{-5}\,\mathrm{Mpc}^{-1}$ and $(2.9 \pm 1.3) \times 10^{-5}\,\mathrm{Mpc}^{-1}$. For the high-luminosity bin, including sources at $z \approx 0.3$–1 we obtain $(1.8 \pm 0.2) \times 10^{-6}\,\mathrm{Mpc}^{-1}$ and $(8.6 \pm 2.5) \times 10^{-7}\,\mathrm{Mpc}^{-1}$ for total and absorbed sources. It is difficult to compare these values to other results, given the small number of sources we have and that our choice of luminosity intervals is driven by the need to maximize the statistics in each bin, which also makes the redshift intervals equally poorly defined and luminosity-dependent. In any case, the total values are in fair agreement with the models from U14 and Aird et al. (2015b).

7.2. Fraction as a Function of Redshift

Recently, Liu et al. (2017) performed a spectral analysis of the brightest AGN in the 7 Ms CDF-S and investigated f_{22} as a function of redshift. They divided their sample in redshift bins in the range $z = 0.8$–3.5 at fixed 2–10 keV luminosities $\log(L_{2-10}\,/\,\mathrm{erg\ s^{-1}}) = 43.5$–$44.2$. They evaluated that these objects are not biased by absorption up to $\log(N_{\rm H}/\mathrm{cm^{-2}}) = 24$. In order to compare with their estimates, we measured the absorption fraction in the same luminosity range for sources in the redshift interval $z = 0.1$–0.5. According to their criterion, this subsample is not biased for $\log(N_{\rm H}/\mathrm{cm^{-2}}) < 24$.[46] We obtain an absorption fraction of $f_{22} = 0.30 \pm 0.17$. In Figure 14, we compare our value with those measured by Liu et al. (2017) for the subsample of sources with spectroscopic redshift determinations. We also report the best fit relative to their whole sample. Our low value nicely follows the monotonic trend with redshift reported by Liu et al. (2017) at higher redshifts. Notice that they had only 12 sources in each bin. In any case, their estimates broadly agree with those inferred by the entire sample (including sources with photometric redshifts), for which they have bins populated by 17–26 sources. Given that our subsample consists of only 11 sources, we decided to explore the robustness of our measure by including neighboring sources (enlarging the subsample to up to 16 sources) by modifying the luminosity and redshift boundaries by ± 0.15 dex and ± 0.05, respectively. The range of possible variation of f_{22} is reported in Figure 14 as the shaded gray area. We also report relatively local (i.e., $z < 1$) fractions by U14 and Buchner et al. (2015). Their fractions measured at, on average, higher redshift ranges, lie at slightly higher f_{22} than our point.

[45] We calculate this range as the interval in redshift for the sources contributing at 90% of the total space densities.

[46] They evaluated their completeness down to a certain column density by assuming a power-law with $\Gamma = 1.8$ modified by photoelectric absorption with an empirically self-absorbed $(\log(N_{\rm H}/\mathrm{cm^{-2}}) = 23)$ reflection component parameterized by PEXRAV with $R = 0.5$ and $E_c = 300$ keV and a scattered fraction set to 1.7% of the primary continuum level.

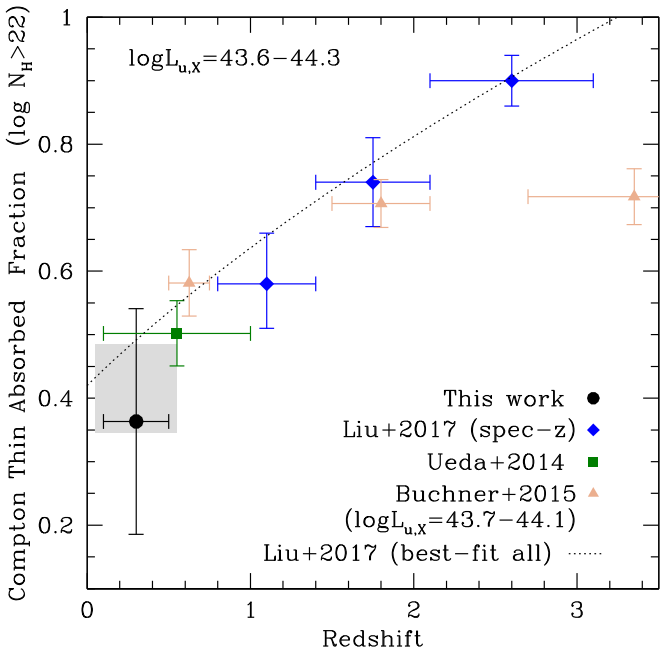

Figure 14. Compton-thin absorbed fractions as a function of redshift for $\log(L_{\rm u,X}/\mathrm{erg\ s^{-1}}) \approx 43.6$–$44.3$ (corresponding to the 2–10 keV $\log(L_{2-10}\,/\,\mathrm{erg\ s^{-1}}) \approx 43.5$–$44.2$, assuming an unabsorbed power law with $\Gamma = 1.8$ for the conversion). Black indicates the absorbed fraction estimated from our sample. Blue, green, and orange are absorbed fractions obtained by the spectroscopic sample in Liu et al. (2017), U14, and Buchner et al. (2015), respectively (the latter reported at $\log(L_{\rm u,X}/\mathrm{erg\ s^{-1}}) \approx 43.744.1$). The gray shaded region is relative to our data point and gives an indication of the robustness of the estimated absorbed fraction (see Section 7.2 for details). Dotted line is the best-fit model reported by Liu et al. (2017), also including sources with photometric redshift estimates in the absorbed fractions.

8. Source Counts as a Function of $N_{\rm H}$

Given that population-synthesis models reproduce the CXB as a mixture of AGN with different column densities, we can analyze the source counts as a function of $N_{\rm H}$ and compare them with model predictions. The latter starts to noticeably differentiate at higher column densities, with the largest difference in the CT regime.

Using the 8–24 keV sensitivity curves reported in Figure 1, we first produced the total source counts[47] for our sample. We model them as a simple power-law $K\,S^{-\alpha}$, given that our sources, having the highest hard-band fluxes in the *NuSTAR*-Extragalactic Survey program (H16), still probe fluxes well above the break at $\log(\mathrm{S_{8-24}/erg\ s^{-1}\ cm^{-2}}) \simeq -14$ predicted by background synthesis models (e.g., G07, BA11). We employed a maximum likelihood estimator (Crawford et al. 1970) to obtain, through a fit to the unbinned differential counts, the best-fit value of the slope α of the integral counts. The normalization of the power-law is fixed by the total number of estimated sources that should be matched by the best-fit model at the catalog lowest flux. The best-fit power-law has a slope value of $\alpha = 1.36 \pm 0.28$, which is flatter than—but still consistent with—the Euclidean 3/2 value for the integral distribution and a normalization of $10.1 \pm 1.3\ \mathrm{deg^{-2}}$ at $10^{-13}\ \mathrm{erg\ s^{-1}\ cm^{-2}}$ (where the error is Poissonian from the total number of sources employed in the source counts).

[47] We used Equations (5) and (6) in Cappelluti et al. (2007) to estimate cumulative number counts and relative uncertainties.

We analyzed the variation of the $\log N$–$\log S$ slope as a function of column density. In order to do this, we performed a scan in $N_{\rm H}$ with step 0.1 dex in $\log N_{\rm H}$. For each value of the column density, we estimate the value of the $\log N$–$\log S$ slope within an interval of ± 0.5 dex. We performed the usual 1000 realizations of our sample, randomizing $N_{\rm H}$ according to their errors and upper limit values. From each of these realizations, we produce a $\log N$–$\log S$ and obtain a best-fit value of α in each $\log N_{\rm H}$ bin. We construct a distribution of α and its uncertainty and assign their median values to the bin. In Figure 15 (upper panel), we report α as a function of $N_{\rm H}$. The average number of objects included in each $\log N$–$\log S$ interval, which is always greater than 10 for $\log(N_{\rm H}/{\rm cm}^{-2}) \lesssim 24$, is plotted in the lower panel (along with its 1σ dispersion). Although the values calculated in adjacent steps are correlated, this plot illustrates the robustness of the best-fit α value and its dependence on outlier objects. On scales larger than $\sim$1 dex in $\log N_{\rm H}$, we have an indication of uncorrelated variations of the slope as a function of $N_{\rm H}$. Throughout the range, there is always consistency within the large errors with an Euclidean slope value. Table 8 reports values for α and normalization of the best-fit power law in several $\log N_{\rm H}$ intervals from $\log(N_{\rm H}/{\rm cm}^{-2}) = 20$ to $\log(N_{\rm H}/{\rm cm}^{-2}) = 25$. Notice that fitting in separate column density bins and randomizing $\log N_{\rm H}$ within the uncertainties results in the sum of the normalizations from all the bins, 10.6 ± 1.4 deg^{-2}, which is slightly higher than the normalization obtained from the fit to the whole data set, but is consistent within the uncertainties.

We notice that, with the exception of the CT sources, unobscured AGN have, on average, higher best-fit slope values ($\alpha \approx 2$–2.4) than obscured objects ($\alpha \approx 1.3$–1.5). In the middle panel of Figure 15, we report the distribution of the median redshift values along with their interquartile range. Both α and the median redshift appear to be correlated, showing similar variations as a function of $N_{\rm H}$. Indeed, they have a Spearman correlation coefficient of $\sim$0.9. As expected, the median redshift of unobscured sources is larger than the sample median, meaning they comprise a large fraction of high-redshift sources. We investigated this trend by progressively removing high-redshift sources. To preserve a sufficiently high number of sources ($>$10) for each $N_{\rm H}$ interval, we only investigated unobscured ($\log[N_{\rm H}/{\rm cm}^{-2}] = 20$–22) and obscured ($\log[N_{\rm H}/{\rm cm}^{-2}] = 22$–24) bins. For the unobscured sources, we find that α progressively decreases to values around $\sim$1.4 when we only consider sources at $z \lesssim 0.4$. For the obscured sources, we notice variation around the Euclidean value across the redshift range within $\sim\pm 0.5$, by $z = 0.4$. Despite models that predict the fact that, at the fluxes probed by *NuSTAR*, $\log N$–$\log S$ will progressively flatten by going down to lower redshifts, this effect should be mild and not as strong as we are finding for the unobscured sources. Indeed, the G07 model predicts, in the flux range $S_{8-24} = 5 \times 10^{-14} - 10^{-12}$ erg s^{-1} cm^{-2}, the slope of the source counts flattens from $z = 1.1$ to $z = 0.4$, with values going from 1.6 to 1.2.

Figure 16 reports $\log N$–$\log S$ for unobscured ($\log[N_{\rm H}/{\rm cm}^{-2}] < 22$), mildly obscured ($\log[N_{\rm H}/{\rm cm}^{-2}] = 22$–23), heavily obscured ($\log[N_{\rm H}/{\rm cm}^{-2}] = 23$–24), and CT sources ($\log[N_{\rm H}/{\rm cm}^{-2}] > 24$). The best-fit power-law models (accounting for $N_{\rm H}$ uncertainties) for each are reported (see also Table 8) as solid lines. The dotted line represents the Euclidean power-law normalized so that it correctly predicts the total number of objects. Red long-dashed, blue short-dashed, and magenta dot-dashed lines show the predictions from G07, BA11 with U14 XLF and Treister et al. (2009) models, respectively. The discriminating power is stronger for the CT regime. However, in this range, we have only three objects, one of which has an upper limit and a minor contribution (during our randomization process) from less-obscured objects with estimated $N_{\rm H}$ close to the $\log(N_{\rm H}/{\rm cm}^{-2}) = 24$. The uncertainties are very large (see Table 8). The model's predictions are all roughly consistent with the source counts within the uncertainties, hence we cannot discriminate between models and draw firm conclusions.

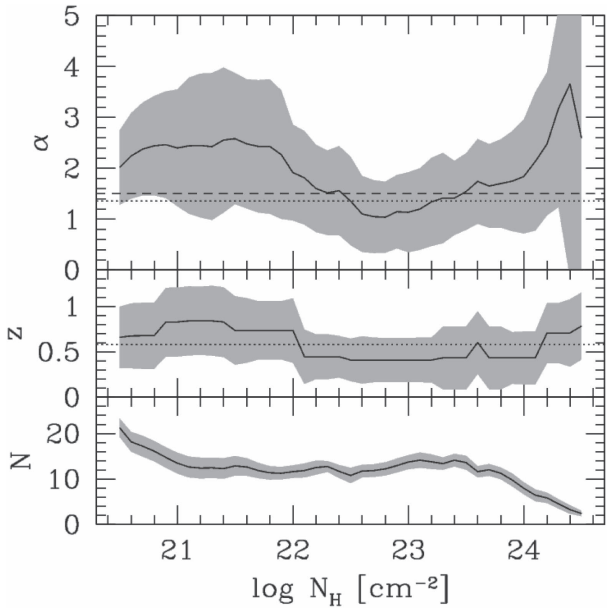

Figure 15. Upper panel: best-fit power-law slopes to the log N–log S produced in 0.1 dex $\log N_{\rm H}$ steps within 1 dex $\log N_{\rm H}$ bins. The slope and the relative uncertainty (shaded gray region) are the median value of the distribution of the best-fit α from 1000 realizations of the sample obtained by randomizing $\log N_{\rm H}$ according to their errors and upper limits. Dotted and dashed lines are the best-fit value for the log N–log S of the whole sample and the Euclidean value, respectively. Middle panel: the median redshift and relative interquartile range (shaded gray region) values obtained from the 1000 random realizations of the sample. Dotted line represents the median redshift value. Lower panel: mean value of the number of the sources considered with relative dispersion (shaded gray region) obtained from the random realizations.

9. Discussion

9.1. Sifting through Candidate CT Sources

Figure 10 displays, regardless of the spectral modeling adopted, a high fraction ($\sim$25%) of heavily absorbed ($\log[N_{\rm H}/{\rm cm}^{-2}] \geqslant 23$). Among these sources, we report one from the *NuSTAR*-COSMOS field (*cosmos330*) that is a bona fide CT, and one (*ser261*) from the serendipitous fields that has an estimate compatible with being CT (i.e., either CT in the baseline model or 90% lower limit in the range $\log[N_{\rm H}/{\rm cm}^{-2}] \approx 23.7$–23.8 from the toroidal modelings). Accounting for the uncertainties, we have an equivalent number of 1.5–2 CT, which, within the Poissonian uncertainties, is fully consistent with the $\sim$0.4–3.3 CT sources ($\log[N_{\rm H}/{\rm cm}^{-2}] = 24$–25) predicted to be observed in our survey by CXB population-synthesis models (Figure 10, bottom panel).

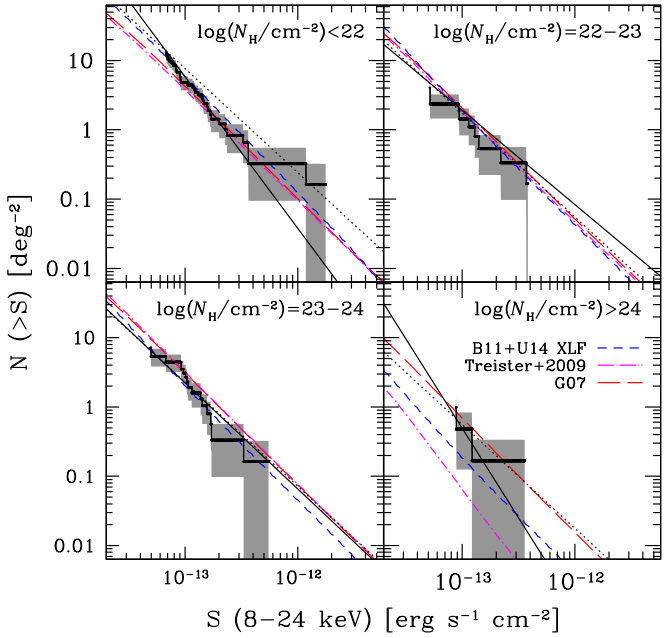

Figure 16. Unbinned source counts for the baseline model case for different $\log N_{\rm H}$ bins. For display purposes, we show the counts obtained by including the sources with column density upper limits in the bin relative to their upper limit value. Solid lines show the best-fit power-law models reported in Table 8 and obtained by accounting for the column density uncertainties as described in Section 8. Dotted line is the Euclidean power-law model whose normalization at the lowest flux equals that estimated for the best-fit model. Red long-dashed, blue short-dashed, and magenta dot-dashed lines are predictions from the G07, BA11, and Treister et al. (2009) models, respectively.

9.1.1. Claimed CT Candidates in the COSMOS Field and their Impact on the Observed CT Budget

Nonetheless, in our sample, we have sources from the COSMOS field, classified as heavily absorbed, which are in common with works focusing on *Chandra* (Brightman et al. 2014) and *XMM-Newton* (Lanzuisi et al. 2015) spectral analysis, and were claimed to be CT: *cosmos181* and *cosmos216*. The spectra and the best-fit models for these sources are reported in Figure 4. This disagreement is not unusual, several works using low-energy data have thus far attempted the spectral identification of distant CT sources in the medium/deep survey fields (e.g., Tozzi et al. 2006; Georgantopoulos et al. 2007, 2009, 2013; Comastri et al. 2011; Feruglio et al. 2011; Brightman & Ueda 2012; Brightman et al. 2014; Buchner et al. 2014; Lanzuisi et al. 2015), and given the range of possible spectral shapes for CT sources and the limited counting statistics (from few tens to ∼100 counts) for these faint sources, especially at the highest energies $\gtrsim$5–6 keV where the effective area starts to drop, researchers have always struggled to consistently identify CT sources (see, e.g., Castelló-Mor et al. 2013). Moreover, their analysis, at least for sources with redshifts $\ll$2 (i.e., the great majority of the potential contributors to the CXB, according to population-synthesis models), have been limited by sampling of the restricted lower-energy part of the reflection component and of the heavily obscured primary emission. This may potentially add possibly non-negligible systematic uncertainties to the statistical ones. Interestingly, Marchesi et al. (2018) analyzing 30 local candidate CT AGN selected from the *Swift/BAT* 100 month survey, found that the addition of *NuSTAR* data allowed a re-classification of ∼40% of the sources as Compton-thin. Source variability may furthermore play a role, because these surveys have gathered data over timescales of years (e.g., Lanzuisi et al. 2014).

It is therefore worthwhile to further investigate these sources in order to understand if they can possibly substantially change the CT budget in our investigation. Following Lanzuisi et al. (2015) and Brightman et al. (2014), we applied their same toroidal modeling[48] to our joint *XMM-Newton*/*Chandra*-*NuSTAR* data sets. The only source that turned out to have a different column density classification is *cosmos181*, for which we obtained $\log(N_{\rm H}/{\rm cm}^{-2}) = 24.01^{+0.05}_{-0.06}$, but only with the Lanzuisi et al. (2015) modeling. For the other modeling and source *cosmos216,* the agreement between the measured column density is well within the 1σ uncertainties. Therefore, only *cosmos181* would nominally and potentially change its classification to CT due to a small increase in the estimated column density (by a little more than 0.1 dex). However, its addition to the CT bin do not appreciably change the column density distribution (Figure 10, bottom panel), as the equivalent number of CT sources would raise from ∼2 to ∼2.3.

9.1.2. CT Candidates in the Serendipitous Catalog

In the Serendip catalog, we have found three candidates CT sources: *ser261*, *ser235,* and *409*. None of these have archival low-energy data from *Chandra* or *XMM-Newton*.

The heavily absorbed nature of *ser261* was established already by a simple power-law fit that returns a very flat value of $\Gamma = 0.68^{+0.28}_{-1.08}$. The baseline model finds *ser261* to be CT. The torus models return a lower $N_{\rm H}$ estimate, with lower limits in the heavily absorbed range ($\log[N_{\rm H}/{\rm cm}^{-2}] > 23.8$ for BNTorus and $\log[N_{\rm H}/{\rm cm}^{-2}] > 23.7$ for MYTorus), i.e., they cannot confirm or reject the CT classification. Notice that, from an SDSS optical spectrum taken back in 2002, the source counterpart shows evidence of broad-lines hinting at a Type 1 nature. The source X-ray spectrum is the lowest-quality in our sample, with just 24 *NuSTAR* net-counts. Clearly, a much better *NuSTAR* spectrum, low-energy X-ray data, and newer optical spectra are needed to better understand the true nature of this source.

As for the borderline source *ser235*, we mention that both *baseline* and MYTorus models report upper limits in the CT regime. A power-law-only model shows a more canonical slope value with $\Gamma = 1.65^{+0.19}_{-0.10}$. Its borderline nature is likely due to the lack of low-energy data and its high redshift, z = 2.1, which makes the $N_{\rm H}$ measure with *NuSTAR*-only data more uncertain. For source *409*, the BNTorus model is the only one reporting an estimated column density upper limit in the CT regime (the baseline model cannot constrain its value at all). A simple power-law model returns $\Gamma = 1.21^{+0.53}_{-0.27}$, which—although a little flat—is still consistent at $\sim 1\sigma$ with the canonical value for an unabsorbed source.

[48] They both used an edge-on BNTorus model. Lanzuisi et al. (2015) adopted $\Gamma = 1.9$ with a scattered power-law component with the same photon index. Brightman et al. (2014) adopted $\Gamma = 1.7$ and a torus semi-opening angle of 30° with negligible scattered component.

9.2. Characterizing the Major Contributors of the Residual Missing CXB Flux

9.2.1. On the Heavily Absorbed Populations

Thanks to the high sensitivity of *NuSTAR* at high energies, we have investigated, with our flux-limited sample, the numerical predominance of the heavily absorbed AGN populations and the prominence in their spectrum of the reflection components. Indeed, these have been identified as the main actors in reproducing the residual unaccounted 20–30 keV CXB flux (Akylas et al. 2012). The limited sample size (63 sources), coupled with the large redshift range ($z \approx 0$–1.5), does not allow us to obtain stringent constraints. However, we have obtained indicative estimates of these quantities from a more robust source-by-source broadband (0.5–24 keV) modeling that is less prone to systematics and large statistical uncertainties[49] We have estimated an intrinsic fraction of AGN as a function of $N_{\rm H}$. Despite the low number of CT sources, we were able to extract a fraction relative to the whole Compton-thin AGN population (i.e., $\log[N_{\rm H}/{\rm cm}^{-2}] = 20$–24), which is formally in the range of $f_{\rm CT}^{20-24} = 0.02$–0.56, with an upper limit of $f_{\rm CT}^{20-24} < 0.66$. There are many assumptions affecting this value and its uncertainty to different extents: (i) the small number statistics (function of the small sample size and of the relatively high unabsorbed flux at which the distribution of the AGN is unbiased), (ii) the assumption of the most representative absorption bias value in the CT bin (which strongly varies within this interval), (iii) the particular model used to infer the absorption bias (we explored the BNTorus model with two different choices of the opening angle), and (iv) an accurate spectral modeling for the CT sources in order to obtain accurate source counts needed to extrapolate at the limited flux the unbiased contribution of the source in the CT bin. Many of these aspects required assumptions to be made, and we tried to make the most reasonable ones. This CT fraction is broadly representative for sources at redshift $z \sim 0.2$–1.0 and luminosities $\log(L_{\rm u,X}/{\rm erg\ s}^{-1}) \approx 43.4$–44.6, the intervals being the 15.9% and 84.2% percentile[50] ranges of the subsample of sources brighter than $S_{\rm smin}^{\rm intr}$ (see Section 6) that have constrained $N_{\rm H}$ values. Given the large number of $\log(N_{\rm H}/{\rm cm}^{-2}) = 23$–24 sources and the less-pronounced bias in this bin, we obtain much better and more stable constraints for these sources. Observational constraints for the local population tend to favor a larger fraction for these sources among the absorbed Compton-thin AGN for sources with comparable luminosity (Ricci et al. 2015). Comparable but stronger conclusions have been drawn by Liu et al. (2017) at higher redshifts ($z = 1.6$–2.4) for roughly similarly luminous sources (they include quasars that are less luminous by a factor of ∼2). We cannot draw comparably strong conclusions on this point; we find indications for a more numerous population of $\log(N_{\rm H}/{\rm cm}^{-2}) = 23$–24 compared to the $\log(N_{\rm H}/{\rm cm}^{-2}) =$ 22–23 one, but within the uncertainties, it is consistent with a constant value. Furthermore, we are not able to test and disfavor models at a confidence level higher than 90%. As for the absorption fraction (f_{22}) for Compton-thin sources as a function of unabsorbed luminosity, our estimated fractions (computed in two bins) do not significantly imply a decreasing trend, although they are in good agreement with those derived by much larger soft X-ray analysis on sources at similar redshifts (i.e., around or within $z \approx 0.1$–1; U14, Buchner et al. 2015). A general increasing trend of f_{22} with redshift has also been measured in deep X-ray spectroscopic investigations of the COSMOS and CDF-S fields (Buchner et al. 2015; Liu et al. 2017) and large complete samples (U14). This trend is reported in Figure 14 for sources at $\log(L_{\rm u,X}/{\rm erg\ s}^{-1}) \approx 43.5$–44.62. We have estimated a fraction at $z = 0.1$–0.5 for sources of similar luminosity, obtaining a generic agreement with extrapolations at lower redshift of the trend reported by Liu et al. (2017), as well as a good agreement with values estimated at $z < 1$ by U14 and Buchner et al. (2015). In order to better constrain and independently evaluate the luminosity and redshift dependence of $f_{\rm abs}$, a much larger sample (at least twice the size of the present sample) and better-quality data with good low-energy X-ray coverage are necessary.

9.2.2. The Importance of the Reflection Component

In our spectroscopic analysis, we also quantify the reflection strength for each source. It is therefore interesting to compare our results to the typical assumptions made in CXB population-synthesis models. Indeed, they generally implement relatively similar assumptions. The reflection is always assumed to have a constant value $R \approx 1$ within each population (e.g., Ballantyne et al. 2006; Treister et al. 2009; Akylas et al. 2012; Ueda et al. 2014) or possibly a function of the degree of obscuration (e.g., G07; Ueda et al. 2014; Esposito & Walter 2016) with no dispersion around a mean value. On average, we find median reflection values that are: (1) significantly lower ($R \approx 0.3$–0.7) than those assumed ($R \approx 1$) by CXB models and (2) exhibit a rather broad distribution with a median value relative to the whole sample of ∼0.4 (Table 6). Furthermore, we measure a significant anti-correlation with unabsorbed and intrinsic luminosities (the latter being more pronounced; see Figure 8 (lower panels) and Table 6). This trend is further confirmed by the findings of our companion paper on stacked *NuSTAR* spectra (DM17). In this context, we find sources with lower unabsorbed luminosities to have a median reflection ($\langle R \rangle = 0.73$) a factor of two stronger than more luminous ones ($\langle R \rangle = 0.31$). The broad R distribution reaches 50% percentile values a factor of two larger. When using intrinsic coronal luminosities, the differences exacerbates further by a factor of about two. A similar trend has been largely ignored by models; the one exception being the G07 model, for which QSOs have been assumed to have no reflection. G07 also assumes higher R for Type-1 sources ($R = 1.3$) compared to Type-2s ($R = 0.88$) in order to mimic a orientation-dependent disk reflection. Ueda et al. (2014) instead assumes a flat $R = 0.5$ from the disk and a torus-based contribution in the context of a luminosity- and redshift-dependent unified scenario in order to reproduce a total $R = 1$ for Seyfert galaxies.

Aird et al. (2015b), presenting the first direct measurements of the 10–40 keV XLF derived from the *NuSTAR* extragalactic survey program, pointed out a degeneracy in the models parameters (the distribution of $N_{\rm H}$ as a function of luminosity and z for the most obscured AGN and R) in order to reproduce the XLF. In particular, they show that the high-energy XLF can be alternatively modeled by either a distribution of $N_{\rm H}$ derived by Aird et al. (2015a) (see Figure 12) and a spectral model with

[49] Notice that, in our 3–24 keV BNTorus joint spectral analysis for the $\log(N_{\rm H}/{\rm cm}^{-2}) = 23.5$–24 sources, the $\log N_{\rm H}$ is derived with an accuracy a factor of two higher than that derived for sources selected at the same column densities and comparable fluxes in the soft X-ray studies by Lanzuisi et al. (2015) and Brightman et al. (2014).

[50] The range delimited by these values corresponds to the inclusion of ∼68% of the sources, assuming Gaussian distribution.

a uniform distribution of reflection strength in the range $0 < R < 2$ (i.e., $\langle R \rangle = 1$), or a distribution of $N_{\rm H}$ derived by Ueda et al. (2014) (Figure 12) and a fixed $R = 2$ at all luminosities. Our analysis does not allow us to conclusively break this degeneracy, as the fraction of CT AGN is poorly constrained. Nonetheless, the *NuSTAR*-derived $\langle R \rangle$ values as measured in this work and in DM17 firmly exclude the high and fixed values of R invoked in order to bring the Ueda et al. (2014) model into full consistency with the 10–40 keV XLF.

We find tentative evidence of an anticorrelation of R with $N_{\rm H}$, whereby more absorbed sources exhibit lower reflections. This is qualitatively in agreement with a disk-reflection scenario, although our median R values are smaller than those assumed by G07 (Table 6). This result, however, may also be indicative of a reflection component absorbed by the same medium obscuring the primary continuum in the hypothesis of no $N_{\rm H}$-dependence. Unfortunately, with our small sample, we cannot test this hypothesis at high significance. Furthermore, we must mention that local studies find mildly obscured Seyferts to have stronger or equally strong reflections than unobscured counterparts (Ricci et al. 2011; Esposito & Walter 2016). We have insufficient statistics to infer a similar trend at comparable low luminosities (i.e., $\log[L_{\rm u,X}/{\rm erg\ s^{-1}}] < 44$).

10. Conclusions

We focused on a sample of 63 bright 8–24 keV selected AGN with $S(8\text{–}24) \geqslant 7 \times 10^{-14}$ erg s^{-1} cm^{-2}, from the multi-tiered *NuSTAR* Extragalactic Survey fields. The sample spans a redshift range of $z = 0$–2.1, with a median value $\langle z \rangle = 0.58$. For the great majority of the sources (58), we performed spectral modeling in the broad 0.5–24 keV band by using archival low-energy spectra from *Chandra* and *XMM-Newton*. For five sources, selected from the serendipitous fields, low-energy data are not available. We used both empirically and physically motivated models, where the latter assumed Monte Carlo implementations of toroidal geometries. The results of the broadband spectral analysis can be summarized as follows:

1. About 25% of the sample is comprised of heavily absorbed sources with $\log(N_{\rm H}/{\rm cm^{-2}}) \geqslant 23$ (see Figure 5).
2. Depending on the details of the adopted modeling, the number of bona fide CT sources is 1–2 (Figure 10).
3. For the empirically motivated model, we computed unabsorbed 10–40 keV and intrinsic coronal 10–40 keV luminosities (i.e., removing the reflection contribution from the unabsorbed luminosities) and found that the former can lead to a luminosity-dependent overestimation of the latter, which is highest (a factor ∼3–4) at the lowest luminosities (i.e., $<10^{44}$ erg s^{-1}; see Section 4.4 and Figure 6).
4. The median reflection strength of the sample is $\langle R \rangle = 0.43$, with a large scatter (interquartile range 0.06–1.50). We find that R significantly anti-correlates with unabsorbed 10–40 keV luminosity (in agreement with DM17) and intrinsic 10–40 keV AGN luminosity (see Table 6 and Figure 8).
5. The observed $N_{\rm H}$ distribution for the absorbed ($\log[N_{\rm H}/{\rm cm^{-2}}] \geqslant 22$) sources is in agreement with CXB population-synthesis model predictions (see Figure 10). The agreement persists when accounting for different spectral modelings or possibly misclassified AGN claimed as CT by previous soft X-ray studies (Section 9.1.1).
6. From the absorption-corrected number fraction, we obtain a CT fraction broadly representative for $z \approx 0.2$–1.0 and $\log(L_{\rm u,X}/{\rm erg\ s^{-1}}) \approx 43.4$–44.6 AGN. The estimated fraction, relative to the AGN population at $\log(N_{\rm H}/{\rm cm^{-2}}) < 24$, is $f_{\rm CT}^{20\text{–}24} = 0.02$–0.56 (<0.66 at 90% c.l.). This value drops by a factor of ∼1.7 if we assume a toroidal obscurer with a halved opening angle (Figure 12).
7. We estimated the intrinsic fraction of obscured Compton-thin ($\log[N_{\rm H}/{\rm cm^{-2}}] \geqslant 22$) sources as a function of unabsorbed luminosity at 10–40 keV (Figure 13). The derived fractions cannot constrain a trend with luminosity, but they are in good agreement with results reported by other authors at similar epochs (i.e., $z \lesssim 1.0$). We further calculate the absorption fraction for sources at $z = 0.1$–0.5 with $\log(L_{\rm u,X}/{\rm erg\ s^{-1}}) \approx 43.6$–44.3. The resulting $f_{22} = 0.36 \pm 0.18$ agrees with extrapolated decreasing trends (from high to low z) from surveys covering the same luminosity range and higher redshifts ($z \approx 3$) with reported values at similar redshift range.

Clearly, increasing the number of sources to spectroscopically study at these flux levels, with good-quality low-energy data, would help to better characterize the *NuSTAR* hard-band selected AGN population at moderate redshift ($z \approx 0.5$–1). This will help in further elucidating the hinted correlation between reflection strength and column density and start a robust investigation of possible redshift dependence of the absorbed fractions.

The main benefit of enlarging the sample size will be the increase in the number of robust CT sources identified at redshifts and luminosities poorly probed currently. This will allow: (1) a more robust and constrained estimate of the CT fraction; (2) the discrimination of CXB population-synthesis models through the comparison of more accurate source counts in the $\log(N_{\rm H}/{\rm cm^{-2}}) = 24$–25 range of column densities; (3) to start probing the $\log(N_{\rm H}/{\rm cm^{-2}}) = 25$–26 bin, which is precluded in our analysis due to a combination of strong absorption bias and small number statistics. The serendipitous survey will progressively increase its sky coverage, providing crucial help in this regard, especially if backed up by ancillary spectroscopic low-energy X-ray and optical data. Three (likely four) CT AGN have already been found in the 13 deg^2 area probed by the first 40 month serendipitous survey sample in Lansbury et al. (2017a). This number has to be regarded as lower limit, given the 70% redshift completeness and the hardness ratio approach used to find extremely heavily obscured candidates.

To make significant progress in this field, an X-ray observatory with a collecting area more than one order of magnitude larger, sub-arcmin PSF, and higher-energy coverage (such as the High-Energy X-ray Probe)[51] is required. It will allow to: (1) resolve the great majority (∼80–90%) of the CXB at its spectral energy density peak, (2) break the degeneracy between high-energy spectral features and the abundance of CT sources, and (3) perform detailed studies on the CT source population. Despite the modest technology development required, which is

[51] https://pcos.gsfc.nasa.gov/physpag/probe/HEXP_2016.pdf

based on the *NuSTAR* heritage, such an instrument is not currently planned for the next decade.

We thank the anonymous referee for useful comments that helped improve our analysis and the presentation of our results. We thank Johannes Buchner and Yoshihiro Ueda for providing machine-readable results on the absorbed fractions. L.Z. thanks R. Gilli, F. Nicastro, E. Piconcelli, R. Valiante, F. Vito, and D. Burlon for useful discussions. L.Z., A.C., F.F., G.L., and A.M. acknowledge financial support under ASI/INAF contract I/037/12/0. A.C. acknowledges the Caltech Kingsley fellowship program. G.L. acknowledges financial support from the CIG grant eEASY No. 321913. F.E.B. acknowledges support from CONICYT-Chile (Basal-CATA PFB-06/2007, FONDECYT Regular 1141218), the Ministry of Economy, Development, and Tourism's Millennium Science Initiative through grant IC120009, awarded to The Millennium Institute of Astrophysics, MAS. This work was supported under NASA Contract NNG08FD60C, and made use of data from the *NuSTAR* mission, a project led by the California Institute of Technology, managed by the Jet Propulsion Laboratory, and funded by NASA. We thank the *NuSTAR* Operations, Software, and Calibration teams for support with the execution and analysis of these observations. This research has made use of the *NuSTAR* Data Analysis Software (NuSTARDAS) jointly developed by the ASI Science Data Center (ASDC, Italy) and the California Institute of Technology (USA).

Appendix
Notes on Single Sources

A.1. COSMOS

The evaluation of possible contributions to our spectra from additional flux from sources located within the spectral extraction radii is performed using the source information provided by the COSMOS-Legacy catalog (Civano et al. 2016) and the low-energy spectra extracted by Marchesi et al. (2016). We did not try joint broadband models with the *NuSTAR* data (except for the CT source *cosmos330*) through complicated models, but rather used a flux estimate at low energy with a simple absorbed power-law model to evaluate possible contamination in common energy bands.

1. *cosmos107*: The *NuSTAR* extraction radius includes two sources of similar flux in the COSMOS-Legacy field: lid1689 and lid1688. The *XMM-Newton* spectrum includes them as well. Source lid1688 has twice the number of net-counts as lid1689 and is the obscured one (i.e., low-energy counterpart). It has an Fe Kα line at the optical spectroscopic redshift. The hard-band *NuSTAR* flux for *cosmos107* from the baseline model gives a flux of 9×10^{-14} erg s^{-1} cm^{-2}. Assuming the absorbed source accounts, as suggested from the number of *Chandra* detected net-counts, for 2/3 of the 8–24 keV *NuSTAR* flux, this source would have a *NuSTAR* flux of $\sim 6 \times 10^{-14}$ erg s^{-1} cm^{-2} (i.e., below the threshold defining our sample), potentially dropping it from the sample.
2. *cosmos129*: The *NuSTAR* extraction radius includes two *Chandra* sources: cid284 (the low-energy counterpart) and cid818. The latter is at the edge of the *NuSTAR* extraction radius; its spectrum has 30 net-counts (0.5–8 keV) and is consistent with being unabsorbed. The *XMM-Newton* extraction radius does not include this source. Hence, only the *NuSTAR* spectrum is potentially affected by cid818. However, at 5–7 keV, cid818 flux is one to two orders of magnitudes fainter than cid284, so we can safely assume that the *NuSTAR* measurement is not significantly affected by cid818.
3. *cosmos154*: The scattered components in *Chandra* and *XMM-Newton* seem to have different shapes (Γ) and normalizations, suggestive of source variability. The source is close (several arcsec) to another AGN (cid366). *Chandra* does not include the latter source, while *XMM-Newton* partially does (it is heavily blended). Moreover, *Chandra* seems to exhibit diffuse emission around the source, which is probably partially included in *XMM-Newton*. We have decided to exclude the *XMM-Newton* data and use only *Chandra* (which has the highest statistics). *NuSTAR* will include both CID366 emission and thermal diffuse emission. However, they are relevant only at energies lower than 3–4 keV. The cid366 spectrum level at 3 keV is comparable with cosmos154, while there is a factor $\sim$10 difference at 4 keV. We decided to use *NuSTAR* only at energies above 4 keV.
4. *cosmos178*: The *NuSTAR* extraction radius includes five sources. Three of them dominate in terms of counts: cid168 (the low-energy counterpart), cid190, and cid192. The 0.5–8 keV (3–8 keV) flux of the first one, i.e., the low-energy counterpart, is 5.1×10^{-14} erg s^{-1} cm^{-2} (2.7×10^{-14} erg s^{-1} cm^{-2}). The other two have lower fluxes, 1.7×10^{-14} erg s^{-1} cm^{-2} (9.5×10^{-15} erg s^{-1} cm^{-2}) and 2.2×10^{-14} erg s^{-1} cm^{-2} (6.8×10^{-15} erg s^{-1} cm^{-2}). The *XMM-Newton* spectrum includes only the cid168 source. The fluxes are comparable within a factor of three. Therefore, the *NuSTAR* spectrum includes flux from all the three sources. The 8–24 keV flux of this source is $\sim 7 \times 10^{-14}$ erg s^{-1} cm^{-2}, implying that the cid168 flux is very likely fainter. This source would potentially be dropped from the sample.
5. *cosmos181*: The *NuSTAR* extraction radius includes four sources. Out of these, two are very faint and the other two dominate the total number of counts. These are: cid482 (the low-energy counterpart) and cid484. Below 4–5 keV, both sources have comparable *Chandra* fluxes. Although cid482 is a factor of few higher in flux, the contribution at 4–5 keV of cid484 is not negligible. Therefore, we decided to limit the *NuSTAR* range for spectral fitting to 4.5–24 keV. The *XMM-Newton* spectrum does not include cid484.
6. *cosmos206*: The *NuSTAR* extraction radius includes two sources: cid329 (the low-energy counterpart) and cid328. The latter is more than one order of magnitude fainter at all energies. Therefore, it should not significantly affect our modelings.
7. *cosmos207*: The *NuSTAR* extraction radius includes two sources separated by 33 arcsec: lid1645 (the low-energy counterpart) and lid1644. The counterpart has a factor of $\sim$5 more counts than lid1644 in the 3–8 keV *Chandra* spectral range. Therefore, the *NuSTAR* spectra should not be substantially contaminated by the latter source.
8. *cosmos229*: The small *NuSTAR* extraction radius (25 arcsec) includes two sources separated by 26 arcsec: cid420 (the low-energy counterpart, offset 14 arcsec from the *NuSTAR* position of cosmos229) and cid 1120. In the

Chandra data, cid420 has a 3-8 keV flux which is 1.2–4 (1σ range) times higher than cid1120. Therefore, it is likely that at least the soft *NuSTAR* band is contaminated to some extent by the fainter source. Because of this, the source would potentially be dropped from the sample because its hard-band *NuSTAR* flux would potentially fall below threshold.

9. *cosmos297*: The *Chandra* spectrum slightly differs from the *XMM-Newton* spectrum at very low energies (∼0.5–0.7 keV), though it has very little impact on our modeling;
10. *cosmos330*: The *NuSTAR* extraction radius includes two sources separated by 26 arcsec: lid1791 (the identified low-energy counterpart) and lid1792. In the 3–8 keV band, the counterpart is a factor ∼2–2.5 (a factor of ∼2 in the *Chandra* collected net counts) brighter than the latter contaminant source. We fit the *cosmos330* spectra jointly with the *Chandra* spectrum of lid1792 to account for its contamination and recover the intrinsic spectral parameters for lid1791. We find that the spectral parameters of *cosmos330* do not appreciably vary and that the source is still classified as CT.

A.2. ECDFS

1. *ecdfs5*: This source does not have unique counterparts in M15. There is one at low redshift ($z = 0.141$; *Chandra* ID 103) and one at high redshift ($z = 1.957$; *Chandra* ID 100). Their separation is ∼22 arcsec, which is smaller than the *NuSTAR* spectral extraction radius. We therefore tried a joint modeling of these two sources with the *NuSTAR* data. Both sources are unabsorbed with $\Gamma \approx 2.1$. The *NuSTAR* spectra in the common 3–8 keV band have normalizations that are higher than the *Chandra* spectra by factors of ∼2 and ∼5.4 for ID 103 and ID 100, respectively. In the 8–24 keV band, ID 103 has a flux ∼3.5 times larger than ID 100. We therefore assume that ID 103 is the correct low-energy counterpart and used it in our analysis.

A.3. EGS

1. *egs26*: The spectrum of this source is flat and unabsorbed. A fit with an absorbed power-law returns a best-fit $\Gamma = 0.9$ with negligible column density for which we place an upper limit at $\log(N_{\rm H}/{\rm cm}^{-2}) \leqslant 20.3$ with $W{\rm stat}/{\rm dof} = 472.31/433$. Our baseline parameterization returns an apparently better fit with $W{\rm stat}/{\rm dof} = 442.9/431$ with $\Gamma = 2.37$, $\log(N_{\rm H}/{\rm cm}^{-2}) \leqslant 21.3$ and $R \approx 67$. The reflection parameter value is extremely high and unphysical. We therefore tried to add a dual-absorber modeling (e.g., Cappi et al. 1996; Dong et al. 2004) to the primary power-law, i.e., a further absorption component given by an inhomogenous cold medium at larger scales by employing the model ZPCFABS. With this parameterization, we obtained an even better fit ($W{\rm stat}/{\rm dof} = 424.4/429$) with more reasonable parameters (as reported in Table 5): $\Gamma = 1.56$, $\log(N_{\rm H}/{\rm cm}^{-2}) \leqslant 21.1$, and $R < 0.18$. For the second absorber, we find $\log(N_{\rm H}/{\rm cm}^{-2}) = 23.40^{+0.05}_{-0.02}$ and a covering fraction $f_c = 0.73 \pm 0.03$. Spectra and best-fit model are reported in Figure 17.

A.4. Serendip

1. *ser243*: This source has Γ flatter than the canonical value at high significance (see Table 5). It also seems to require a scattered component (in *Chandra* data at energies below 0.5 keV) with $\Gamma_{\rm sc} \simeq 2.4$. Freezing the primary photon index to the canonical $\Gamma = 1.8$ makes the scattered component steeper, $\Gamma_{\rm sc} \simeq 3$. In this case, the reflection strength raises from $R < 0.74$ to $R = 1.1$.
2. *ser318*: The *XMM-Newton* and *NuSTAR* data are simultaneous, though the spectra do not to agree well at 3–4 keV: *XMM-Newton* has a factor of 7–8 fewer counts in this range. *NuSTAR* shows a hint of Fe Kα at ∼3 keV.
3. *ser37*: The spectrum of this source is very flat and unabsorbed. A fit with an absorbed power-law returns $\Gamma = 0.2$ and negligible column density. However, the modeling is not acceptable, with strong residuals across the broadband and fit statistics of $W{\rm stat}/{\rm dof} = 345.04/218$. The baseline modeling yields a much better parameterization, with $W{\rm stat}/{\rm dof} = 225.77/217$. The best-fit parameters are $\Gamma \approx 2.5$, $\log(N_{\rm H}/{\rm cm}^{-2}) \leqslant 19.9$, and $R = 10.3$. Both Γ and R are too high. Therefore, as done with *egs26*, we tried a dual-absorber model, modifying the primary power-law with cold and partially ionized partial-covering absorbers (ZPCFABS and ZXIPCF, respectively). The model that gives the better parameterization in terms of fit statistics and reasonable parameters (see Table 5) is obtained using the warm ionized absorption model and imposing $\Gamma = 1.8$. For the absorber, we obtained the following parameters: $\log(N_{\rm H}/{\rm cm}^{-2}) = 22.80^{+0.02}_{-0.03}$, $f_c = 0.969^{+0.003}_{-0.006}$, and an ionization parameter $\log(\xi/{\rm erg\ cm\ s}^{-1}) = -0.55^{+0.10}_{-0.19}$. Spectra and best-fit model are reported in Figure 17.
4. *ser267*: In our spectral analysis, we treated this AGN as a canonical unabsorbed source. The joint *Chandra* and *NuSTAR* FPMA+FPMB low-quality spectra (i.e., 45, 27, and 38 total net-counts, respectively) are jointly modeled with an unabsorbed baseline model with primary continuum slope consistent with the canonical $\Gamma = 1.8$–2 value. On the other hand, in the *NuSTAR* spectra (i.e., in both focal plane modules), we find evidence of a strong residual at an energy of ∼5.7 keV (10 net-counts in both focal plane modules). The significance of this feature, if modeled with a Gaussian line, is at the $\sim 2\sigma$ level (based on $\Delta\chi^2$ confidence contours on line energy and normalization). The line can be modeled by a 6.4 keV Fe Kα at the redshift $z = 0.131$ of the source. In our best-fit baseline parameterization, the line has an observed EW ≈ 1.4 keV. The low-quality *Chandra* spectrum is consistent with this best-fit line solution. This may be an indication that the source hosts an obscured AGN. We mention, however, that the optical spectrum from SDSS shows broad lines pointing to a Type 1 classification for this source. Clearly, better X-ray data across the broad 0.5–24 keV band are needed to shed light on the nature of this source and properly assess the significance of the line as Fe Kα.
5. *ser148*: A simple power-law model shows a flat spectrum with $\Gamma = 1.4$ with strong residuals at low energies ($W{\rm stat}/{\rm dof} = 3143.79/1261$). A simple cold absorption is not required. The baseline model does not improve the modeling. Reflection is not required, as the large residuals are at soft energies (<1–2 keV). We therefore tried

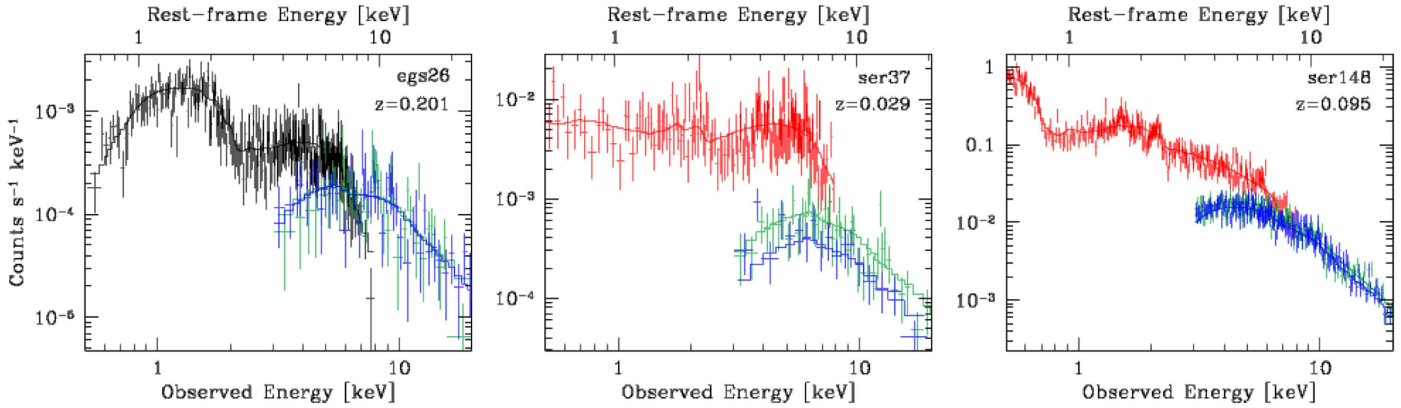

Figure 17. Broadband spectra and relative best-fit model for sources *egs26*, *ser37,* and *ser148*. The adopted best-fit model is the baseline one modified with the addition of a low-energy, ionized/neutral, partial-covering absorber. Black, red, green, and blue spectra refer to *Chandra*, *XMM-Newton*, *NuSTAR*-FPMA, and *NuSTAR*-FPMB, respectively.

additional warm absorption (ZXIPCF) on the primary component and obtained a good representation of the spectrum (see Table 5) with the following warm absorber parameters: $\log(N_{\rm H}/{\rm cm}^{-2}) = 22.76 \pm 0.01$, $f_c = 1.0$ and a ionization parameter $\log(\xi/{\rm erg\ cm\ s}^{-1}) = 1.39 \pm 0.05$. Spectra and best-fit model are reported in Figure 17.

6. *ser261*: No observations at low energy are available for this sources from either *Chandra* or *XMM-Newton*. There are short observations (<10 ks) from *Swift*-XRT in which a source is barely detected 10–20 arcsec from the *NuSTAR* position. If this is the right low-energy counterpart, it is difficult to model the joint *Swift*-XRT-*NuSTAR* spectrum. It results in a heavily absorbed source (from *NuSTAR* data) with a large scattered component (from *Swift*). We also must mention that the SDSS spectrum of the optical counterpart shows evidence of broad emission lines.

ORCID iDs

A. Comastri https://orcid.org/0000-0003-3451-9970
S. Puccetti https://orcid.org/0000-0002-2734-7835
J. Aird https://orcid.org/0000-0003-1908-8463
G. B. Lansbury https://orcid.org/0000-0002-5328-9827
G. Lanzuisi https://orcid.org/0000-0001-9094-0984
J. R. Mullaney https://orcid.org/0000-0002-3126-6712
D. Stern https://orcid.org/0000-0003-2686-9241
M. Ajello https://orcid.org/0000-0002-6584-1703
D. M. Alexander https://orcid.org/0000-0002-5896-6313
D. R. Ballantyne https://orcid.org/0000-0001-8128-6976
W. N. Brandt https://orcid.org/0000-0002-0167-2453
C.-T. J. Chen https://orcid.org/0000-0002-4945-5079
D. Farrah https://orcid.org/0000-0003-1748-2010
F. A. Harrison https://orcid.org/0000-0003-2992-8024
P. Gandhi https://orcid.org/0000-0003-3105-2615
L. Lanz https://orcid.org/0000-0002-3249-8224
A. Masini https://orcid.org/0000-0002-7100-9366
S. Marchesi https://orcid.org/0000-0001-5544-0749
C. Ricci https://orcid.org/0000-0001-5231-2645
E. Treister https://orcid.org/0000-0001-7568-6412

References

Aird, J., Alexander, D. M., Ballantyne, D. R., et al. 2015b, ApJ, 815, 66
Aird, J., Coil, A. L., Georgakakis, A., et al. 2015a, MNRAS, 451, 1892
Ajello, M., Rau, A., Greiner, J., et al. 2008, ApJ, 673, 96
Akylas, A., Georgakakis, A., Georgantopoulos, I., Brightman, M., & Nandra, K. 2012, A&A, 546, A98
Alexander, D. M., Stern, D., Del Moro, A., et al. 2013, ApJ, 773, 125
Ballantyne, D. R., Draper, A. R., Madsen, K. K., Rigby, J. R., & Treister, E. 2011, ApJ, 736, 56
Ballantyne, D. R., Everett, J. E., & Murray, N. 2006, ApJ, 639, 740
Baumgartner, W. H., Tueller, J., Markwardt, C. B., et al. 2013, ApJS, 207, 19
Brandt, W. N., & Alexander, D. M. 2015, A&ARv, 23, 1
Brandt, W. N., Alexander, D. M., Hornschemeier, A. E., et al. 2001, AJ, 122, 2810
Brightman, M., & Nandra, K. 2011, MNRAS, 413, 1206
Brightman, M., Nandra, K., Salvato, M., et al. 2014, MNRAS, 443, 1999
Brightman, M., & Ueda, Y. 2012, MNRAS, 423, 702
Brusa, M., Civano, F., Comastri, A., et al. 2010, ApJ, 716, 348
Buchner, J., Georgakakis, A., Nandra, K., et al. 2014, A&A, 564, A125
Buchner, J., Georgakakis, A., Nandra, K., et al. 2015, ApJ, 802, 89
Burlon, D., Ajello, M., Greiner, J., et al. 2011, ApJ, 728, 58
Cappelluti, N., Hasinger, G., Brusa, M., et al. 2007, ApJS, 172, 341
Cappelluti, N., Li, Y., Ricarte, A., et al. 2017, ApJ, 837, 19
Cappi, M., Mihara, T., Matsuoka, M., et al. 1996, ApJ, 456, 141
Cash, W. 1979, ApJ, 228, 939
Castelló-Mor, N., Carrera, F. J., Alonso-Herrero, A., et al. 2013, A&A, 556, A114
Civano, F., Elvis, M., Brusa, M., et al. 2012, ApJS, 201, 30
Civano, F., Hickox, R. C., Puccetti, S., et al. 2015, ApJ, 808, 185
Civano, F., Marchesi, S., Comastri, A., et al. 2016, ApJ, 819, 62
Comastri, A., Ranalli, P., Iwasawa, K., et al. 2011, A&A, 526, L9
Comastri, A., Setti, G., Zamorani, G., & Hasinger, G. 1995, A&A, 296, 1
Crawford, D. F., Jauncey, D. L., & Murdoch, H. S. 1970, ApJ, 162, 405
Dadina, M. 2008, A&A, 485, 417
Del Moro, A., Alexander, D. M., Aird, J. A., et al. 2017, ApJ, 849, 57
Del Moro, A., Mullaney, J. R., Alexander, D. M., et al. 2014, ApJ, 786, 16
Della Ceca, R., Caccianiga, A., Severgnini, P., et al. 2008, A&A, 487, 119
Dong, H., Xue, S.-J., Li, C., & Cheng, F.-Z. 2004, ChJAA, 4, 427
Draper, A. R., & Ballantyne, D. R. 2010, ApJL, 715, L99
Elvis, M., Civano, F., Vignali, C., et al. 2009, ApJS, 184, 158
Esposito, V., & Walter, R. 2016, A&A, 590, A49
Fabian, A. C., Lohfink, A., Kara, E., et al. 2015, MNRAS, 451, 4375
Feigelson, E. D., & Nelson, P. I. 1985, ApJ, 293, 192
Feruglio, C., Daddi, E., Fiore, F., et al. 2011, ApJL, 729, L4
Gandhi, P., Fabian, A. C., Suebsuwong, T., et al. 2007, MNRAS, 382, 1005
Gehrels, N. 1986, ApJ, 303, 336
Georgantopoulos, I., Akylas, A., Georgakakis, A., & Rowan-Robinson, M. 2009, A&A, 507, 747
Georgantopoulos, I., Comastri, A., Vignali, C., et al. 2013, A&A, 555, A43
Georgantopoulos, I., Georgakakis, A., & Akylas, A. 2007, A&A, 466, 823
Giacconi, R., Rosati, P., Tozzi, P., et al. 2001, ApJ, 551, 624
Gilli, R. 2013, MmSAI, 84, 647
Gilli, R., Comastri, A., & Hasinger, G. 2007, A&A, 463, 79
Goulding, A. D., Forman, W. R., Hickox, R. C., et al. 2012, ApJS, 202, 6
Harrison, F. A., Aird, J., Civano, F., et al. 2016, ApJ, 831, 185
Harrison, F. A., Craig, W. W., Christensen, F. E., et al. 2013, ApJ, 770, 103
Hasinger, G., Miyaji, T., & Schmidt, M. 2005, A&A, 441, 417

Hickox, R. C., & Markevitch, M. 2006, ApJ, 645, 95
Isobe, T., Feigelson, E. D., & Nelson, P. I. 1986, ApJ, 306, 490
Kalberla, P. M. W., Burton, W. B., Hartmann, D., et al. 2005, A&A, 440, 775
Krivonos, R., Revnivtsev, M., Lutovinov, A., et al. 2007, A&A, 475, 775
La Franca, F., Fiore, F., Comastri, A., et al. 2005, ApJ, 635, 864
Lansbury, G. B., Alexander, D. M., Aird, J., et al. 2017a, ApJ, 846, 20
Lansbury, G. B., Stern, D., Aird, J., et al. 2017b, ApJ, 836, 99
Lanzuisi, G., Civano, F., Elvis, M., et al. 2013, MNRAS, 431, 978
Lanzuisi, G., Ponti, G., Salvato, M., et al. 2014, ApJ, 781, 105
Lanzuisi, G., Ranalli, P., Georgantopoulos, I., et al. 2015, A&A, 573, A137
Lavalley, M. P., Isobe, T., & Feigelson, E. D. 1992, BAAS, 24, 839
Lawrence, A., & Elvis, M. 1982, ApJ, 256, 410
Lehmer, B. D., Brandt, W. N., Alexander, D. M., et al. 2005, ApJS, 161, 21
Lehmer, B. D., Xue, Y. Q., Brandt, W. N., et al. 2012, ApJ, 752, 46
Liu, T., Tozzi, P., Wang, J.-X., et al. 2017, ApJS, 232, 8
Liu, Y., & Li, X. 2015, MNRAS, 448, L53
Luo, B., Brandt, W. N., Xue, Y. Q., et al. 2017, ApJS, 228, 2
Madsen, K. K., Harrison, F. A., Markwardt, C. B., et al. 2015, ApJS, 220, 8
Magdziarz, P., & Zdziarski, A. A. 1995, MNRAS, 273, 837
Mainieri, V., Hasinger, G., Cappelluti, N., et al. 2007, ApJS, 172, 368
Marchesi, S., Ajello, M., Marcotulli, L., et al. 2018, ApJ, Submitted (arXiv:1801.03166)
Marchesi, S., Lanzuisi, G., Civano, F., et al. 2016, ApJ, 830, 100
Marshall, F. E., Boldt, E. A., Holt, S. S., et al. 1980, ApJ, 235, 4
Marshall, H. L. 1985, ApJ, 299, 109
Masini, A., Civano, F., Comastri, A., et al. 2018, ApJS, Submitted (arXiv:1801.0188)
Mullaney, J. R., Del-Moro, A., Aird, J., et al. 2015, ApJ, 808, 184
Murphy, K. D., & Yaqoob, T. 2009, MNRAS, 397, 1549
Mushotzky, R. F., Cowie, L. L., Barger, A. J., & Arnaud, K. A. 2000, Natur, 404, 459
Nandra, K., Laird, E. S., Aird, J. A., et al. 2015, ApJS, 220, 10
Page, K. L., Reeves, J. N., O'Brien, P. T., & Turner, M. J. L. 2005, MNRAS, 364, 195
Page, M. J., & Carrera, F. J. 2000, MNRAS, 311, 433
Piconcelli, E., Jimenez-Bailón, E., Guainazzi, M., et al. 2005, A&A, 432, 15
Ranalli, P., Comastri, A., Vignali, C., et al. 2013, A&A, 555, A42
Reeves, J. N., & Turner, M. J. L. 2000, MNRAS, 316, 234
Ricci, C., Bauer, F. E., Arevalo, P., et al. 2016, ApJ, 820, 5
Ricci, C., Ueda, Y., Koss, M. J., et al. 2015, ApJL, 815, L13
Ricci, C., Walter, R., Courvoisier, T. J.-L., & Paltani, S. 2011, A&A, 532, A102
Sazonov, S., Revnivtsev, M., Krivonos, R., Churazov, E., & Sunyaev, R. 2007, A&A, 462, 57
Schmidt, M. 1968, ApJ, 151, 393
Setti, G., & Woltjer, L. 1989, A&A, 224, L21
Steffen, A. T., Barger, A. J., Cowie, L. L., Mushotzky, R. F., & Yang, Y. 2003, ApJL, 596, L23
Tozzi, P., Gilli, R., Mainieri, V., et al. 2006, A&A, 451, 457
Treister, E., & Urry, C. M. 2006, ApJL, 652, L79
Treister, E., Urry, C. M., & Virani, S. 2009, ApJ, 696, 110
Ueda, Y., Akiyama, M., Hasinger, G., Miyaji, T., & Watson, M. G. 2014, ApJ, 786, 104
Vignali, C., Comastri, A., Cappi, M., et al. 1999, ApJ, 516, 582
Vito, F., Gilli, R., Vignali, C., et al. 2014, MNRAS, 445, 3557
Wachter, K., Leach, R., & Kellogg, E. 1979, ApJ, 230, 274
Wik, D. R., Hornstrup, A., Molendi, S., et al. 2014, ApJ, 792, 48
Worsley, M. A., Fabian, A. C., Bauer, F. E., et al. 2005, MNRAS, 357 1281
Xue, Y. Q., Luo, B., Brandt, W. N., et al. 2011, ApJS, 195, 10
Xue, Y. Q., Luo, B., Brandt, W. N., et al. 2016, ApJS, 224, 15
Xue, Y. Q., Wang, S. X., Brandt, W. N., et al. 2012, ApJ, 758, 129